ASYMMETRIC TANDEM ORGANIC SOLAR CELLS

THOMAS JONATHAN HOWELLS

DEPARTMENT OF CHEMISTRY

UNIVERSITY OF WARWICK

FOR THE DEGREE OF DOCTOR OF PHILOSOPHY

DECEMBER 2011

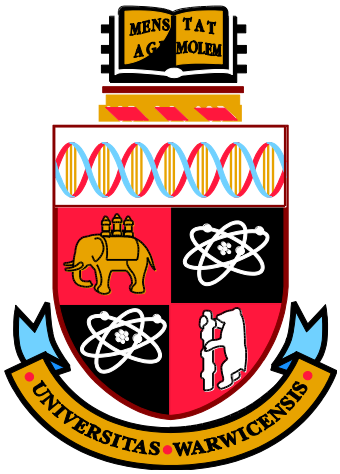

TABLE OF CONTENTS

DECLARATION

I confirm that the work in this thesis is my own, conducted during my time at the University of Warwick, with the exception of the solution processed TiOx / SubPc hybrid cells described for optical modelling in Chapter 4; these devices were fabricated by Chloe Dearden, but of interest for optical modelling. Some parts of this thesis, particularly Chapter 5, have been published and presented at an international conference. None of the work has been previously presented for a higher degree.

ACKNOWLEDGEMENTS

It is fitting to take a moment to acknowledge those who have helped me along the way during my PhD, without which I would not have reached this point. Firstly, my supervisor, Professor Tim Jones, for giving me this opportunity to work on an area I find both interesting and challenging, and for his support during my studies. I would also like to acknowledge my industrial sponsor, Kurt J. Lesker Company, for their funding and expertise in vacuum systems, without which this project would have been much more difficult. In addition, Professor Jenny Nelson at Imperial College, London, for her help with optical modelling, and David James, also at Imperial College, for helping me with ellipsometry measurements.

Equally, the rest of my research group have all helped me in one way or another during my PhD, so my thanks for putting up with my chain-tea-drinking habits go to Dr Virendra Chauhan, Dr Stefan Schumann, Ian Hancox, Nicola Beaumont, Luke Rochford, Edward New, Natalie Unsworth, Chloe Dearden, Raffaello da Campo and Gavin Jones. Last but far from least, Dr Paul Sullivan, from whom I have learnt a lot about chemistry, vacuum science, photovoltaics and Swagelok fittings, and whose advice has always been helpful.

Finally, I would like to thank my family, for not asking too many times when I was going to get a real job, and for their support. In particular, my fiancée Sarah for putting up with me through my sometimes unusual working hours and general geekiness!

LIST OF ABBREVIATIONS

Al – Aluminium

AFM – Atomic Force Microscopy

Ag – Silver

AM – Air Mass; effective measure of atmospheric path length.

AM0 – Sun's irradiance in space, with no atmospheric attenuation.

AM1.5G – Standard spectrum for solar cells, Air Mass 1.5 Global.

BCP – Bathocuproine, or 2,9-Dimethyl-4,7-diphenyl-1,10-phenanthroline

C_{60} – Fullerene

CdTe – cadmium telluride

ClAlPc – Aluminium Phthalocyanine Chloride

CuPc – Copper (II) Phthalocyanine

DSSC – Dye sensitized solar cell

DI water - De-ionised water.

EQE – External Quantum Efficiency

FF – Fill factor

eV – electron volt

e^- - shorthand for an electron.

GaAs – gallium arsenide

HOMO – Highest Occupied Molecular Orbital

H_2Pc – metal-free phthalocyanine.

h^+ - shorthand for a hole.

ITO – Indium-Tin Oxide

IQE – Internal Quantum Efficiency

J_{sc} – Short-circuit current.

J-V curve – Current Density vs Voltage curve.

K-cell – Knudsen cell

KJLC – Kurt J. Lesker Company

LUMO – Lowest Unoccupied Molecular Orbital

MDMO-PPV - poly(2-methoxy-5-(3',7'-dimethyloctyloxy)-1,4-phenylene vinylene)

MEH-PPV - poly(2-methoxy-5-(2'-ethyl-hexyloxy)-1,4-phenylene vinylene)

MoO_x – Molybdenum Oxide

OLED – Organic light emitting diode

OFET – Organic field effect transistor

OMBD - Organic molecular beam deposition.

OPV – Organic photovoltaic

P3HT - poly(3-hexylthiophene)

Pc – Phthalocyanine

PCBM - [6,6]-phenyl-C_{61} butyric acid methyl ester

$PC_{70}BM$ - [6,6]-phenyl-C_{71} butyric acid methyl ester

PCE – Power Conversion Efficiency

PCPDTBT - Poly[2,1,3-benzothiadiazole-4,7-diyl[4,4-bis(2-ethylhexyl)-4H-cyclopenta[2,1-b:3,4-b']dithiophene-2,6-diyl]]

PTCBI - 3,4,9,10-perylenetetracarboxylic bis-benzimidazole

PV – Photovoltaic

QCM – Quartz Crystal Microbalance

SubPc – Boron Subpthalocyanine Chloride

TiO_x – Titanium Oxide

NREL – National Renewable Energy Laboratory (US)

UV-vis – Electroabsorption measurement in the ultraviolet to visible (and often near-infrared) ranges.

V_{oc} – Open circuit voltage.

LIST OF MATHEMATICAL SYMBOLS

α - absorption coefficient

λ – wavelength

ε_r – relative permittivity of a material

μ_r – relative permeability of a material.

ρ - free charge density.

θ – angle of incidence, measured from surface normal.

τ - exciton lifetime

σ - conductivity

A – Absorptance

B - magnetic field

D – Diffusion coefficient

E – Energy

E - electric field

D - electric displacement field (or electric field in a medium)

E_f – Fermi energy

E_g – band gap in a material.

H - magnetizing field (or magnetic field in a medium)

I – Current

J – Current density

$\boldsymbol{j}$ - free current density

k – wavevector

L_D - exciton diffusion length

m - mass

n – number of excitons.

P - Power

Q_A – Quantum efficiency of absorption

Q_{Diff} – Quantum efficiency of diffusion

Q_{Diss} – Quantum efficiency of dissociation

Q_T – Quantum efficiency of charge transport

R – Resistance, electrical

Ir – Intensity / Irradiance

S_R - Spectral response of reference diode

S_T - Spectral response of cell under test.

T – Temperature, Kelvin.

TR - Transmittance

t – time

V - Voltage

x - distance

LIST OF PHYSICAL CONSTANTS

c – speed of light; 299 792 458 m / s

ε_0 - permittivity of free space; $8.85418782 \times 10^{-12}$ m^{-3} kg^{-1} s^4 A^2

h – Planck's constant; 6.626068×10^{-34} m^2 kg / s

k_b – Boltzmann's constant; $1.3806503 \times 10^{-23}$ m^2 kg s^{-2} K^{-1}

q_e – electronic charge; $1.60217646 \times 10^{-19}$ coulombs

μ_0 - permeability of free space; $1.25663706 \times 10^{-6}$ m kg s^{-2} A^{-2}

ABSTRACT

Organic photovoltaics (OPVs) is an area that has attracted much attention recently as a potential low cost, sustainable source of energy with a good potential for full-scale commercialisation. Understanding the factors that determine the efficiency of such cells is therefore a high priority, as well as developing ways to boost efficiency to commercially-useful levels. In addition to an intensive search for new materials, significant effort has been spent on ways to squeeze more performance out of existing materials, such as multijunction cells. This thesis investigates double junction tandem cells in the context of small molecule organic materials.

Two different organic electron donor materials, boron subphthalocyanine chloride (SubPc) and aluminium phthalocyanine chloride (ClAlPc) were used as donors in heterojunctions with C_{60} to create tandem cells for this thesis. These materials have been previously used for solar cells and the absorption spectra of the donor materials complement each other, making them good candidates for tandem cell architectures.

The design of the recombination layer between the cells is considered first, with silver nanoparticles demonstrated to work well as recombination centres for charges from the front and back sub-cells, necessary to avoid a charge build-up at the interface. The growth conditions for the nanoparticles are optimised, with the tandem cells outperforming the single heterojunction architecture.

Optical modelling is considered as a method to improve the understanding of thin film solar cells, where interference effects from the reflective aluminium electrode are important in determining the magnitude of absorption a cell can achieve. The use of such modelling is first demonstrated in hybrid solar cells based on a SubPc donor with a titanium oxide (TiOx) acceptor; this system is ideal for observing the effects of interference as only the SubPc layer has significant absorption. The modelling is then applied to tandem cells where it is used to predict the short-circuit current (J_{sc}) generation of the sub-cells, which is not accessible experimentally. Current-matching is then used to predict the J_{sc} of the complete tandem device.

As a support to the optical modelling, ellipsometry measurements of thin films of ClAlPc are presented. These films of known thickness are analysed to extract the complex refractive index for use in optical modelling calculations. A dependence of the complex refractive index on film thickness and substrate is also noted.

Finally, the external quantum efficiency (EQE) technique is considered as applied to solar cells, and an additional method is proposed to characterise current balancing in asymmetric tandem cells under illumination. This technique is verified experimentally by two separate sets of data.

PUBLICATION LIST

T. Howells, E. New, P. Sullivan, T.S. Jones
An External Quantum Efficiency Technique to Directly Observe Current Balancing in Tandem Organic Photovoltaics
Advanced Energy Materials, 2011. **1**(6): p. 1085-1088.

S. Schumann, C. Dearden, T. Howells, R. Pitt, R. Da Campo, P. Sullivan, T.S. Jones
Hybrid organic-inorganic solar devices based on the small molecule organic semiconductor boron subphthalocyanine chloride.
Submitted to Advanced Energy Materials

E.New, T. Howells, P.Sullivan, Ross A. Hatton, T.S. Jones
Enhancing the efficiency of small molecule tandem photovoltaics by modifying the photo-active layer morphology
Manuscript in preparation

1. INTRODUCTION

1.1. MOTIVATION

The world has seen a steady rise in global energy consumption, due to increased population and the growing industrialization of countries such as China and India. To date most of this rise has been met primarily with an increase in production based on non-renewable fossil fuels, with smaller contributions from nuclear, and even less from renewables such as hydroelectricity, wind, wave, and solar power, as shown in **Figure 1.1.**[1]

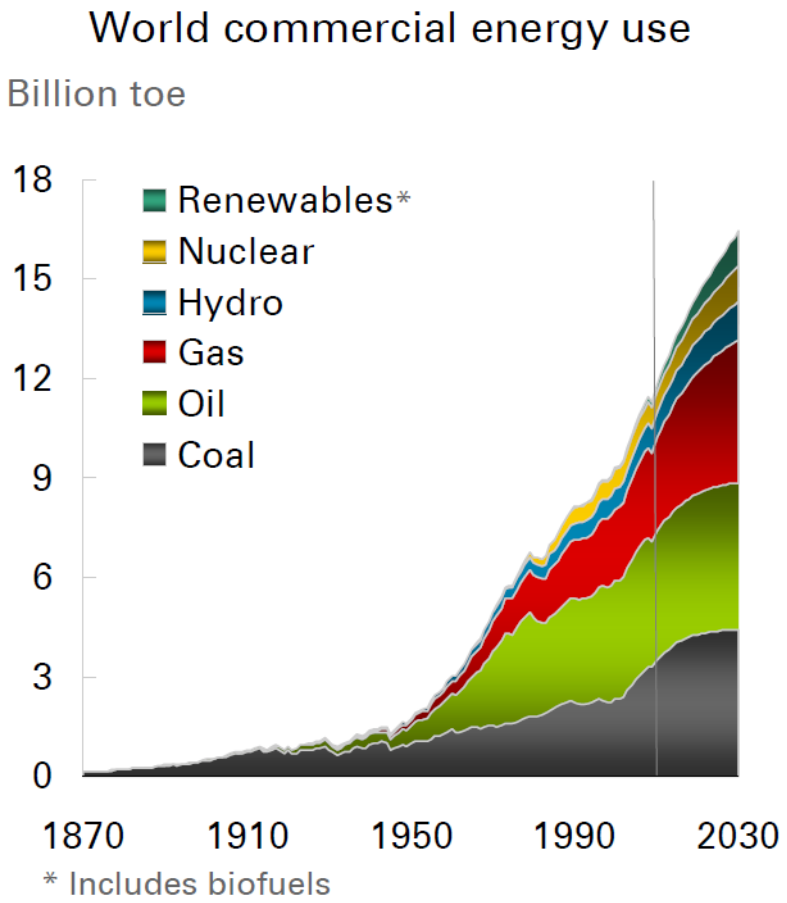

Figure 1.1. Energy consumption from 1870 to present day, showing generation type and including predictions up to 2030. Figure from BP Energy Outlook 2030.[1] 'Billion toe' stands for billion tonnes of oil equivalent.

However, this approach has a number of disadvantages. Not least, there is a limit to the amount of fossil fuels available; already the production of fossil fuels in many areas is dropping.[2] In addition, mining fossil fuels results in environmental damage and burning fossil fuels results in large releases of carbon dioxide. These are good reasons to reduce our reliance on fossil fuels; in the long term this replacement is an absolute necessity, and even in the shorter term gains can be made by reducing damage to the environment due to mining and potential global warming. The effects of global warming have already been observed as a rise in the mean global surface temperatures (**Figure 1.2**) and sea level, making this a pressing issue. [3]

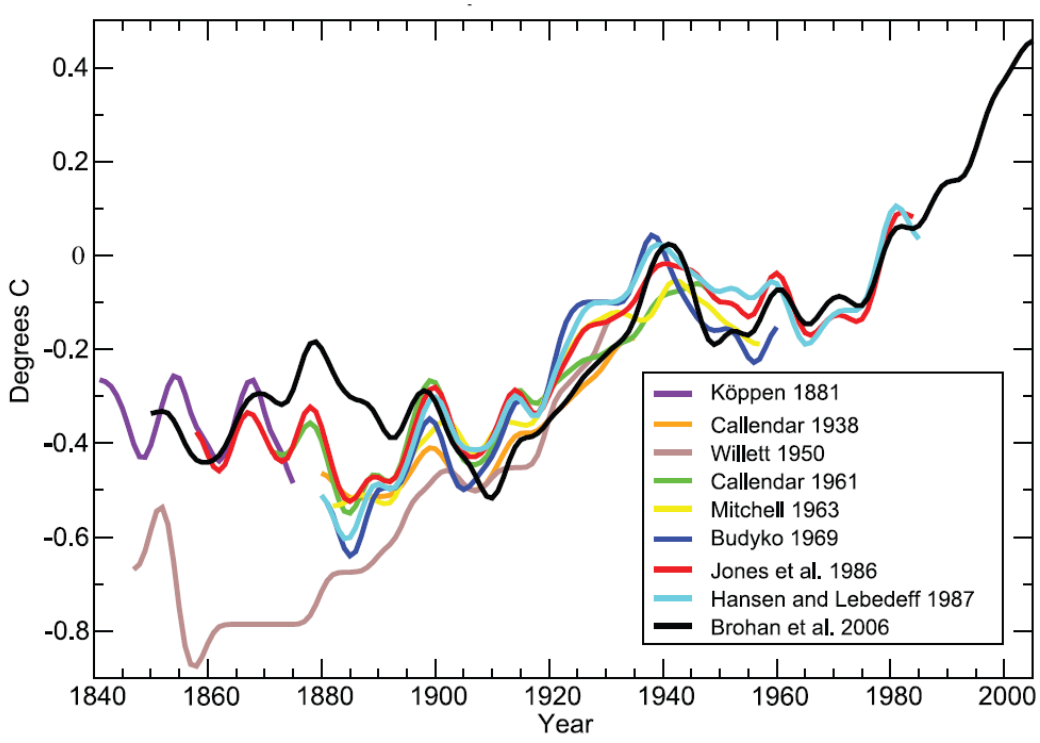

Figure 1.2. Published records of surface temperature change over large regions, showing the recent increase in temperature attributed to greenhouse gas emissions. Figure from fourth IPCC report, section 1.1 page 101.[3]

Currently, however, economics still dictates energy policy. Until renewable energy can generate electricity more cheaply than fossil fuels, utility companies and governments are unlikely to invest in replacing fossil fuels. As a result there is a lot of interest in the development of cheaper methods of renewable energy generation. Of these, solar energy is a very promising candidate. Calculations show that the amount of energy that reaches the earth's surface from the sun is around 10,000 times greater than total world energy consumption, meaning that there is more than enough potential to meet current energy demands.[4] Photovoltaic (PV) technology allows this energy to be converted directly into electricity, which is convenient for applications such as portable devices or panels based on buildings, where space is limited. High efficiency cells can also be used with concentrator technology to generate commercial scale electricity, and indeed is already seeing some use in areas such as California, where sunlight is stronger and more reliable.[5]

1.2. HISTORY OF SOLAR CELLS

The photovoltaic effect was first observed by Edmond Becquerel in 1839. The earliest cell was built by Charles Fritts, who coated selenium with a thin layer of gold to create a Schottky barrier device with a power conversion efficiency (PCE) of around 1%.[4] The modern form of semiconductor junction solar cells was patented in 1946 by Russel Ohl,[6] with the discovery of the p-n junction in crystalline silicon, and the first practical cells developed at Bell Laboratories with a diffused silicon p-n junction.[4] At first, the cells' use was very limited due to the high cost of producing the panels; the primary commercial use of the cells was for satellites, where cost was no object and the benefits of PV were well suited to the application. Cells based on

single junction monocrystalline silicon have since reached an efficiency of 24.4%,[7] but these cells are expensive due to the manufacturing process required – to create the large-scale, defect free crystals needed takes high temperatures and processing under high vacuum. While it is possible to instead use amorphous silicon to reduce the fabrication cost, this also leads to a lower cell efficiency of ~10%.[8] Silicon solar cells are sometimes referred to as 'first generation' cells.

The second generation for solar cells was the development of cells utilizing different inorganic materials, usually in thin films to try to reduce the overall processing costs compared to 'first generation' cells. Using combinations such as gallium arsenide (GaAs)[9] or cadmium telluride (CdTe)[10] allowed the growth of thin inorganic films whose band gap can be controlled, allowing tailoring to different parts of the solar spectrum. This then allowed the creation of the first multijunction devices, which are sometimes termed 'third generation' devices, where each junction absorbs a different part of the solar spectrum. This also reduces energy lost by thermalization of hot carriers.[4] These cells have reached very high PCEs around 41% when using a solar concentrator.[11] However, the low abundance of the materials used and processing methods mean these cells are still expensive. There are also environmental issues with the high toxicity of some of the elements used for these 'second' and 'third' generation cells.

The most recent generation of cells, labelled as 'Emergent Photovoltaics' by the National Renewable Energy Laboratory (NREL, US),[8] involves another shift in materials choice, driven partly by the development of organic semiconductors for optoelectronics, for example organic light-emitting diodes (OLEDs). These cells

employ organic semiconductor junctions or organic / inorganic hybrid junctions to generate a photovoltaic effect, and are more generally referred to as organic photovoltaics (OPV). They are sometimes also labelled ‘excitonic’ solar cells due to their method of operation, discussed in **Section 1.5**. The cells generally use a dye, or chromophore, to harvest sunlight. Hybrid cells use the high absorbance of some organic semiconductors to allow for thin and cheap absorbing layers, while still using an inorganic acceptor for their high stability and conductivity.[12]

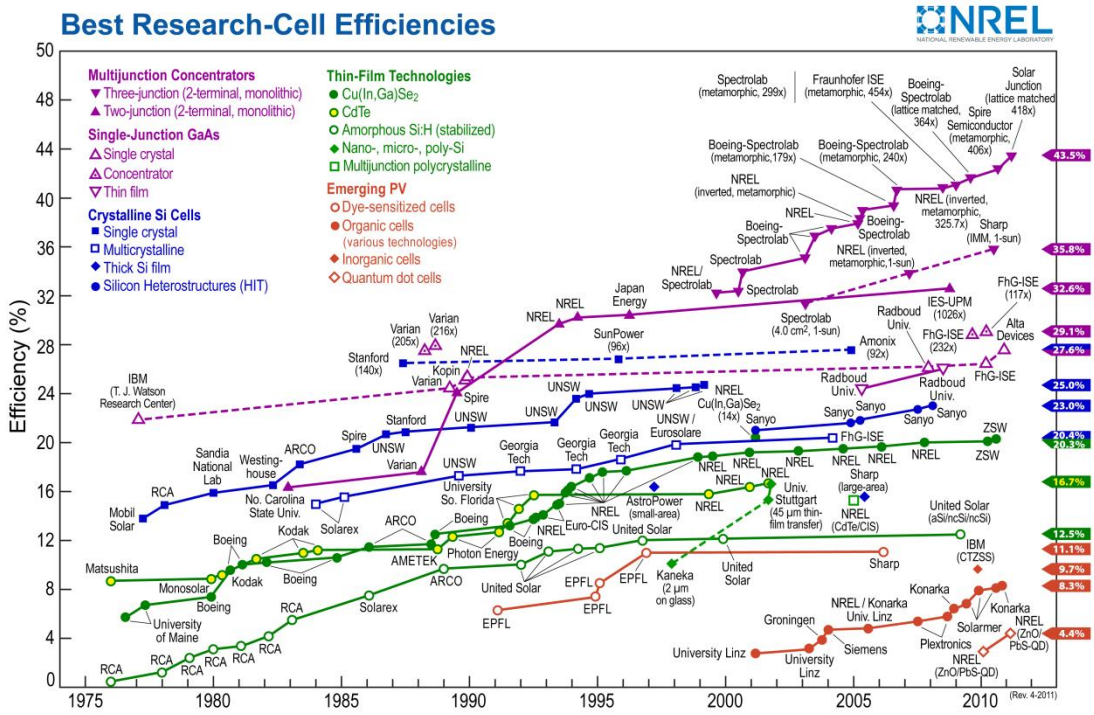

Figure 1.3. Research cell efficiencies from 1975 to 2011, showing the improvement in all technologies and the comparison between them. Figure compiled by the US National Renewable Energy Laboratory (NREL), from annual data collection.[8]

Since organic compounds are comprised primarily of the elements carbon, nitrogen, oxygen and hydrogen, all of which have a high abundance and can be manipulated at low temperatures, these compounds can be very cheap compared to inorganic

materials. While the efficiencies of these cells cannot yet match the efficiencies of the inorganic cells, the use of low-cost materials and fabrication techniques mean the cost-per-watt can be competitive.[13] An overview of the efficiencies of all types of PV cell in the laboratory is shown in **Figure 1.3**.

1.3. ORGANIC SOLAR CELL DEVELOPMENT

Organic cells can generally be divided into three categories; dye-sensitised solar cells (DSSCs), small molecule cells, and polymer cells. In addition to this, a cell which uses both organic and inorganic materials as the active layers is usually termed a hybrid cell; generally the organic material is the donor and the inorganic material the acceptor. DSSCs were invented in 1991 by O'Regan and Grätzel and initially obtained PCEs around 7.4%.[14] By 1994 these cells had improved to around 10%.[15] This had progressed to 10.4% (certified) by 2001, and more recently to 11.1% in 2005.[16] These cells are based on redox chemistry, using a dye in an electrolyte and a solid electron acceptor such as titanium dioxide (TiO_2). The dye absorbs light, becomes excited, and transfers charge to the titanium dioxide. The dye then oxidises the electrolyte surrounding it to neutralize itself; the oxidised electrolyte diffuses to the counter electrode where it is reduced, completing the circuit. This style of device will not be discussed further in this thesis.

Polymer and small molecule cells are based on largely the same design principles. The operating principles of these cells will be discussed in section 1.4. Polymer layers are usually solution processed, while small molecules are spin-coated, spray-painted, or more commonly vacuum deposited using organic molecular beam deposition (OMBD) depending on their properties.

Before 1986, organic cells were based on thin films of single layers of small molecules, such as porphyrins or phthalocyanines.[17] These Schottky based devices are very inefficient in organics since exciton dissociation is thermal or defect-driven, and in organics the thermal contribution is small, unlike inorganic semiconductors. Defect-driven dissociation is inefficient and large numbers of impurities often lead to a breakdown of the electrical characteristics useful in solar cells. In 1986, Tang et. al. developed the two-layer donor/acceptor heterojunction architecture to improve exciton dissociation.[18] At the heterojunction between materials excitons can dissociate into free charges much more efficiently than in a Schottky cell. This early cell used Copper Phthalocyanine (CuPc) and a perylene tetracarboxylic derivative, 3,4,9,10-perylenetetracarboxylic bis-benzimidazole (PTCBI), to give a PCE of about 1%. Successive improvements in materials since then have improved the efficiency of such devices, such as the use of C_{60} as an acceptor, which conducts relatively well for an organic, absorbs at shorter and UV wavelengths and has favourable energy levels for exciton dissociation with many organic donor materials. Similar cells based on an oligothiophene derivative : C_{60} junction have recently managed 4.9%.[19]

Two compatible ways to improve organic devices further are bulk heterojunction cells and tandem cells. The first bulk heterojunction device was created by Heeger et. al. in 1995 by spin coating of a polymer, poly(2-methoxy-5-(2'-ethyl-hexyloxy)-1,4-phenylene vinylene), or MEH-PPV, with a soluble fullerene.[20] By spin coating both at the same time, instead of forming a single junction between layers, the polymer and fullerene separated into domains such that the distance from any molecule to an interface is always small. This helps greatly for dissociating excitons, and recent cells have reached high efficiencies of 7.4%.[21] The random nature of the

domains, however, introduces a problem of charge transport paths to the electrode which limits these devices. There have recently been attempts to improve charge transport in such a bulk heterojunction using polystyrene spheres in a near-perfect packing arrangement as a scaffold to create a 3D interpenetrating network of donor and acceptor materials.[22] In this case, since the spheres and the voids around them are continuous, when filled with the donor and acceptor materials both materials have continous charge transport paths throughout the layer, while at the same time minimizing the distance a charge can be generated away from an interface. This allows much thicker layers, and thus more absorption, by compensating for the short exciton diffusion length.

Creating a tandem cell involves stacking extra layers to create a second cell atop the first cell. This allows for greater absorption while keeping the individual cells, or sub-cells, thin to allow for exciton dissociation. By utilizing differing materials in the front and back cells the tandem cell can absorb much more widely than a single cell and thus obtain higher efficiencies. The first tandem cell was created by Hiramoto et al in 1990, and consisted of two metal-free phthalocyanine : perylene tetracarboxylic derivative sub-cells separated by a gold interstitial layer. This discontinuous layer is used to prevent charge build-up between the sub-cells in the device by providing recombination centres for the charges from either side of the interface. This first cell demonstrated primarily the potential for improving the voltage of the cell, going from 0.44V for a single cell to 0.78V in the tandem cell.[23] The next contribution was made by Forrest et al. who demonstrated some uncertified 5.7% cells based on copper phthalocyanine (CuPc) : C_{60} heterojunctions with silver nanoparticles as recombination centres in 2004.[24] Since then there have been multiple contributions to small molecule tandem cells from Maennig et al.[25] ,

Triyana et al.,[26] and Cheyns et al.[27], the latter achieving efficiencies of 5.15% in 2010 using a combination of phthalocyanine and subphthalocyanine derivatives with fullerene as the acceptor.

There has also been some progress in creating solution-processed tandem cells, with the first part-solution processed tandem cell created by Kawano et al. in 2006.[28] This utilized two sub-cells of poly[2-methoxy-5-(3',7'-dimethyloctyloxy)-1,4-phenylene vinylene], or MDMO-PPV, with the fullerene derivative [6,6]-phenyl-C_{61} butyric acid methyl ester (PCBM), and a 20 nm ITO recombination layer, achieving an efficiency of 3.1%. This was followed in the same year by Dennler et al. who created a Zinc Phthalocyanine (ZnPc):C_{60} cell atop a poly[3-hexylthiophene-2,5-diyl](P3HT) : PCBM cell with a gold recombination layer, achieving only 2.3% efficiency but significantly boosting the voltage of the cell.[29] Work by Colsman et al.[30], Janssen et al.[31], and Hadipour et al.[32] resulted in further development, with the first fully solution processed cell grown by Gilot et al. in 2007.[33] Work by Kim et al. demonstrated a 6.5% device in 2007, based on poly[2,6-(4,4-bis-(2-ethylhexyl)-4*H*-cyclopenta[2,1-b;3,4-b']dithiophene)-*alt*-4,7-(2,1,3-benzothiadiazole)] (PCPDTBT) with PCBM in one cell and P3HT with [6,6]-phenyl-C_{71} butyric acid methyl ester ($PC_{70}BM$) in the second cell.[34]

Hybrid cells have more in common with the workings of polymer and small molecule cells. The overall aim of such systems is to utilize the strengths of each material while minimizing the drawbacks by combining them;[35] organic materials often have very high extinction coefficients and are cheap to produce, while inorganic materials, such as TiO_2, can have good long-range charge transport and high stability.[36] This thesis is concerned primarily with all-vacuum deposited small molecule tandem cells, with the exception of the hybrid single cells grown by Chloe

Dearden. These are of interest for optical modelling, and were partly spin-coated; these devices are considered in **Section 4.4.2.**

1.4. SOLAR CELL THEORY

1.4.1. THE PHOTOVOLTAIC EFFECT

When light is absorbed by a material, an electron in the material is excited; the energy gained being equal to the energy of the absorbed photon. If enough energy is absorbed, this results in the photoelectric effect – when a high energy photon transfers enough energy to completely remove an electron from its material. This process was first explained by Einstein in his 1905 paper, and was the first proof that light existed in discrete quanta.[37] If the energy is not enough to completely remove the electron from the material, the electron is instead left in an excited state. In some situations these excited states quickly relax back to their ground state by internal conversion, but in a photovoltaic device the electrons are excited to a relatively stable charge-carrying state, and a built-in asymmetry causes the electrons to move through the device. This generates a current, which can be pushed through an external loading circuit to do work.

1.4.2. SEMICONDUCTORS

The origin of the stable charge-carrying state is the electronic structure of the absorbing materials, which originates in the way atoms and electrons interact with each other. A lone atom has a number of electron orbitals at varying energies, with its' electrons (ideally) filling the lowest energy ones; the defined levels in this case are a result of quantization.[38] In a solid, however, the situation is more complicated.

A common place to start is to consider the effect of a 1D periodic electrostatic potential on the 1D free electron model. In this case, Bragg reflection from the lattice splits the plane wave solutions into two standing waves, one which places a lot of electrons onto the same sites as the ions and one which places electrons in-between the ions. These states have similar kinetic energies but differing potential energies; this leads to an energy gap in which there are no eigenstates for electrons, a 'forbidden' region. This allows us to segment **k**-space into a series of zones, each of measure $2\pi / a$, where a is the lattice spacing; these are called Brillouin zones. The details and mathematics of k-space and Brillouin zones can be found in numerous introductory solid-state textbooks. [38, 39]

Each lattice unit cell can thus has its own set of Brillouin zones, which in an infinite repeating lattice are identical. Each zone corresponds to a 'band' in the crystal's electronic structure. When extended to three dimensions, it is common for zones to overlap; the result is considered as a single band. The electrons in the material occupy the bands starting at the lowest energy and working up in energy, as displayed in **Figure 1.4**. The energy of the level the electrons fill up to in the ideal case (no electron having more energy than necessary) is called the Fermi energy. The characteristics of the materials emerge from the filling of the band structure. A partly empty band provides many states for an electron to move into, allowing easy conduction, whereas an electron in a full band cannot change its' momentum without jumping into a different band. Thus, if the highest occupied band is only partly full, the material is a metal, as shown on the left in **Figure 1.4**. If the highest occupied band is completely full the material is an insulator, as shown on the right in **Figure 1.4.**

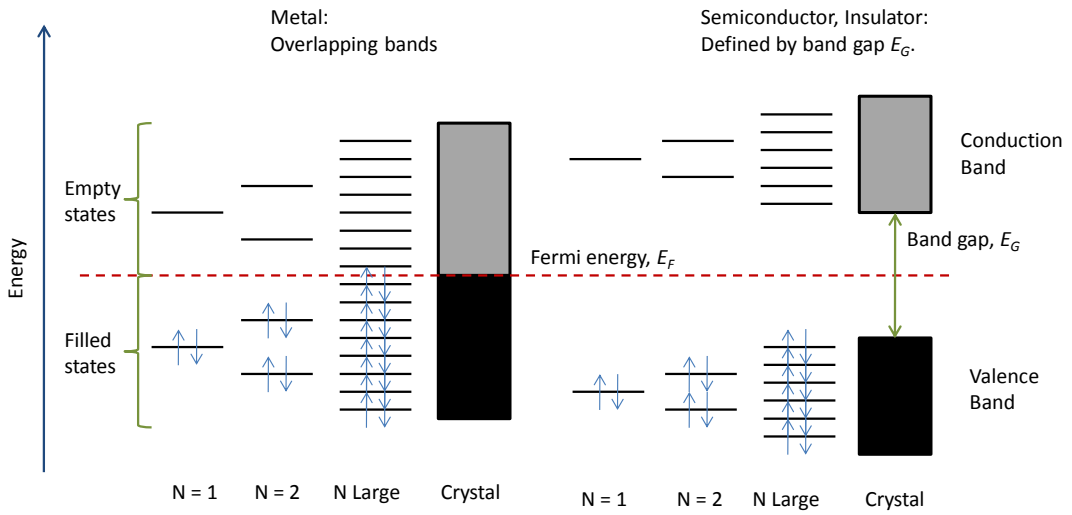

Figure 1.4. Representation of the formation of band structures as the number of atoms brought together increases.

In non-metals, the energy difference between the top of the highest occupied band and the bottom of the next available band is the band gap, E_g. The band gap originates from the electron orbitals of the element or molecule that constitutes the lattice. In the case of Silicon, for example, each atom contains eight sp states, four of which are filled. In a crystal, however, the Silicon is bonded to surrounding atoms; the energy levels interact to form four bonding and four (higher potential energy) antibonding levels. Silicon's four electrons are sufficient to completely fill the bonding levels, with the antibonding levels left empty. The full band is termed the valence band, as the electrons are bound to their atoms tightly, while the first free band is the conduction band, as electrons in it can move freely and conduct. A semiconductor occurs when the band gap is small enough to be overcome by thermal excitation, and some electrons are promoted from the valence band to the conduction band. The probability of finding an electron in the conduction band at a set temperature is described by Fermi-Dirac statistics.[4] The small number of such

electrons leads to the low conductivity of semiconductors, and the greater concentration at increased temperatures leads to a higher conductivity for semiconductors; this is in contrast to the lower conductivity with temperature found in metals as a result of increased scattering of electrons by phonon interactions.

In organic semiconductors the situation is slightly different as organic semiconductors are made of molecules rather than atoms. The molecular orbitals instead define the energy structure, and the energy levels are not usually defined as bands as there are not enough states close together to form a near-continuum as seen in inorganic semiconductors. Instead of referring to band edges, Highest Occupied Molecular Orbital (HOMO) and the Lowest Unoccupied Molecular Orbital (LUMO) are used to reflect the differing electronic structure, as in **Figure 1.5**. For such organic semiconductors the π-bonding orbitals usually combine to create the HOMO while the π-antibonding orbitals create the LUMO, with the difference between the two defining the band gap.

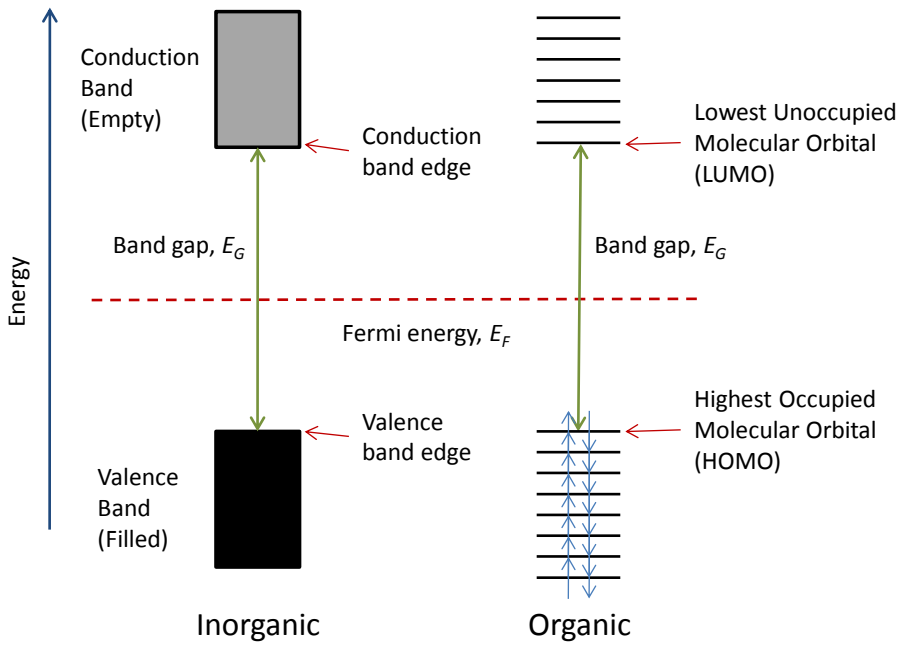

Figure 1.5. Comparison of electronic structure between organic and inorganic semiconductors.

1.5. DEVICE OPERATION IN ORGANIC PHOTOVOLTAICS

The process of generating power from a photovoltaic device can be split into a number of stages. Firstly, light is absorbed, and excitons are generated; the excitons diffuse and dissociate, usually upon reaching an interface. The electrons and holes generated by dissociation are then transported to different electrodes to generate a photovoltage; in the presence of an external circuit this drives current around it. These stages are shown below in **Figure 1.6**, and further explained in the relevant sections.

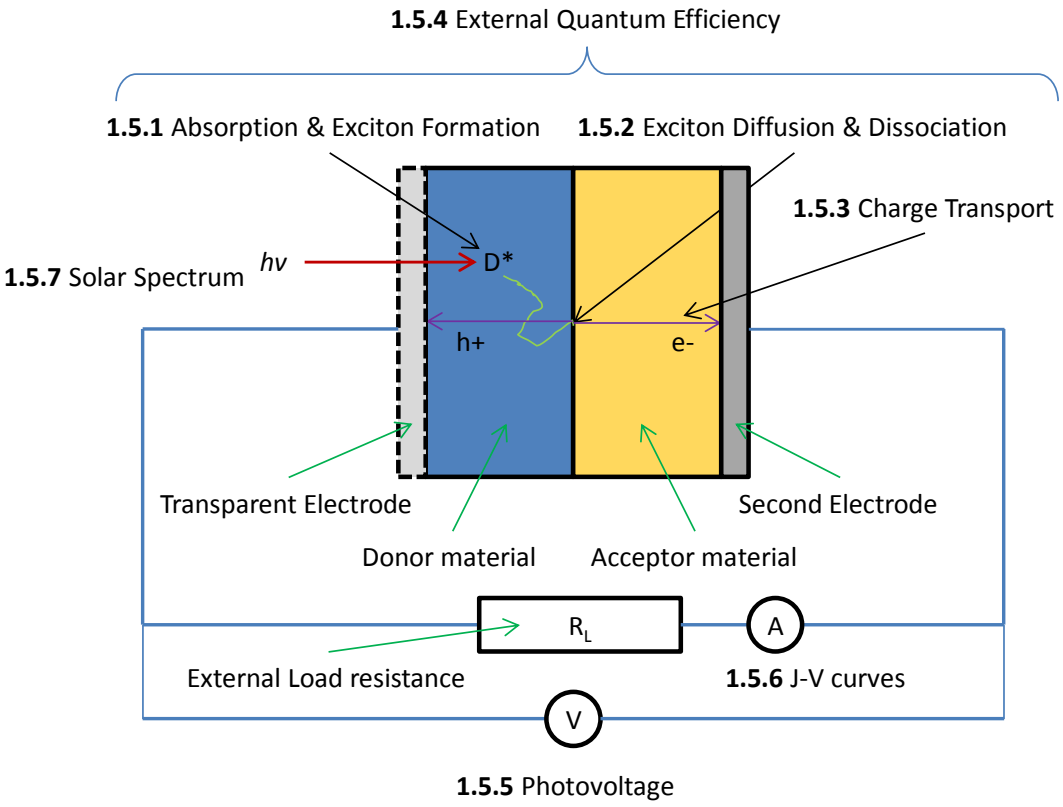

Figure 1.6. Schematic representation of power generation in an organic solar cell, relating each process to the relevant section. D* represents an exciton, e- an electron and h+ a hole, while A and V represent current and voltage meters respectively.

1.5.1. ABSORPTION & EXCITON FORMATION

Absorption in semiconductors occurs when a photon promotes an electron from the valence band / HOMO to the conduction band / LUMO. The electronic structure of the semiconductor thus determines what part(s) of the spectrum can be readily absorbed. Promoting from the valence band/HOMO leaves behind a vacancy in the level, usually known as a 'hole'. Since there are generally far fewer holes than electrons in the valence band / HOMO, it can be convenient to represent the hole as a particle with positive electric charge. This hole can form a Coulombic attraction with the electron that was promoted out of it, leading to a bound state called an 'exciton'. Carriers in these states cannot yet contribute to a photovoltaic effect.

The strength of the binding between hole and electron depends on the properties of the material. In organic semiconductors this bond tends to be strong due to the low dielectric function and weaker interatomic electronic interactions, unlike covalently bonded inorganic semiconductors such as silicon. The lower dielectric function means less electric field screening, and causes the potential wells of the charges to be larger (shown in **Figure 1.7**), while the weaker interatomic interactions tend to spatially restrict the electron wave function, localizing the electron in the potential caused by its matching hole.[40]

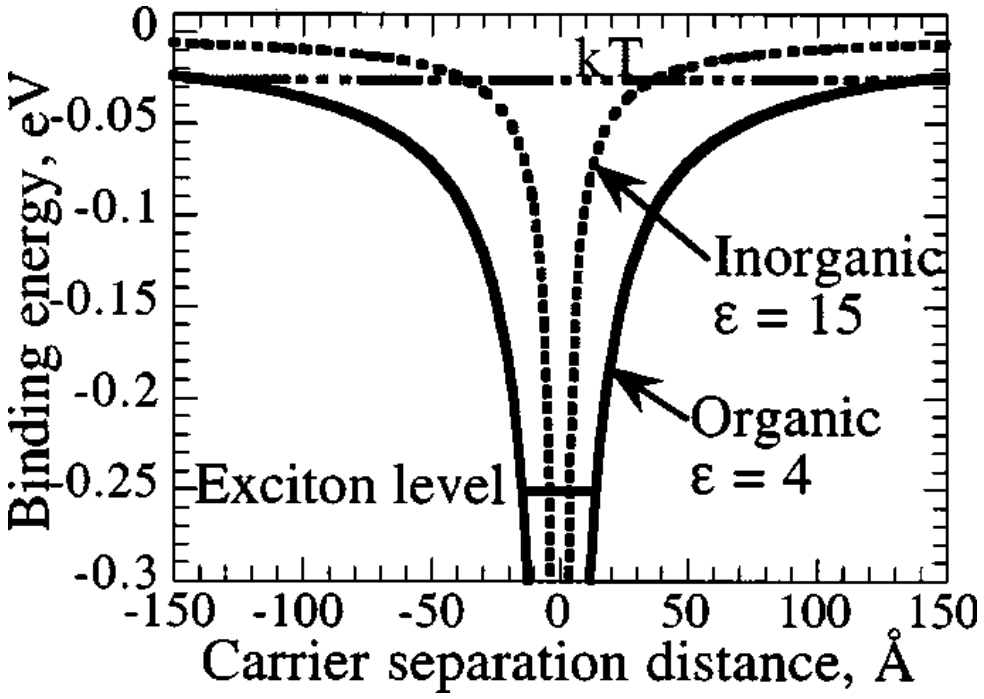

Figure 1.7. Binding energy of two isolated charged particle with separation distance inside a semiconductor. The interaction is shown to be stronger at longer distances in low-dielectric organic materials. Figure adapted from Gregg et al.[40]

This leads to organic materials creating tightly bound Frenkel excitons, which are localised on the absorbing molecule.[41] The weaker interaction in inorganic materials lead to Mott-Wannier excitons,[42] where the charges are still bound but not on the same molecule, as shown in **Figure 1.8**. The Bohr radius of the relevant charge carrier can be used to show the restriction difference between Frenkel and Mott-Wannier excitons. Intermediate states are possible based on the binding energy of the exciton and dielectric constant of the material.

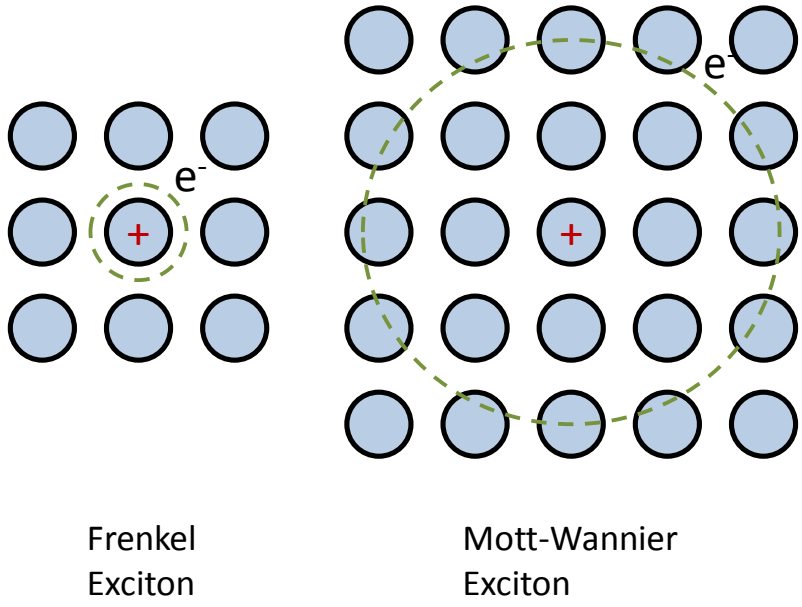

Figure 1.8. Different types of exciton as separated by their Bohr radius. Frenkel excitons are localised on a single molecule while Mott-Wannier excitons are much less localised.

The existence of Frenkel excitons shows up as additional states in the electronic structure slightly above the valence band / HOMO for holes and slightly below the conduction band / LUMO for electrons. The energy difference between these states and the HOMO / LUMO constitutes the binding energy E_B of the exciton, as shown in **Figure 1.9**. This is the amount of energy required to break the coulombic attraction and generate free charges, as in **(1.1)**:

$$E_B = E_1 + E_2 \tag{1.1}$$

Where E_1 and E_2 are the energy differences for electrons and holes, respectively. The binding energy of Mott-Wannier excitons is low enough that it can be overcome easily by thermal excitation. However, for Frenkel excitons in organic materials this is not the case; binding energies are often greater than 0.1 eV. Comparing to the average energy of a molecule at room temperature, k_bT or ~0.025 eV, these binding

energies are too high for thermal excitation to break the bond, and require an additional impetus to result in dissociation.

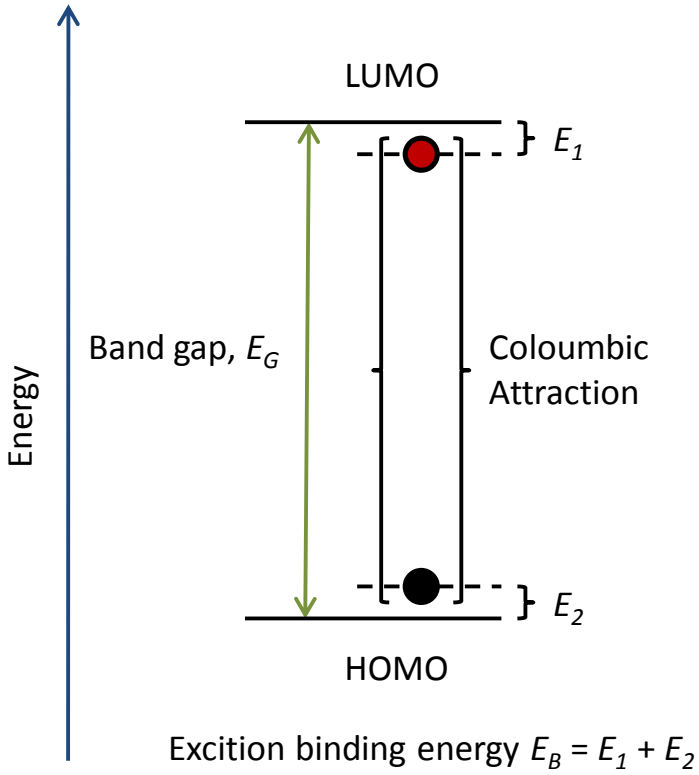

Figure 1.9. Diagram showing the position of the coloumbically bound states that form and lead to excitons.

1.5.2. EXCITON DIFFUSION & DISSOCIATION

The impetus to dissociate an exciton is usually provided by creating a heterojunction between two organic semiconductors. The second semiconductor is chosen so that the electron from an exciton can drop down into it (or a hole rise from it depending on the material containing the exciton), releasing the energy difference between the LUMO or HOMO levels and breaking the bound state, as in **Figure 1.10**. As shown

in the figure, dissociation occurs in excitons from the donor if $\Delta LUMO > E_B(donor)$, and in excitons from the acceptor if $\Delta HOMO > E_B(acceptor)$.

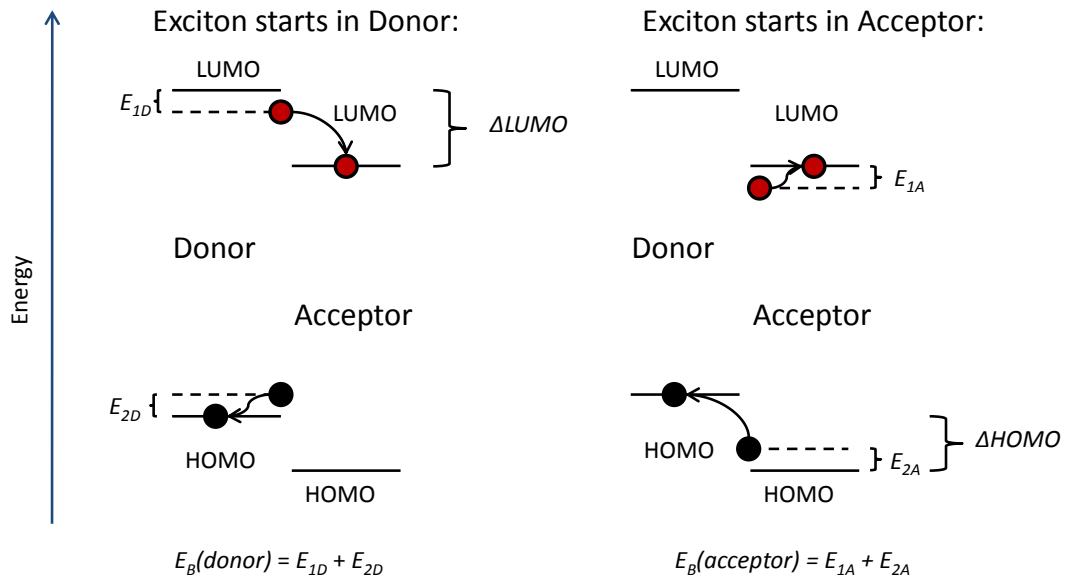

Figure 1.10. Effect of energy levels on dissociation at a Donor/Acceptor interface.

However, this method of dissociating excitons requires the exciton to reach the interface between the two semiconductors. An exciton has, overall, no charge, so an external electric field cannot be used to either dissociate the exciton or drive it towards an interface. Instead, excitons can only reach the interface by energy transfer to adjacent molecules. This process is not driven, but rather a random hopping process and as such is governed by the diffusion equation. Written to accommodate exciton generation and recombination in a general bulk case the 1-D time-dependant exciton diffusion equation is given as **(1.2)**.[43]

$$\frac{\partial n(x,t)}{\partial t} = g\alpha N_0(t)(1-R)e^{-\alpha x} - \frac{n(x,t)}{\tau} + D\frac{\delta^2 n(x,t)}{\delta x^2} - F(x-x_{int})n(x,t) \quad (1.2)$$

Here, $n(x,t)$ is the time- and position-dependant exciton density. The first term represents the exciton generation rate with depth in the material, assuming an exponential drop-off in absorption; g the efficiency of exciton formation, α the absorption coefficient of the material, $N_0(t)$ the photon flux, and R the reflectivity of the top of the cell. The second term represents recombination, with average time τ. The third term represents exciton diffusion, and the final term represents dissociation at the heterojunction, where $F(x\text{-}x_{int})$ is the dissociation rate of excitons at the interface. Solving **(1.2)** for steady illumination ($\delta n/\delta t = 0$) with boundary conditions n(x=0) = 0 (drain of excitons at ITO electrode) and $n(x=\infty) = 0$ (No absorption in the bulk because of the exponential drop-off) leads to **(1.3)**. This is still a slightly simplified case, in the case of multiple organic layers or metal interfaces the boundary conditions should be modified, and the exponential drop-off term replaced with a more accurate representation.

$$n(x) = \frac{g\alpha N_0(1-R)}{D}\frac{\alpha L_D^2}{1-(\alpha L_D)^2}(e^{-\alpha x} - e^{-\left(\frac{x}{L}\right)}) \tag{1.3}$$

L is the thickness of the layer. During this derivation we also define the quantity L_D, as below in **(1.4)**.

$$L_D = \sqrt{D\tau} \tag{1.4}$$

L_D represents the average distance an exciton will travel via random hops in an average lifetime. This is useful because this then defines an optimal thickness for the absorbing layer; excitons generated further from the interface will have a steadily decreasing chance of reaching the interface. As a result, increasing the thickness of the layer will have a strongly diminishing contribution to current generation, while

still increasing the resistivity of the layer, meaning the optimal thickness will usually be close to the diffusion length of the excitons in the material. If enough information about the layer is known the optimum layer thickness can be calculated by solving the exciton diffusion equation.

1.5.3. CHARGE TRANSPORT

After generating free charges at the interface, these charges must still reach the external circuit. Generally, in an OPV device the holes are transported through the electron donor material and the electrons through the electron acceptor material. While charge mobilities in crystalline inorganic materials can be very high due to the long range order, intermolecular bonding in organic semiconductors is usually much weaker, and they are often polycrystalline or amorphous. This leads to charge mobilities that are typically orders of magnitude lower than for inorganic crystalline semiconductors, due to the charges having to jump from one domain or molecule to another. This sort of structure is also likely to increase the number of trap or defect sites that impede charge transport.

The final point of interest is the interaction with the electrodes. The positioning of the Fermi level (or workfunction) of an electrode relative to the organic material will affect the carrier extraction barriers at the interface. When the metal electrode is brought into contact with the organic, the organic will sit in the potential of the surface dipole of the metal, leading to a shift in the effective vacuum level.[44] The contact between the two materials can sometimes cause a second interfacial dipole to form, due to chemical reactions, electron cloud redistribution or other reasons.[44]

This is noted as a second shift in the vacuum level, and commonly referred to as the interface dipole. After taking account of the surface dipoles, the Fermi level in the two materials will tend to align, as can be justified by considering the case of non-aligned Fermi levels: One Fermi level will be at a higher energy than the other, and so electrons will be more likely to transfer to the lower energy state, on average, by crossing between the materials. This leads to an effect called band bending, where electrons added or removed from the organic shift the local potential in a certain thickness from the interface. This can act to increase or reduce the carrier injection / extraction barriers depending on the nature of the band bending, as shown in **Figure 1.11**. The energy level shifts and barrier height can be measured utilising UPS.[44]

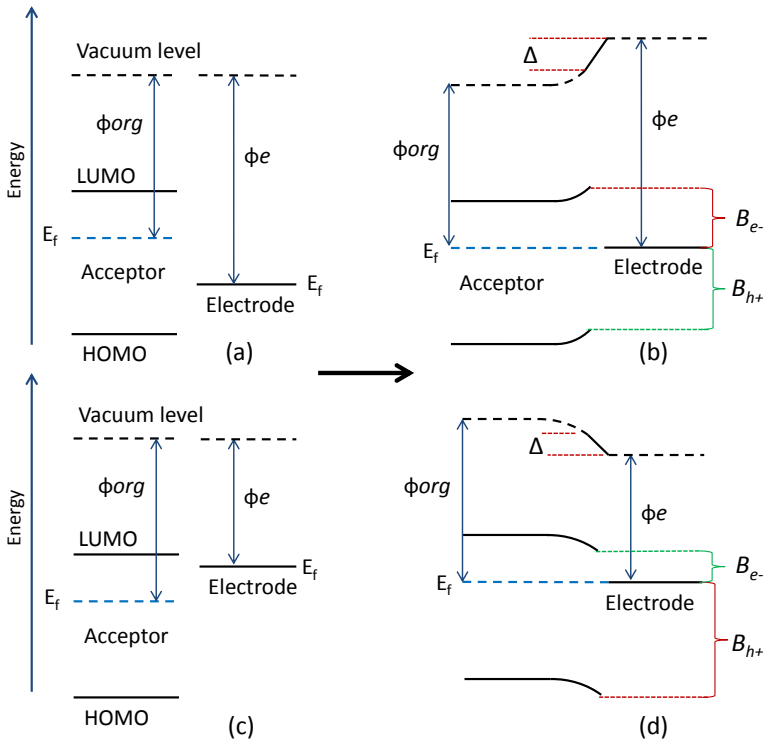

Figure 1.11. Bringing an organic (workfunction ϕorg) into contact with a metal electrode (workfunction ϕe). In (a) and (b) the metal has a higher workfunction than the organic, in (c) and (d) the metal is lower workfunction. (a) and (c) show the materials' energy levels before contact, (b) and (d) after, with Δ indicating the interface dipole. The barriers B_{e-} and B_{h+} are shown in red or green depending on whether they were increased or decreased by band bending.

Recent work on electrode modification has involved using ultrathin interlayers such as metal oxides that give a good match to the energy levels of the organic semiconductor, while still allowing charges to transfer easily from them to the metal electrodes. [45, 46]

1.5.4. EXTERNAL QUANTUM EFFICIENCY

By assigning a quantum efficiency to each of these processes, we can define the overall quantum efficiency, usually termed the external quantum efficiency (EQE).[4] This is simply the product of the individual quantum efficiencies, as in **(1.5)**.

$$EQE = Q_A Q_{Diff} Q_{Diss} Q_T \tag{1.5}$$

Here, Q_A is the quantum efficiency of absorption, Q_{Diff} that of exciton diffusion to an interface, Q_{Diss} the efficiency of the dissociation at the interface, and Q_T the efficiency of charge transport of the resultant free charges to the electrode. This overall quantum efficiency can often be measured directly, which is further discussed in **Chapter 5**. If the incoming light intensity at each wavelength is known, the EQE allows calculation of the maximum expected photocurrent, J_{sc}, from the cell, as in **(1.6)**.

$$Jsc = q_e \int_0^\infty NP(\lambda) EQE(\lambda)\, d\lambda \tag{1.6}$$

EQE(λ) is the quantum efficiency for a particular wavelength of light, and *NP(λ)* is the number of photons arriving at that wavelength, as calculated from the intensity spectra, while q_e is the electronic charge. This integral represents the maximum photocurrent that can be measured from the cell with the specified illumination. However, this does not define the efficiency of the cell or the power that can be extracted from the device. Power (*P*) in direct current electronics is equal to voltage (*V*) multiplied by current (*I*), as in **(1.7)**; thus, we need to know both the voltage and current at the same time.

$$P = VI \tag{1.7}$$

1.5.5. PHOTOVOLTAGE

The origin of the photovoltage in organic semiconductors is generally accepted to be related to the HOMO-LUMO offset of the donor-acceptor heterojunction, given in **(1.8)** as presented by Cheyns et al.[47] The model used predicts the maximum photovoltage a cell can produce, and accounts for the interface gap between HOMO and LUMO levels, band bending in the donor and acceptor materials (BB_D and BB_A respectively) and the energy losses at the electrodes ($\Delta\Phi_D$, $\Delta\Phi_A$) due to the position of the work function relative to the charge-carrying band.

$$V_{oc} = |HOMO_D - LUMO_A| + BB_D + BB_A - \Delta E_D - \Delta E_A \tag{1.8}$$

These terms are shown graphically in **Figure 1.12**. The energy level difference between the HOMO of the donor and the LUMO of the acceptor is ideally maximized to improve the voltage while the LUMO-LUMO (*ΔLUMO*) and HOMO-

HOMO (*ΔHOMO*) differences are kept sufficiently large to dissociate excitons that reach the interface, the exact difference required determined by the binding energy of the excitons in the material. The choice of heterojunction can strongly affect the maximum voltage and thus power obtainable from a set of materials; materials for OPV devices are thus usually chosen in pairs due to the heterojunction and absorption requirements.

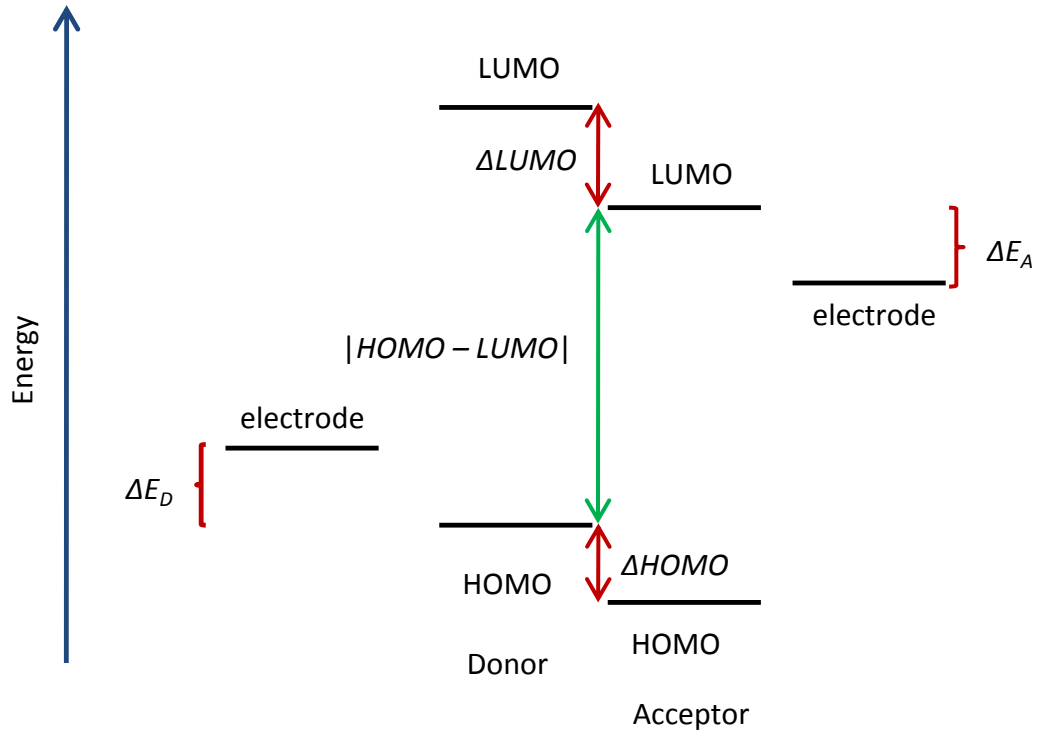

Figure 1.12. Simplified origin of photovoltage in organic heterojunctions. Effects are shown in green or red depending on whether they aid or reduce the photovoltage.

1.5.6. J-V CURVES

In the previous section the photovoltage was introduced as the maximum obtainable photovoltage, dependant on the energy levels of the donor-acceptor heterojunction. In practice, the maximum photovoltage a cell can generate occurs when there is

infinite load resistance between the contacts. In this situation no current flows through the external circuit, and the only limitation to the charge build-up at the electrodes is internal, represented by the reverse current flow due to the potential, J_{dark}. The maximum photovoltage occurs when this internal flow is equivalent to the generated photocurrent, and is called the 'open-circuit voltage', denoted as V_{oc}. The other extreme is when the electrodes are in direct contact, with a resistance very close to zero; in this case, no photovoltage can build-up across the contacts since the current flows immediately from one to the other to reduce the potential. However, the photocurrent in this situation is maximised due to the minimal resistance and lack of reverse current, and this situation is termed the 'short-circuit current', denoted J_{sc}. This maximum photocurrent is what is predicted using EQE and the illumination spectra.[4]

It is worth noting that neither of these situations can result in useful work. If the resistance is truly zero in the short circuit case, and truly infinite at open circuit, then in each case either the voltage or current is zero. From **(1.7)** it can be seen that if either of these quantities is zero the power output is also zero. Since solar cells are interesting for their power output, this means that these measurements alone are insufficient. However, for load resistances between infinity and zero, the power can be defined since both quantities will be non-zero and depend on the load resistance applied.

The reverse current, J_{dark}, is often compared with the current that flows through a solar cell in the dark under an applied voltage, hence the name. Most solar cells behave like a diode in the dark, admitting a much larger current in forward bias than in reverse bias. This rectifying behaviour is expected due to the asymmetric junction

used for charge separation. If treated as an ideal diode, the dark current density J_{dark} will obey **(1.9)**.[4]

$$J_{dark}(V) = J_0(e^{\frac{q_e V}{k_b T}} - 1) \tag{1.9}$$

J_0 is a constant, V is voltage, T temperature, q_e the electronic charge and k_b the Boltzmann constant. This current will have the opposite sign to the photocurrent. The photocurrent will, in this analysis, be independent of applied voltage – the response of the cell to varying applied voltages (which is equivalent to varying resistive loads) can then be approximated as the sum of the photocurrent, measured at short circuit, and the dark current; this is known as a superposition approximation, as in **(1.10)**:

$$J = J_{dark} - J_{sc} \tag{1.10}$$

The convention here can be taken either way. Either the standard engineering convention for diodes can be used, making J_{dark} positive, or the photocurrent can be defined as positive. In this case the standard engineering convention has been used. The effect of the photocurrent J_{sc} in this case is simply to shift the dark curve, although this is an approximation. This idealised case is shown in **Figure 1.13**.

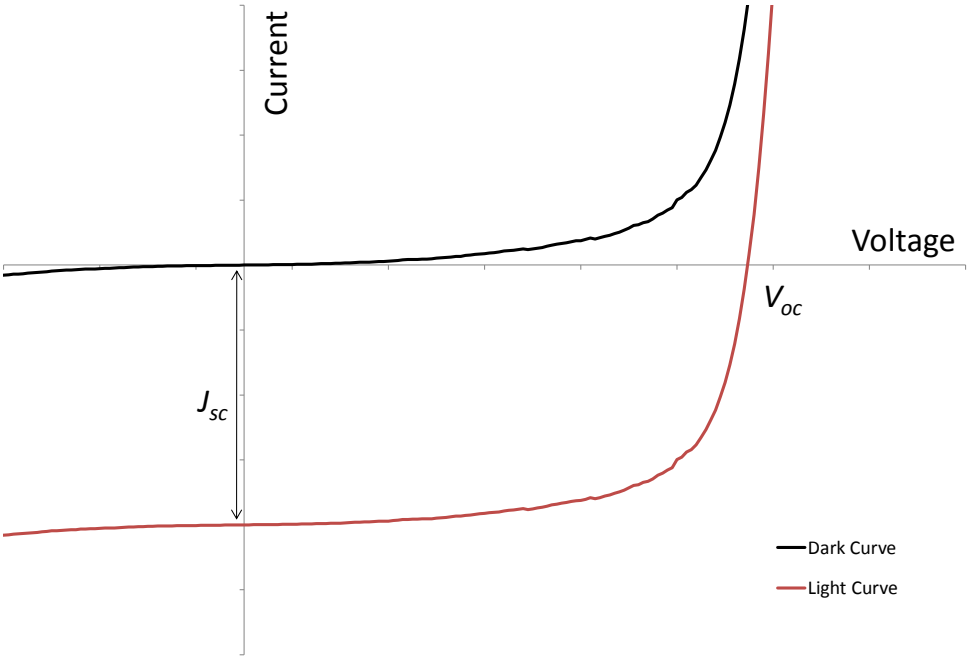

Figure 1.13. Ideal shifting of a dark curve by the short-circuit current.

In a less idealised case, losses also occur via resistance of the contacts and leakage inside the device. A solar cell can thus be represented equivalently as a current generator in parallel with a diode, with the two parasitic resistances R_S and R_P, representing the contact resistance and the resistance to leakage inside the device respectively. This equivalent electronic circuit is shown in **Figure 1.14**.

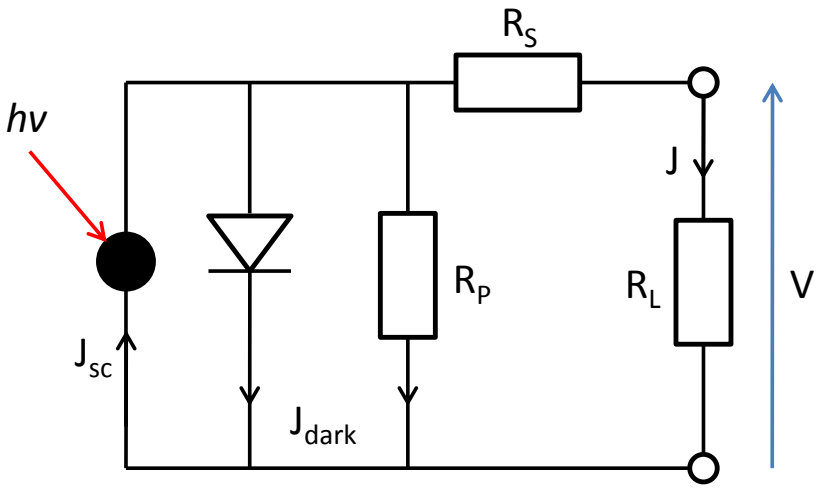

Figure 1.14. Equivalent circuit diagram for a solar cell, including parasitic resistances.

The series resistance R_S is a more significant problem at higher current loads, as can be rationalised from using Ohm's law and **(1.7)** to calculate the power dissipated due to R_S, as in **(1.11)**. R_S would ideally be zero to reduce power dissipation inside the device.

$$P = VI = I^2R \tag{1.11}$$

The parallel, or shunt, resistance R_P arises from leakage between contacts or around the edge of the device, and is ideally infinite, or at least very large; a poor parallel resistance is equivalent to poor rectifying behaviour in devices. Both of these resistances lead to changes in the shape of the J-V curve, and reduce the maximum obtainable power. The maximum power output of a cell occurs where the current-voltage product is at its maximum, called the maximum power point. The resistance of the load at this point is the optimum resistive load for the cell to drive. Given that

the current and voltage at the maximum power point are J_m and V_m respectively, the fill factor of the cell is then defined by **(1.12)**.

$$FF = \frac{J_m V_m}{J_{sc} V_{oc}} \tag{1.12}$$

The fill factor is an ideality ratio representing the ratio between the maximum power that would be expected if the cell could extrapolate from J_{sc} and V_{oc} to that achieved. It therefore incorporates the effect of the parasitic resistances without these resistances being explicitly measured. An example J-V curve with the important quantities shown is displayed in **Figure 1.15.** On such a plot, area represents power; the fill factor can be visualised by comparing the light and dark squares in the figure.

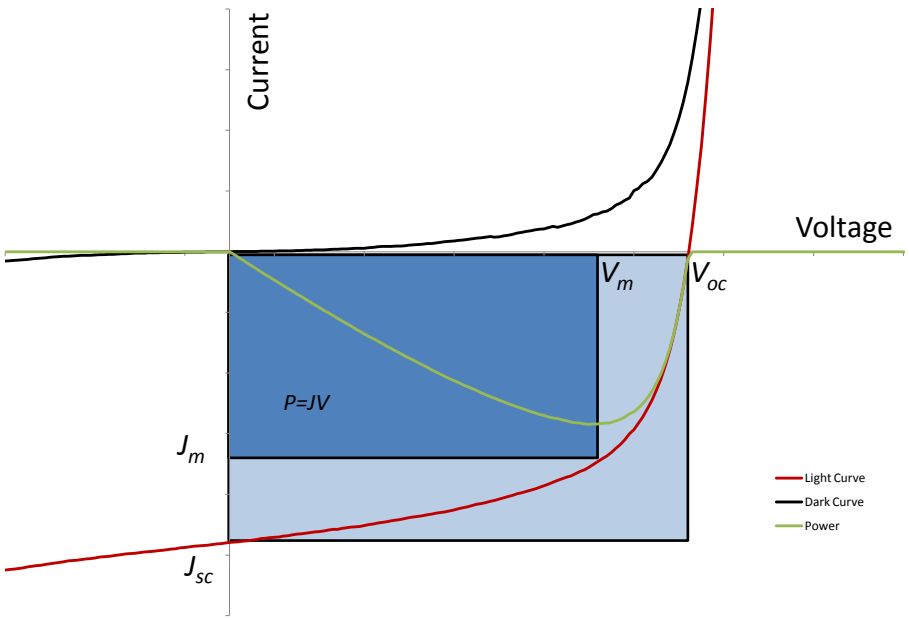

Figure 1.15. J-V curve with important parameters shown. The Fill Factor is the ratio of the two areas, defined by V_{oc} J_{sc} and $V_m J_m$.

Once the power that can be obtained from the solar cell is known, the power conversion efficiency (PCE) can be calculated. This is defined as the ratio of the power output, $J_m V_m$, to the power of the incident illumination, P_I, as in **(1.13)**.

$$PCE = \frac{J_m V_m}{P_I} = \frac{J_{sc} V_{oc} FF}{P_I} \tag{1.13}$$

1.5.7. SOLAR SPECTRUM

The efficiency of a cell will, in practice, depend on the spectrum of the light used, as **(1.6)** states explicitly. Since *Jsc* and *Voc* also depend on the incident light intensity, to compare solar cells a standard spectrum is used. The spectrum chosen is the global Air Mass 1.5 spectrum, or AM1.5G spectrum.

This spectrum is defined to be the same as the solar spectrum, but taking account of the absorption and attenuation by the earth's atmosphere. The extra-terrestrial spectra is also termed the 'air mass 0' (AM0) spectrum, indicating it does not include any atmospheric absorption. The formula for air mass is shown in **(1.14)**, which states that it is effectively the ratio in path length the light has to travel through the atmosphere compared to the case where the sun is directly overhead.[4] AM1 is thus the case where the sun is directly overhead, and AM1.5 corresponds to the sun being at an angle of 42°.

$$AM = \frac{Current\ sunlight\ path\ length\ through\ atmosphere}{Path\ length\ when\ sun\ directly\ overhead} \tag{1.14}$$

In space, the sun's spectrum is close to that of a 5760K black body radiator. A black body radiators' emission is calculated using **(1.15)**:[48]

$$L(\lambda) = \frac{2hc^2}{\lambda^5} \frac{1}{e^{\frac{hc}{\lambda k_B T}} - 1} \tag{1.15}$$

Blackbody spectra for various temperatures are plotted in **Figure 1.16**. At higher temperatures, the peak of the curve shifts to shorter wavelengths (or higher energies), as well as the total power emitted increasing as the fourth power of the temperature according to the Stefan-Boltzmann law.

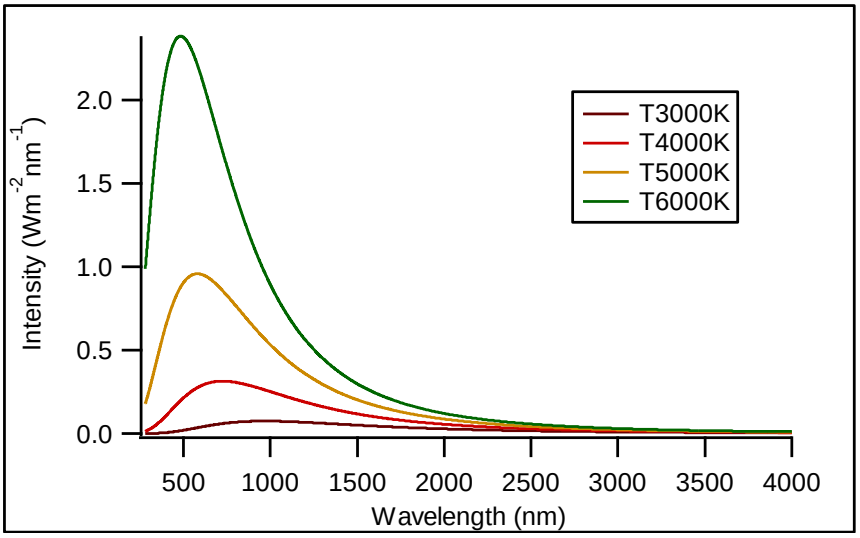

Figure 1.16. Ideal blackbody radiation emission spectra, for various temperatures of blackbody.

On the surface of the planet, the spectrum changes due to absorption in the atmosphere. Multiple bands are more strongly absorbed due to specific molecules in the atmosphere, such as water and carbon dioxide.[4] The AM1.5, AM0 and 5760K blackbody spectra are compared in **Figure 1.17**.

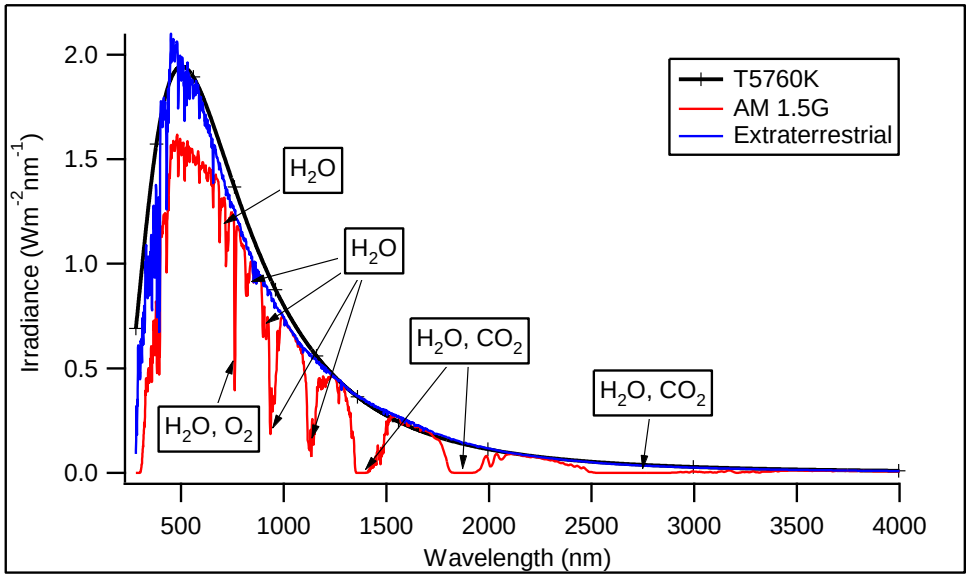

Figure 1.17. Comparison of the AM0 (extraterrestrial), AM1.5 and 5760K blackbody spectra. The 5760K blackbody spectrum is reduced in intensity for comparison. Data from the American Society for Testing and Materials (ASTM) G173 spectrum.[49] Obtained via the NREL website.[50]

Creating this spectrum in the lab requires specialised light sources, as discussed in **Section 2.6**. Deviations from this spectrum in measurement can lead to significant errors in efficiency calculations, particularly where the cell's absorption is localized, as is often the case for organic materials or tandem cells. This spectral mismatch can be accounted for by determining the spectral correction factor, defined in **(1.16)**.[51, 52]

$$F = \frac{\int_{\lambda_1}^{\lambda_2} Ir_{ref}(\lambda) S_R(\lambda) d\lambda}{\int_{\lambda_1}^{\lambda_2} Ir_{ref}(\lambda) S_T(\lambda) d\lambda} \times \frac{\int_{\lambda_1}^{\lambda_2} Ir_S(\lambda) S_T(\lambda) d\lambda}{\int_{\lambda_1}^{\lambda_2} Ir_S(\lambda) S_R(\lambda) d\lambda} \quad (1.16)$$

Ir_{ref} = Standard/Reference spectral irradiance (AM1.5G)

Ir_S = Spectral irradiance of the actual light source

S_R = Spectral response of reference diode

S_T = Spectral response of cell under test.

The resultant correction factor F can be used to correct the measured current of the cell to what would be expected in ideal conditions. If the actual light source was perfectly equivalent to AM1.5G, the equation would simplify to unity. The dependence on the reference diode lies in the calibration of the intensity for testing; the cell under test may be more sensitive to more / less light in regions of the spectrum where the reference diode is insensitive, depending on the materials used.

1.6. MATERIALS

This section will briefly introduce the materials used for devices in this thesis. Some discussion of their history, crystal structure, and electronic properties is presented, with a focus on the 'active' materials in the solar cell, the electron donors and electron acceptors.

1.6.1. ELECTRON DONORS

1.6.1.1. PHTHALOCYANINES: BACKGROUND

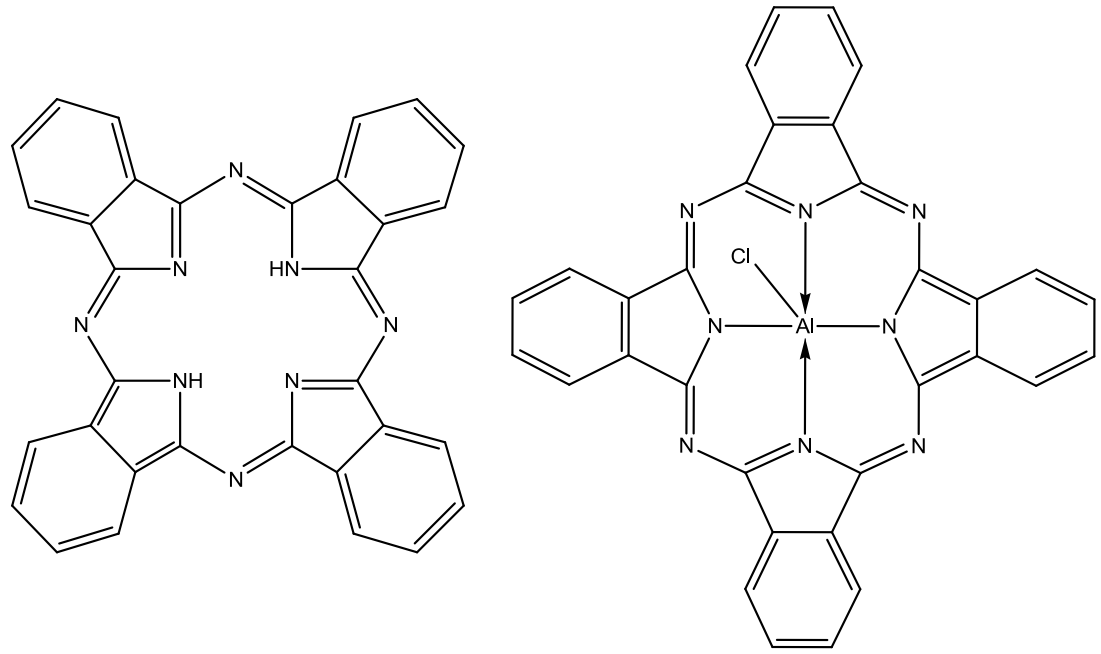

Figure 1.18. Metal-free phthalocyanine (H_2Pc,left), and Aluminium phthalocyanine chloride (ClAlPc, right).

All electron donors used in this work were Phthalocyanine (Pc) derivatives. Phthalocyanines of various composition have been used as dyes or inks since their accidental discovery in 1927.[53] The strong colours of these materials make them

interesting for OLED and OPV applications, although there is some interest in using them for more general organic electronics such as OFETs.[54]

Phthalocyanines are heteroaromatic compounds, porphyrin analogues, containing a large π system. The macrocycles contain a central ligand cavity that can either contain two hydrogen atoms (in the case of metal-free pthalocyanine, H_2Pc) or act as a metal chelating ligand, allowing the formation of many different metal phthalocyanine compounds, and making them extremely versatile. While phthalocyanines tend to be both chemically and thermally stable it is possible to modify the synthesis to add other groups on the outer ring to enhance various properties of the cell. For example, halogenation has been shown to shift the energy levels and absorption,[55] while other groups can be used to increase solubility.[56]

1.6.1.2. CRYSTAL STRUCTURE

The relatively weak π-π interactions between phthalocyanines and the flexibility of the molecules themselves leads to a number of possible crystal structures. Smaller central ions result in planar molecules, while large ones cause the molecule to shift into a pyramidal configuration to accommodate them; this affects the type of crystal formed by the molecule. Planar phthalocyanines, such as Copper (II) Phthalocyanine, have been shown to form at least 8 polymorphs;[57] in thin films, the α- or β-forms are usually observed. Growth on weakly interacting (i.e. non-templating) substrates depends on the substrate temperature; while the β-form is more favourable thermodynamically, if the substrate is below the α-β phase transition temperature, the α-form is grown instead. Growth on an elevated temperature substrate or annealing post-growth above the transition temperature can

cause the film to switch phases.[58] Both phases lead to molecular arrangements with a distinctive herringbone structure, as shown in **Figure 1.19**; the difference is the angle between the molecular plane and the stacking direction.[58]

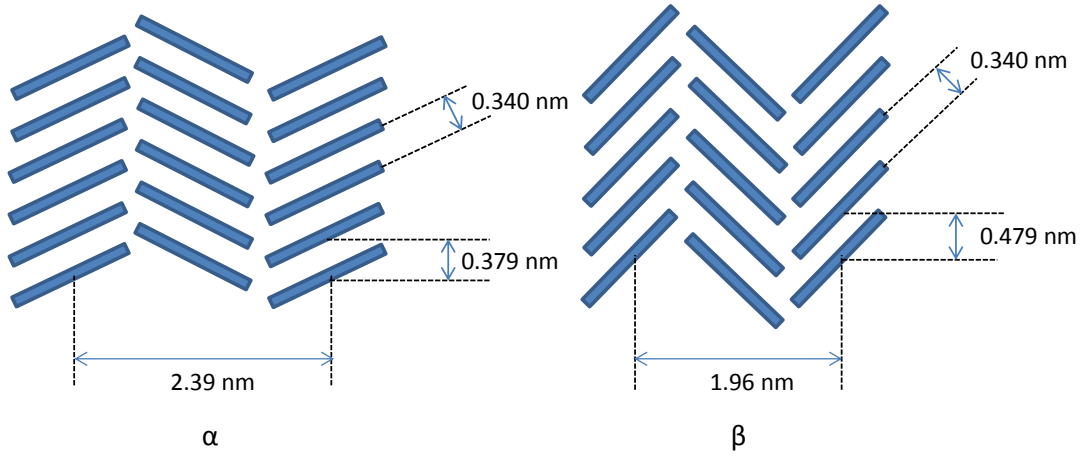

Figure 1.19. The 'herringbone' organisation of planar phthalocyanines such as CuPc, α- and β- forms shown. The primary difference is the angle between the molecular plane and the stacking direction.

This sort of packing results in anisotropic charge transport; this is easy to understand as the stronger intermolecular π – π interactions will aid charge transport in the stacking direction. On a weakly-interacting surface the stacking axis is generally parallel to the surface.

Aluminium phthalocyanine chloride (ClAlPc), as used in this work, differs from the planar CuPc in that the highly electronegative chlorine atom forces the molecule to adopt a more pyramidal configuration. Although the α- and β- phases of the crystal have been observed, both phases are polycrystalline rather than forming large crystallites like the planar phthalocyanines.[59] This reduces the charge mobility in ClAlPc films compared to CuPc. Material grown at elevated rather than room temperature has been observed to grow much larger crystallites, and should lead to a

better charge transport as a result.[59] Templating layers can also be useful in enhancing the crystallinity.[60]

1.6.1.3. ELECTRONIC PROPERTIES

The electronic structure of aluminium phthalocyanine chloride (ClAlPc, **Figure 1.18**) is not too dissimilar from that of CuPc, to be expected as the only changes are the metal cation and the introduction of a permanent dipole via the chlorine. ClAlPc thus has a HOMO level at 5.4 eV, and a LUMO level at 3.5-3.6 eV.[61] Charge mobility has been measured at $1x10^{-3}$ cm^2/Vs, though dependant on the deposition rate; presumably slower deposition rates lead to higher crystallinity.[62] ClAlPc demonstrates two primary areas of absorption, similarly to other aza-aromatic macrocyclic compounds and other phthalocyanines,[63, 64] a long wavelength Q-band absorption and Soret / B-band absorption in the UV-region. The Q-band absorption is dependent on the metal ion to some extent, and so shifts depending on the phthalocyanine; for ClAlPc, it lies between 600 and 850 nm. Q-band absorption is generally assigned to a π-π^* transition from the HOMO to the LUMO in phthalocyanines.[63] The absorption spectrum is displayed in **Figure 1.20**.

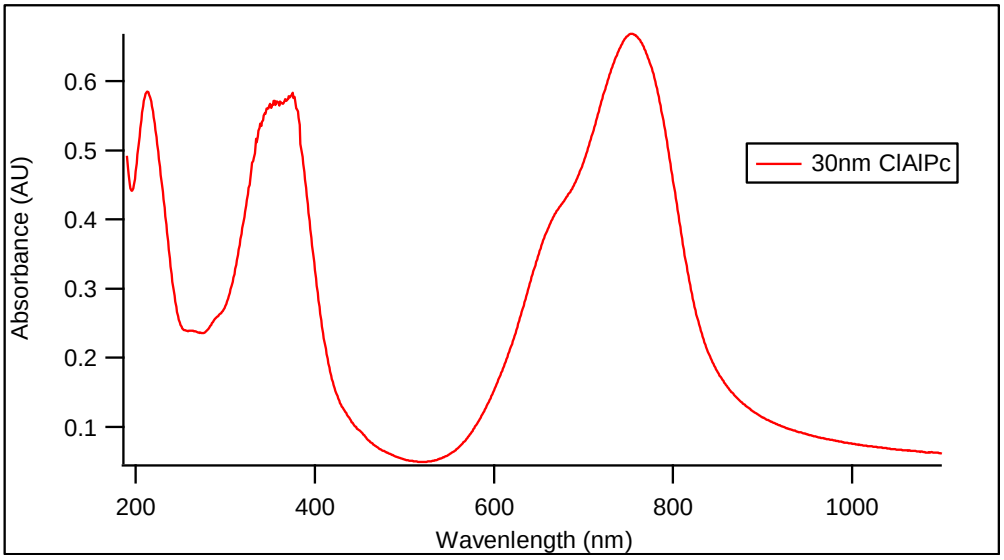

Figure 1.20. Absorption spectrum of a 30 nm ClAlPc thin film grown on a quartz substrate.

1.6.1.4. SUBPHTHALOCYANINE: BACKGROUND

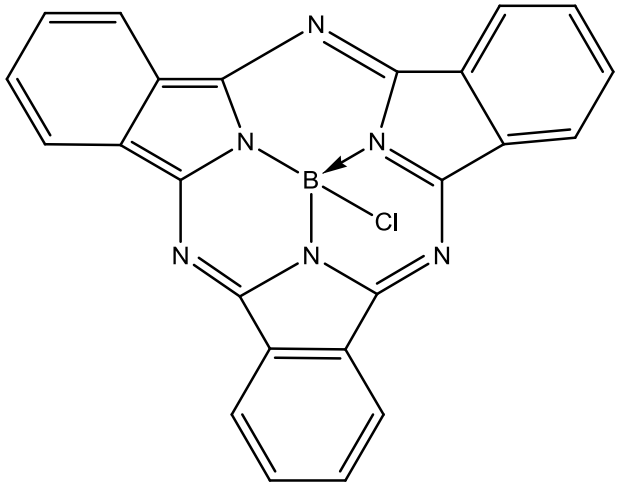

Figure 1.21. Boron Subphthalocyanine Chloride (SubPc).

Subpthalocyanines were first synthesized in 1972 by Meller et al. while attempting to create a boron phthalocyanine.[65] Only boron can be used as a metal ligand due to the much smaller space available in the macrocycle.

1.6.1.5. CRYSTAL STRUCTURE

The small size of the boron atom, plus the existence of the chlorine group causes the molecule to be non-planar.[66] While monolayer films have been observed by STM to form nanocrystals,[67] thicker films are generally considered to be amorphous.[61] This has implications for charge transport, as there is no strong coupling in any direction from $\pi - \pi^*$ interactions; charge mobility is correspondingly low in boron subphthalocyanine.

1.6.1.6. ELECTRONIC PROPERTIES

Boron subphthalocyanine chloride (SubPc, **Figure 1.21**) has its HOMO level at 5.6 eV, and its LUMO level at 3.6eV.[68] The lack of crystallinity limits charge transport, as shown by the lower hole mobility which is on the order of $1x10^{-5}$ cm^2/Vs.[69] Similar to ClAlPc, SubPc absorbs primarily in two regions, a Q-band in the visible between 450 and 625 nm, and a Soret (B) band in the UV, both assumed to correspond to π-π^* transitions on the C-N backbone.[70] The Q-band in subphthalocyanine is shifted to shorter wavelengths due to the smaller macrocycle. The absorbance is given in **Figure 1.22**.

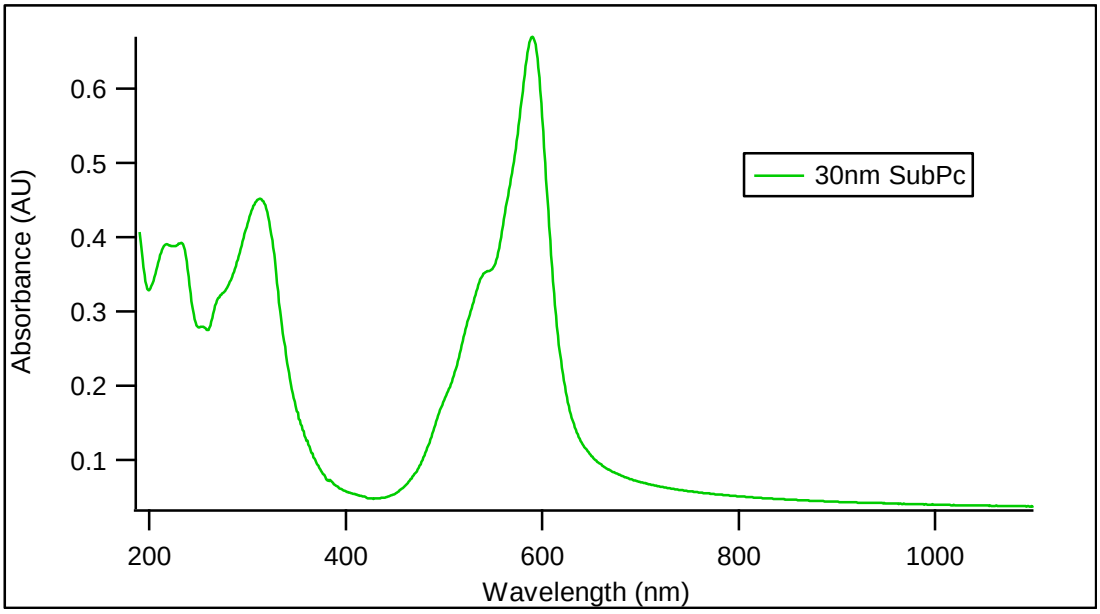

Figure 1.22. Absorption spectrum of a 30 nm SubPc thin film on a quartz substrate.

1.6.2. ELECTRON ACCEPTORS

1.6.2.1. FULLERENE: BACKGROUND

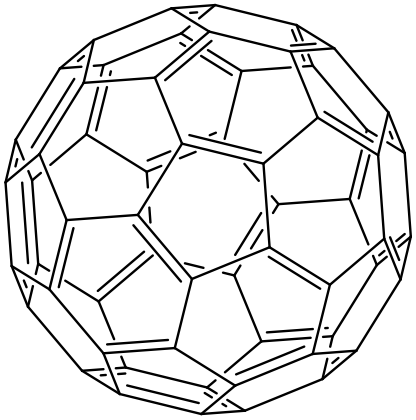

Figure 1.23. A Fullerene, or C_{60}, molecule.

The only electron acceptor used in this work was fullerene, C_{60}, which is an allotrope of carbon consisting of sixty carbon atoms, all linked together into a hollow sphere like a ball. The bonds form a distinctive pattern of hexagons and pentagons on the surface, as shown in **Figure 1.23**. The molecules were named after Buckminster Fuller due to the resemblance of the spheres with his futuristic architectures, and are sometimes referred to as 'buckyballs'.[71] The electronic properties of C_{60} have led to much interest in use for organic electronics, such as photovoltaics and OFETs.[72]

1.6.2.2. FULLERENE: CRYSTAL STRUCTURE

C_{60} molecules form an extended conjugated system due to sp-2 hybridisation, which also enables it to accept a number of electrons. This makes it a good electron acceptor, with a high mobility for an organic semiconductor. However, the curved surface of a C_{60} molecule strains the bonds of sp-2 hybridization, forcing them much

closer to the angles found in sp-3 hybridization. This also makes it more reactive with oxygen, potentially a problem in the presence of any trapped oxygen.

C_{60} forms a face-centred cubic lattice at room temperature, and the molecules are completely free to rotate rapidly.[73] Below 260K the molecules undergo a phase change and lose rotational freedom, and the lattice shifts to simple cubic, although this is not likely to occur for the usage of fullerene here. **Figure 1.24** shows C_{60} molecules in their face-centred cubic lattice.

Figure 1.24. C_{60} molecules in their fcc lattice configuration. Image by JW Jiang.[74]

1.6.2.3. FULLERENE: ELECTRONIC PROPERTIES

The high degree of symmetry and the extended π system present in C_{60} allow for good transport both across and between molecules.[73] The ability of a C_{60} molecule to accept between 6 and 12 electrons at once makes it a good acceptor material. The HOMO of C_{60} lies at 6.2 eV and the LUMO at 4.5 eV,[75] making it a useful match to the phthalocyanine donors. Absorption is dominated by electric dipole-allowed

transitions between bonding and antibonding molecular orbitals at short wavelengths (<400 nm), with weaker absorption at longer wavelengths up to 650 nm associated with electric dipole-forbidden transitions from the HOMO to the LUMO. An absorption spectrum for C_{60} is displayed in **Figure 1.25**.

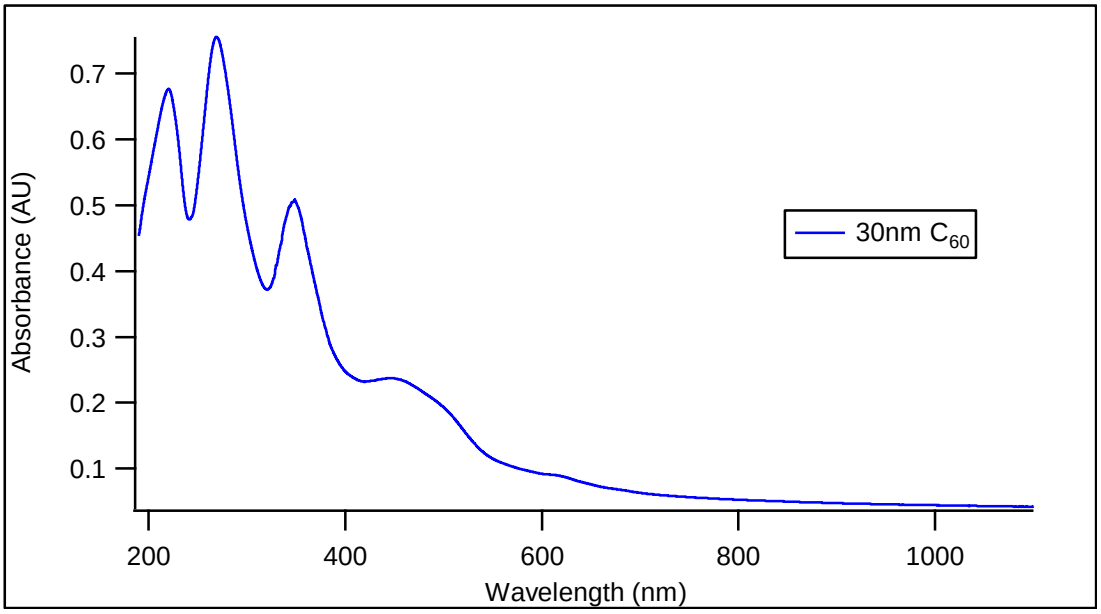

Figure 1.25. Absorption spectrum of a 30 nm C_{60} thin film on a quartz substrate.

1.6.3. INTERLAYERS

Several interlayers were utilized during this work, both for electrode modification and creating the recombination layer in tandem architectures; their various uses are critical to boosting the PCE and stability of the devices.

Molybdenum oxide (MoO_x), a transparent metal oxide, was used both to improve energy level alignment at the electrodes and also to improve the stability of the devices when grown on Indium-Tin Oxide (ITO) substrates (see section 1.6.4).[45] Workfunction values for this material vary depending on the measurement made, highlighting a need for further study; it is proposed that charge transport through

these layers occurs through gap states near the HOMO level of the donor, allowing for a better contact between donor and electrode.[76]

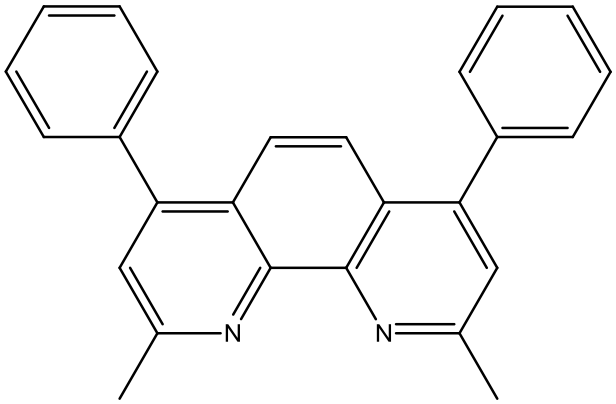

Figure 1.26. Bathocuproine (BCP).

Bathocuproine (BCP), or 2,9-Dimethyl-4,7-diphenyl-1,10-phenanthroline (**Figure 1.26**), was used as an exciton blocking and sacrificial layer.[77] The large band gap of 3.5 eV prevents excitons quenching at the metal interface and enhances efficiency, while the layer also protects the underlying active material from the bombardment of hot metal during electrode deposition. It is presumed that transport through this layer is via defect states induced by the bombardment of hot metal during electrode deposition. An electron mobility of 1.1×10^{-3} cm^2/Vs has been reported.[78]

Silver (Ag) was used to form metal nanoparticles in the recombination layer to act as recombination centres. This is explained in detail in **Chapter 3.** The workfunction of Ag varies between 4.14 eV up to 4.6 eV depending on the crystal face measured and precise nature of the measurement.[79, 80]

1.6.4. ELECTRODES

Since one electrode by necessity must have a very good transparency, indium-tin oxide (ITO) - coated glass with a sheet resistance of 15 Ω sq^{-1} was used as both substrate and bottom electrode. With its workfunction of -4.7 eV it is mainly used as a hole acceptor. ITO is relatively expensive as it must be sputtered onto the glass, and efforts are underway to find suitable replacements.[81]

The second electrode has no requirement to be transparent and it can actually be beneficial for this electrode to form a mirror surface to reflect incoming light back through the solar cell. Further consideration is given to this effect in **Section** 4 when discussing optical modelling. As a result, aluminium (Al) was chosen for its abundance, stability and low workfunction of -4.3 eV.[79]

2. THIN FILM GROWTH AND ANALYSIS

2.1. PURIFICATION OF MATERIALS

Purity of materials has been shown to affect device performance significantly,[82] so many of the materials used were first purified. All purification was undertaken by thermal gradient sublimation under vacuum at a base pressure of 10^{-6} mbar. Vacuum was provided by a turbo pump backed by a piston pump. A Carbolite tube furnace was used to provide controlled heating. Materials to be purified are placed in the bottom of a glass tube, placed inside a larger quartz tube connected to the vacuum system, and the tube placed halfway into the tube furnace, with the material at the centre of the furnace, as shown in **Figure 2.1**.

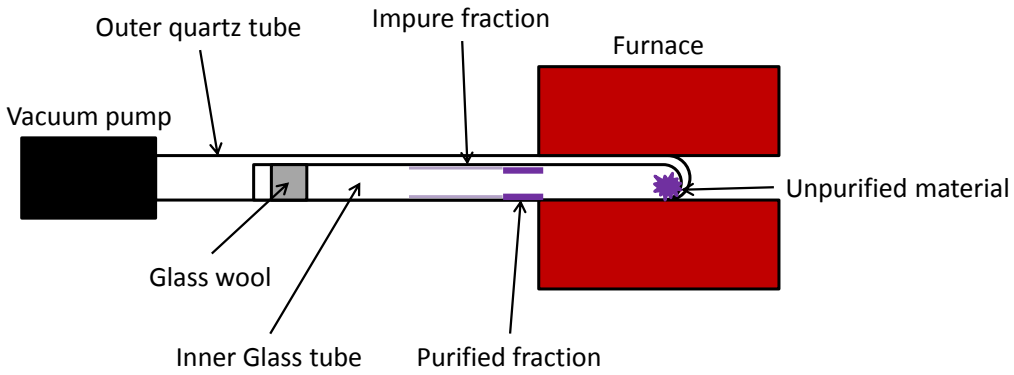

Figure 2.1. Schematic of material purification. The unpurified material is placed in the centre of the furnace, which is held just above the sublimation point of the material. The purified fraction is collected by removing and breaking the inner glass tube.

The system is then put under vacuum and heated at a rate ≤ 1 $Kmin^{-1}$, to a temperature determined by the material to be purified. After at least 10 hours at the purification temperature, which is ideally just above the temperature at which the material sublimates, the system is allowed to cool. The inner glass tube is then

removed and broken with a tube cutter near the band of purified material that forms where the tube left the furnace, and the band of material is scraped into a vial. Purified materials are removed and put under nitrogen atmosphere as quickly as possible.

2.2. SUBSTRATES

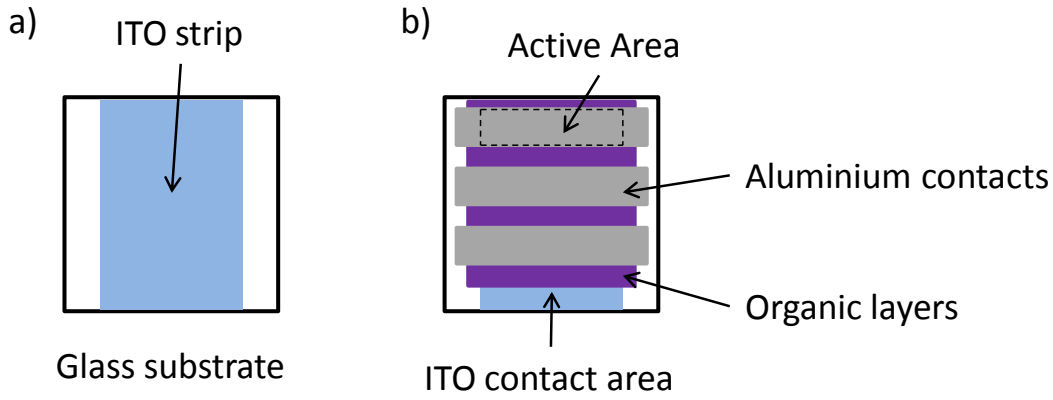

Figure 2.2. Diagram showing the substrates used for device work. Part a) shows the substrate with an ITO stripe, demonstrating the space left either side for use with the top contacts. Part b) shows the schematic of a complete device with organic layers and aluminium contacts.

All devices and samples were grown on indium-tin oxide coated glass (ITO) substrates. The substrates were obtained pre-cut to 12 mm x 12 mm from Thin-Film Devices. The substrates come with an 8 mm pre-patterned stripe of ITO down the centre of the substrate leaving 2 mm uncoated at each side to ease the application of electrodes without shorting the devices, **Figure 2.2a**. The 2 mm-width counter electrodes were grown across the organic layers perpendicular to the ITO stripe so contact could be made in the uncoated areas. This also gives a well-defined device area, as shown in **Figure 2.2b**. Before use all substrates were solvent and detergent

cleaned under sonication, utilising acetone, decon-90, distilled water and isopropanol, in the following process:

- Rinse in acetone
- Sonicate in acetone bath for 15 minutes.
- Quick acetone rinse
- Rinse in deionised (DI) water
- Sonicate in 30:70 decon:water mixture for 15 minutes
- Rinse in DI water
- Sonicate in DI water for 5 minutes
- Rinse in DI water
- Rinse in Isopropanol
- Sonicate in Isopropanol for 15 minutes
- Rinse in Isopropanol
- Dry with compressed nitrogen.
- UV-Ozone treatment for 30 mins.

U-V Ozone treatment involves placing the sample in an enclosed space with a U-V lamp, which generates ozone from the air inside. The ozone can then remove impurities from the surface of the substrate.

2.3.ORGANIC MOLECULAR BEAM DEPOSITION

For precise control over the thicknesses of the layers grown, organic molecular beam deposition (OMBD) was used to grow the devices. Many of the materials are also unsuitable in their current form for solution processing. OMBD relies on the sublimation or evaporation of the target material at moderate temperatures in vacuum, and cannot be used with materials that degrade before evaporation. The deposition utilizes the Knudsen effect, in which material evaporated under a vacuum

will travel in a straight line due to the long mean path length in the vacuum. For unconstrained material this leads to an equal flux in all directions, so the material is constrained by usage of a crucible, as in **Figure 2.3**.

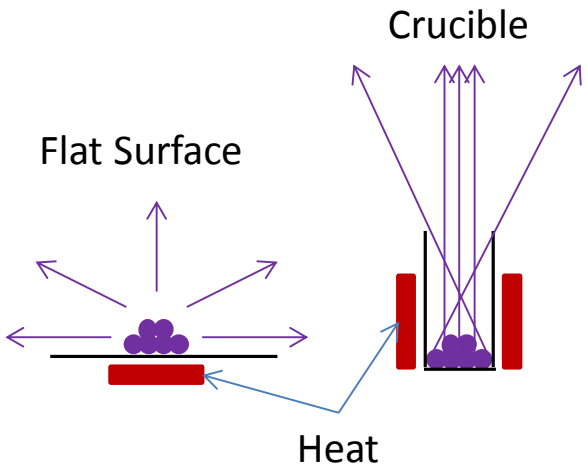

Figure 2.3. Comparison of flux from material evaporated on a surface to evaporation from a crucible. The crucible leads to a beam rather than an equal distribution, with the centre of the beam higher in flux than the edges.

This crucible is heated resistively and the temperature is controlled using a thermocouple with feedback software. This setup is termed a Knudsen cell, or K-cell. The walls of the crucible mean that the flux of material can only escape through the opening, forming it into a beam. The flux can then be controlled by adjusting the temperature of the cell.

The main growth system used in this project was a Kurt J. Lesker Spectros system. High vacuum is provided by a CryoTorr cryogenic pump capable of a base pressure of 10^{-8} mbar after initial roughing with a scroll pump. The system contains eight organic source cells (K-cells) and three metal source cells and supports both single and co-deposition of organics. Temperature control of the organic cells is provided

by a Mini-8 controller interfaced to a computer running custom Kurt J. Lesker Company (KJLC) software. Sigma Instruments SQS-242 is used to interface to QCMs placed strategically inside the chamber to report measured film thickness and growth rate (flux).

Figure 2.4. Spectros system, without glovebox, Picture courtesy of Kurt J Lesker company.

The substrate holder for this system can hold up to 36 substrates at once for homogenous deposition. It is possible to apply shadow masks to control exposure to any particular quarter of the substrate holder; this allows differing structures to be produced in a single growth. Masks can be changed without venting via an internal transfer arm, and are also used to grow separated aluminium contacts, allowing a single substrate to contain multiple pixels. The system is enclosed by a glove box such that devices can be grown and removed within a nitrogen atmosphere for

analysis or further processing. To keep samples under nitrogen for as long as possible, a sample holder that is airtight is used when taking samples out of the glovebox. This holds the substrate under a nitrogen atmosphere, but with a transparent quartz window to allow illumination, and with connections to the contacts on the device, allowing the device to be tested while still under nitrogen with no chance of degradation from oxygen or moisture.

2.4. METAL DEPOSITION

Deposition of metals in vacuum was also performed by thermal evaporation in a process similar to OMBD. Since metals evaporate at much higher temperatures than most organic materials, the heaters are designed differently. Crucibles are still heated resistively but instead of using a thermocouple to monitor temperature only the current flow is observed. The higher temperatures mean that energy loss from radiation is much more important as outlined by **(1.15)**, and so the temperature responds much more quickly to changes in current than in a K-cell. Adjustment of the current flow can still allow precise control over the flux from the crucible without knowledge of the temperature.

2.5. THICKNESS DETERMINATION

2.5.1. IN-SITU: QUARTZ CRYSTAL MICROBALANCE

Measuring the flux in OMBD requires a very precise method of measurement, as the flux can be low enough to deposit less than a monolayer of molecules per second. One of the few ways to measure fluxes this low is to use an oscillating quartz crystal, which is highly sensitive to mass changes at the surface. This was first recognised by Sauerbrey, who developed equation **(2.1)** relating frequency and mass change:[83]

$$\Delta m = \frac{\Delta f}{C_f} \tag{2.1}$$

In this equation Δm is the change in mass on the crystal, Δf the change in oscillation frequency of the crystal, and C_f the linear sensitivity factor of the crystal. However, if the frequency changes by more than 2% from the initial frequency of the crystal, the more complex equation **(2.2)** must be used.

$$\Delta m = \frac{N_q \rho_q}{\pi \left[\rho_q \mu_q / \rho_f \mu_f\right]^{1/2} f_L} \tan^{-1}\left(Z \tan\left[\pi \frac{(f_U - f_L)}{f_U}\right]\right) \tag{2.2}$$

Where N_q is the frequency constant, ρ_q is the density of the quartz crystal, μ_q is the shear modulus of the quartz, ρ_f is the density of the film material, μ_f is the shear modulus of the film material, f_L is the frequency of the loaded crystal, and f_U is the unloaded frequency. Quartz crystals are thus integrated into a holder and measurement apparatus to measure changes in mass, termed a Quartz Crystal Microbalance (QCM).

The change in mass can thus be determined by measuring the change in frequency of oscillation. To convert this to a thickness, the mass change can be divided by the density of the film, if known. As an added complication, the flux incident on the quartz crystal is likely to be different to the flux incident on the sample, as in **Figure 2.5**, which is the position of primary interest.

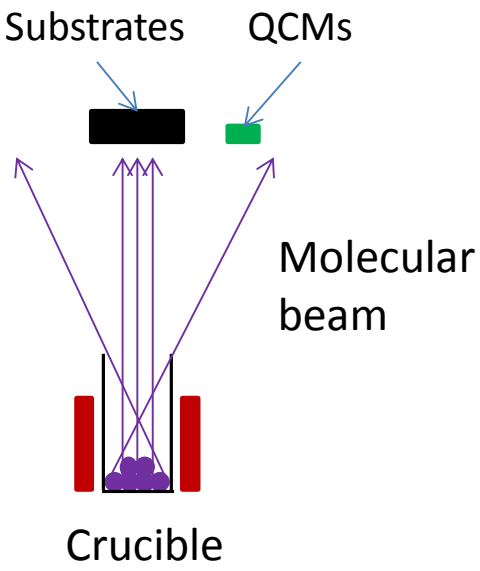

Figure 2.5. Illustration of the geometrical effect on QCM tooling factors. The molecular beam is not uniform from centre to edge, leading to differences in deposition on substrates and QCM.

To account for this, materials must be calibrated for a specific source location, QCM location, and material, using the assumption that the shape of the beam will not change significantly with time. This is done by growing a relatively thick film while taking note of the QCM reading, then measuring the film with other means, in this case an atomic force microscope (AFM).

2.5.2. EX-SITU: ATOMIC FORCE MICROSCOPY

AFM is a scanning probe technique utilizing the repulsive force of atoms bought close to each other. In its most basic form, the technique uses a cantilever with an ultra-sharp tip, which is brought into contact with the surface by piezoelectric elements. The reflection of a laser off the back of the cantilever is used to precisely measure the deflection, which allows a calculation of the force on the cantilever exerted by the surface via Hooke's law. By moving the cantilever to keep the force the same, and making a record of the movements made, a 3-D map of the surface can be made as the cantilever scans. The feedback loop required is built into the control software. A schematic of the complete setup for AFM is shown in **Figure 2.6**.

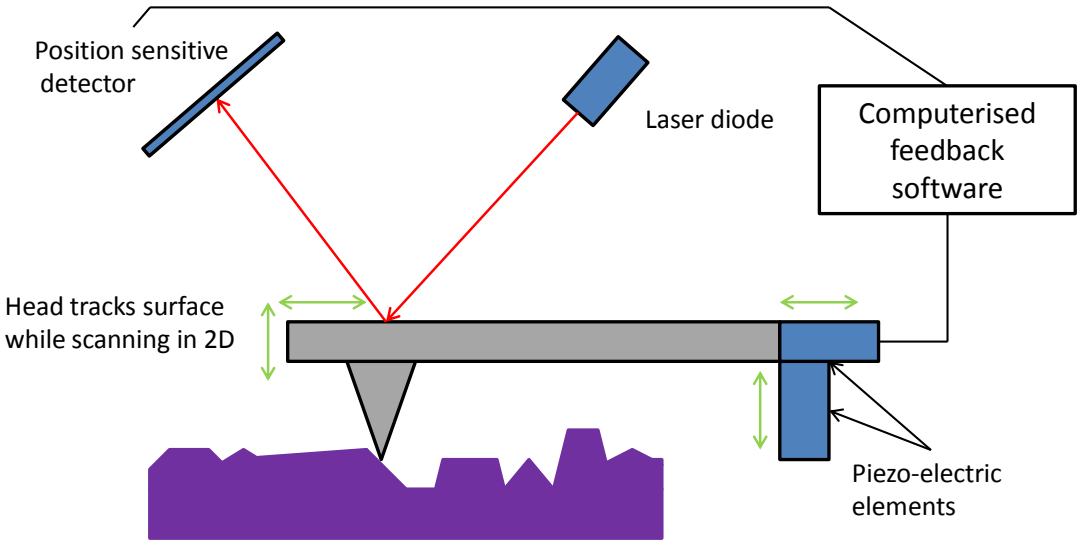

Figure 2.6. Schematic of the mode of operation of an AFM tip. Green arrows indicate movement, while the red indicates the laser.

This basic mode of operation, usually termed contact mode as the tip and surface are kept in contact, can lead to degradation of sample or tip easily. It can therefore be beneficial to instead use either non-contact or tapping mode. In non-contact mode, the tip is oscillated at a frequency just above its resonant frequency, with amplitude

of around 10 nm, and held slightly above the surface, between 1 and 10 nm. At this distance van der Waals forces are at their strongest, and act to decrease the resonance frequency of the cantilever. Changing the height of the cantilever to keep either the frequency or oscillation amplitude constant allows a similar measurement of the surface topography to normal contact mode, but with less stress on the tip or surface.

Tapping mode (also referred to as dynamic contact mode, or AC mode) is a modification of non-contact mode developed to avoid a problem with non-contact mode imaging in air. Most samples in this situation develop a liquid meniscus layer, which can cause a tip in non-contact mode to stick to the surface, destroying the delicate balance needed for accurate imaging.[84] Tapping mode involves oscillating the cantilever at a much greater amplitude typically around 100 – 200 nm, and maintaining a set oscillation amplitude while moving across the surface. Since the tip is only briefly 'in-contact' with the surface, much less damage occurs than in full contact mode, and there is no chance of the tip 'sticking' to the surface since the oscillations are so large.

This setup allows AFM to offer nanometer-scale resolution, determined primarily by the sharpness of the tip; some recent work has involved using a carbon nanotube as a probe tip to improve resolution.[85] A more in-depth consideration of AFM technique is available from Martin et. al. or Binnig et. al.[86] In this thesis, AFM was used primarily to determine layer thicknesses. To achieve this, the layer in question was partially removed from the surface using a sharp needle. As organics are much more easily removed than the underlying substrate, this allows the probe moving across the edge of the scratch to measure the height of the step up to the organic surface,

and thus the thickness of the layer. An example image and line profile is shown in **Figure 2.7**.

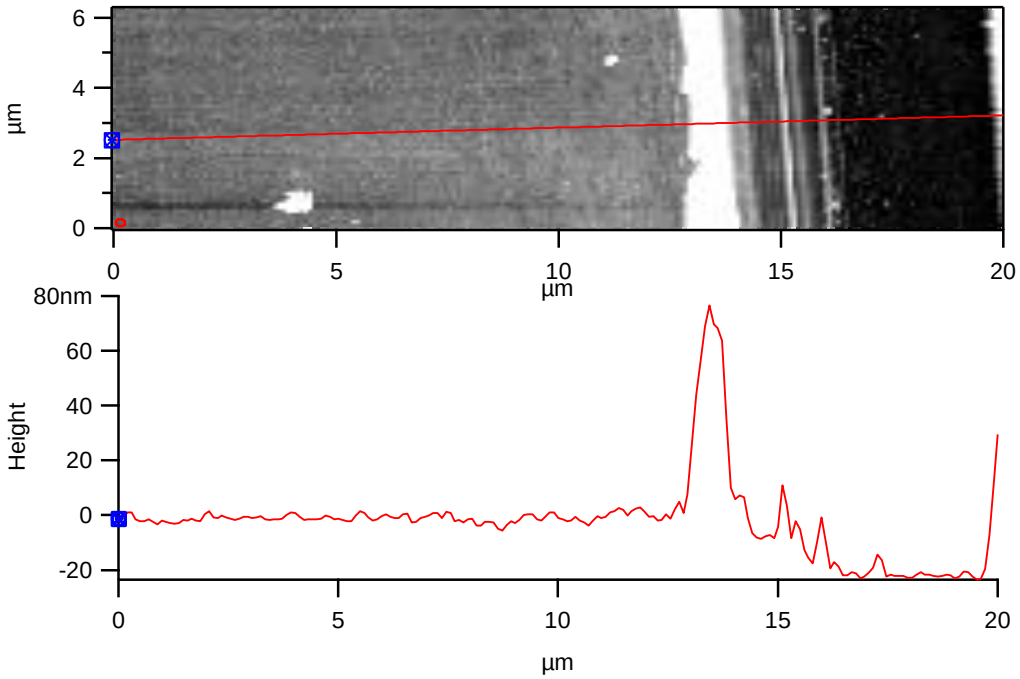

Figure 2.7. Image of a step edge with a 20 nm ClAlPc layer. The image has been flattened. ITO is much more difficult to scratch than the organic layers, so it is expected that the flat area to the right is the underlying ITO. This is supported by a phase change when scanning that area, not shown.

The points present in the image can then also be added to a histogram of heights, as below, to gain a numerical measure of the height difference between the two flat areas, as in **Figure 2.8**. The height difference (x-axis) between the best-populated bins in a properly flattened image can then be considered to be the thickness of the film, and can be measured by the software; in this case the software measured a difference of 18.8 nm between the two flat surfaces.

An Asylum Research MFP-3D-SA microscope with isolation table and hood was used to measure the thickness of organic layers by step-edge measurements. An image of the probe head is displayed in **Figure 2.9**.

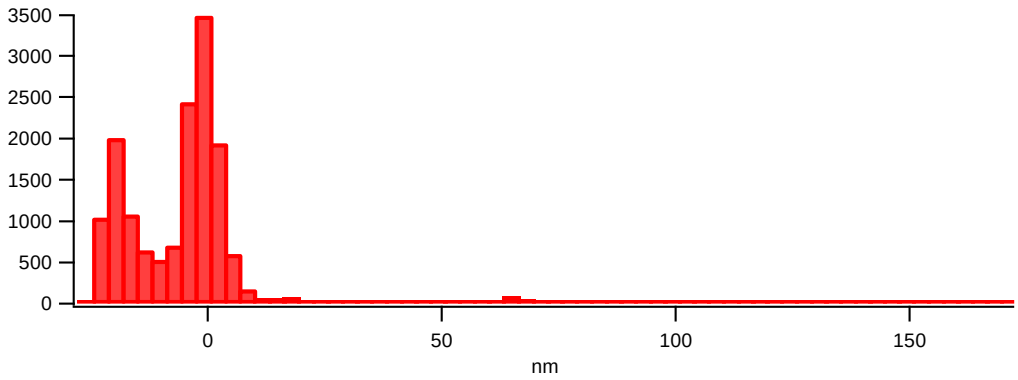

Figure 2.8. Histogram of point heights generated from the image in **Figure 2.7**. Height is the x-axis, while the number of points at that height is the y-axis. Bins need to be appropriately sized.

Figure 2.9. Asylum research MFP-3D-SA AFM base and head, image courtesy of Asylum Research.

To measure the power conversion efficiency of devices, a Newport – Oriel Solar Simulator (model 91191 – 1000) was utilized to provide illumination. This type of solar simulator is based around a Xenon arc lamp, and uses spectral filters to provide a reasonably good spectral match to sunlight at several times the intensity of the AM 1.5G standard. The normalised spectra are presented in **Figure 2.10** for comparison.

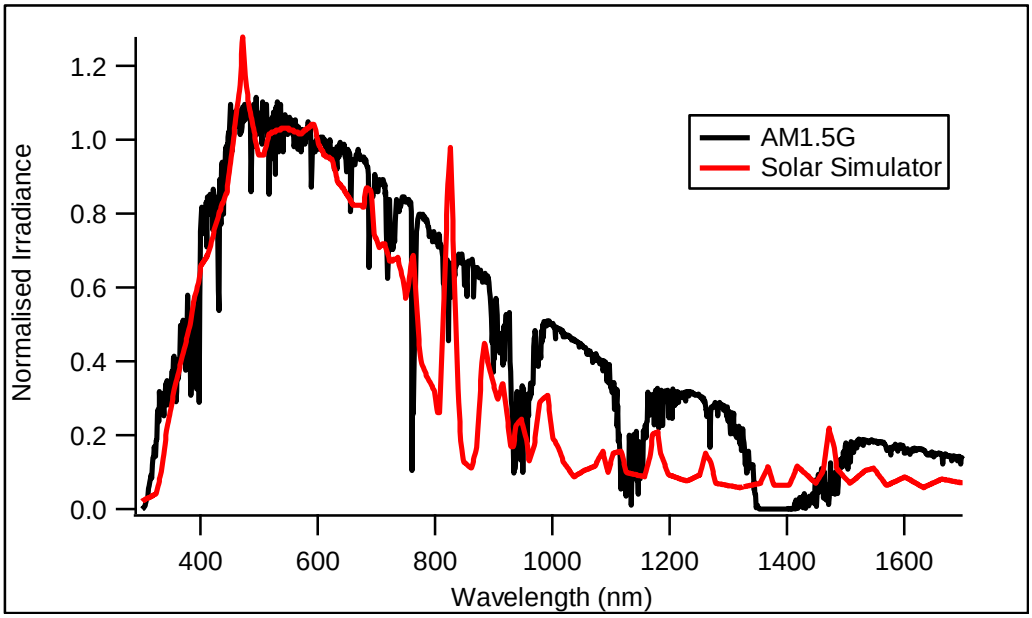

Figure 2.10. Comparison of the AM1.5G spectrum and the spectrum output from a Newport-Oriel solar simulator like the one used for this thesis. Both spectra are normalised to 600 nm for comparison. Data for the Newport simulator obtained from Newport's website.[87]

Additional neutral density external filters are then used to give a range of possible powers up to about 5 times the AM 1.5G standard, or '5 suns'. Light intensity is measured using a calibrated diode (PVM-482, PV Measurements, Inc) so it can be adjusted such that the power incident is equivalent to 1 sun (or whatever power is required).

The J-V measurements were performed using a Keithley 2400 sourcemeter attached to a computer via a National Instruments GPIB card, running a custom-made analysis program created by Dr. P. Sullivan. The software measures J-V curves and calculates the *FF*, V_{oc}, J_{sc}, and *PCE* when provided with a measurement of the illuminating intensity, as described in Section 1.5.6.

2.7. ELLIPSOMETRY

Two ellipsometers were used for this work, one at the University of Warwick (Nanofilm EP^3-SE) and a second at Imperial College, London (SOPRA GES 5). The experimental details of each are outlined below; the data was obtained via the specification of each instrument on the manufacturer's websites.[88] Ellipsometric theory is discussed in **Section 4.2.1**.

2.7.1. NANOFILM EP^3-SE

The ellipsometer was made by Nanofilm and is a model EP^3-SE spectroscopic Imaging Ellipsometer. This is a nulling ellipsometer in the PCSA configuration, which utilises a Xenon arc lamp as a light source, using 46 interference filters to provide light at specific wavelengths that cover the range 365-1000nm. It also includes a laser for calibration of the sample height. The goniometer for controlling the angle of incidence is controlled automatically, allowing fully automated variable angle spectroscopic ellipsometry (VASE) once the sample is aligned. The imaging uses a CCD camera and magnifying optics. The ellipsometer came with its own data analysis software, EP4, provided by Nanofilm. The software came with a small database of common materials, and allows the definition of multilayer stacks and dispersion functions for unknown materials.

2.7.2. SOPRA GES 5

The SOPRALAB (SOPRA) GES 5 is a rotating polarizer / fixed analyser PSA configuration ellipsometer, with a wide spectral range provided by a Xenon arc lamp and Monochromator, covering the range between 230 nm and 2 μm. It utilizes two different detectors, a photomultiplier for the UV/Visible spectrum from 230 nm to 880 nm and an InGaAs detector in the near infra-red up to 2 μm. The instrument is calibrated to measure the nonlinearity and polarization sensitivity of the different detectors and compensate for these effects during measurements. This ellipsometer likewise has its own analysis suite, similar in capability to the Nanofilm EP4 software, but this was not used extensively for this thesis, as it was only present at Imperial College.

3. SINGLE AND MULTIJUNCTION CELLS

3.1. DESIGN

The single cells in this work were grown in order to facilitate the growth of tandem cells and to correlate with the optical modelling and EQE measurements. The materials used in this section were introduced in section 1.6. The nature of the materials means that these cells are kept very thin and also have relatively narrow absorption bands, as explained in section 1.5. This makes it difficult to absorb the wide range of wavelengths available in sunlight with a single pair of materials. However, since extra vacuum deposited layers can simply be layered on top of each other, with little change to overall processing difficulty, multijunction cells can be very beneficial. Stacking materials that absorb at different wavelengths results in increased absorption while only minimally affecting the efficiency of either junction. Multijunction cells utilizing different materials for each junction are termed 'asymmetric'. The materials used here for the multijunction cells grown were chosen carefully so that their absorption overlapped as little as possible, as shown in **Figure 3.1.** This allows them to complement each other in a tandem cell, as displayed schematically by **Figure 3.2**. This approach should be beneficial when compared to 'symmetric' cells using the same material system in each sub-cell, which have been shown previously.[89]

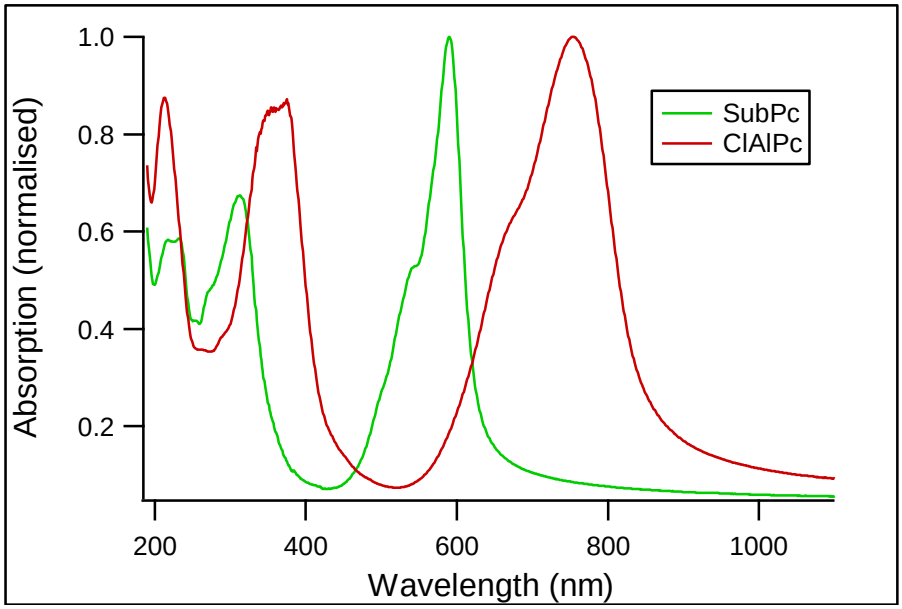

Figure 3.1. Electronic absorption (UV-vis) spectra of the active donor materials used here for single cells as introduced in Section 1.6.

Both material combinations (ClAlPc / C_{60} and SubPc /C_{60}) also benefit from a high obtainable open circuit voltage, Voc, when compared to many cells used in the literature.[90] This has been observed recently in the ClAlPc / C_{60} junction by Chauhan et al[91] and in the SubPc / C_{60} junction by Mutolo et al.[92] Some early work on tandem cells using these materials has also recently been demonstrated by Cheyns et al[27].

Creating a tandem cell is unfortunately not as straightforward as simply growing the extra layers from the single cells atop each other, as shown schematically in **Figure 3.2a**. The problem with this arrangement can be seen in the energy level diagram of **Figure 3.2b**. Combining two cells in this simplistic way creates the two intended D/A junctions, but also a reverse D/A junction between the acceptor of the first cell and the donor of the second. This heterojunction would oppose the other two, and lead to a reduction in efficiency due to the reverse photocurrent. To avoid this

problem, exciton blocking interlayers are used between the cells to prevent photocurrent generation.

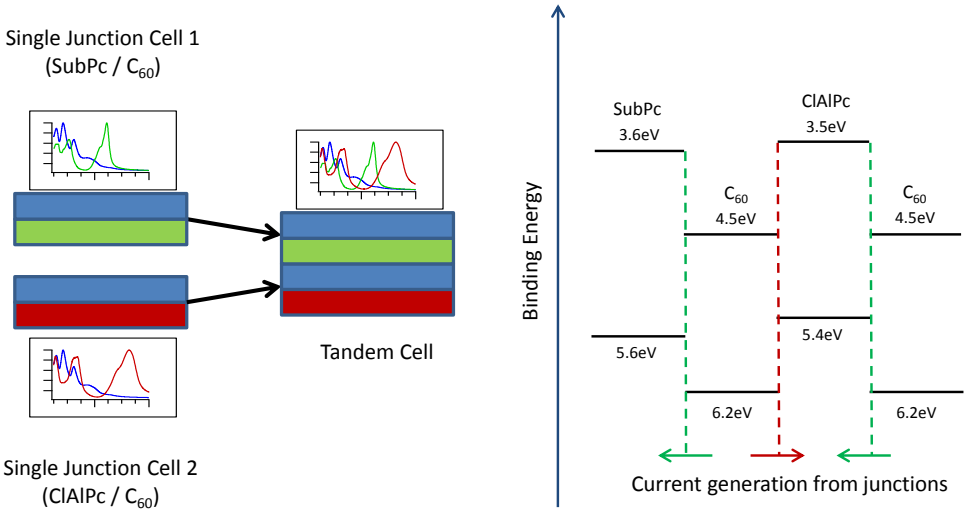

Figure 3.2. a) Schematic of creating a tandem cell, using the UV-VIS spectra of example materials to show the increase in absorption. b) Energy level diagram of the tandem cell. Arrows indicate current generation direction from each junction, with green currents being useful and red being counterproductive.

In addition, the lack of energy level alignment at the interface e between the two sub-cells will prevent charges from either side passing through. It is important that charge does not accumulate at the interface between sub-cells where it cannot be collected. Two extra steps are required to ensure this is achieved. Firstly, silver nanoparticles are added to serve as centres for recombination of electrons and holes from the front and back of the cell. The particles add extra energy states in-between the HOMO and LUMO at the interface that charges can transfer to in order to recombine easily, as displayed by **Figure 3.3**.

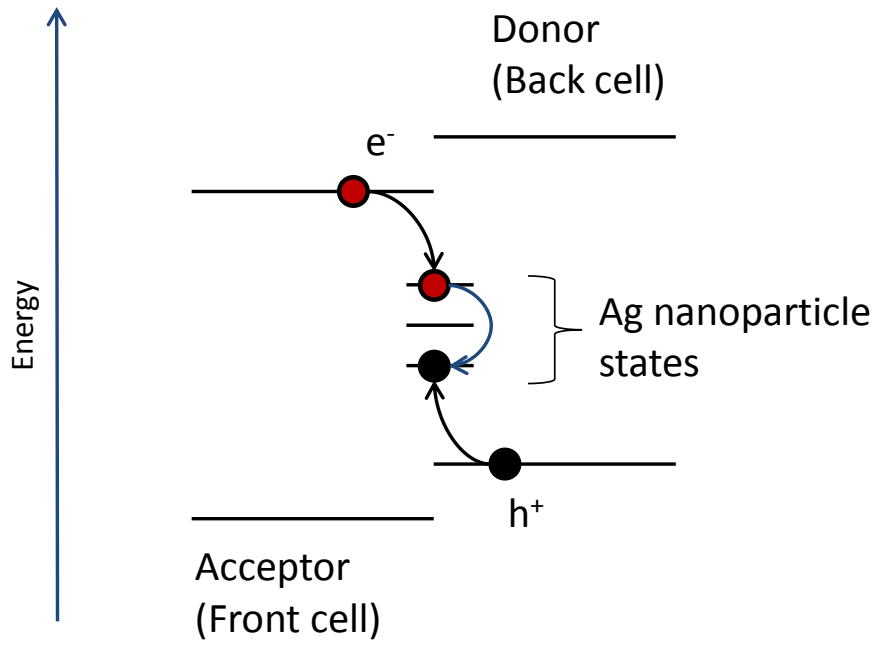

Figure 3.3. Recombination through the interface states of the Ag nanoparticles at the central interface between the two sub-cells.

Secondly, current from the front and back cells must be matched to ensure there is no accumulation of the dominant charge.[4] It is possible to remove this requirement, but it comes with a significant technical challenge. Providing two extra electrodes separated by an insulating layer between the two cells allows the cells to be electrically distinct, as shown in **Figure 3.4a**. These are called 'four-terminal' tandem cells, and are useful for sub-cells that have markedly different current generation or when it is desirable to be able to measure the sub-cells of the tandem cell individually.[93] Without the insulator, the back cell anode and front cell cathode are the same, making a three-terminal cell. While a three-terminal cell does not allow complete isolation of the sub-cells, it can be used to measure intermediate voltage in a series configuration and thus allows them to be measured individually. A parallel connection is possible by reversing one of the cells, demonstrated in **Figure 3.4b.**

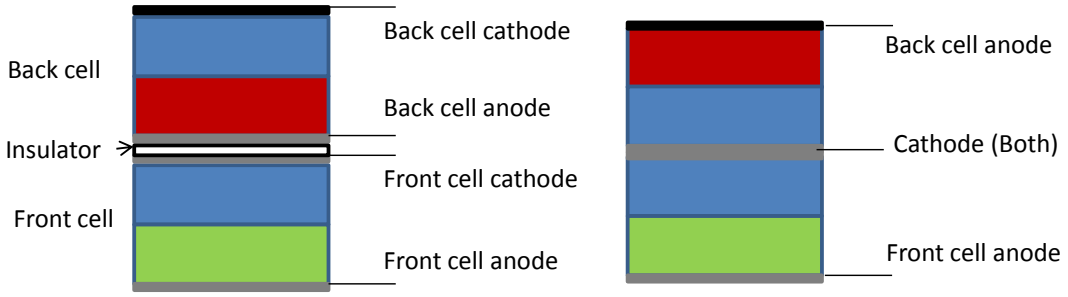

Figure 3.4. Schematic of a four terminal tandem cell. The cells are electrically isolated and so can be connected in series or parallel externally if required.

The ability to measure sub-cells individually is a valuable tool for tandem cells, but often difficult in organic cells due to material requirements. An ideal intermediate electrode would be completely transparent and highly conductive even in thin layers; however these two properties do not often overlap. Even for a completely transparent electrode the optical spacing effect (see **Chapter 4**) can cause the results with and without the intermediate electrode to be different, if the final aim is not to include the electrode in the design. One material commonly used as an electrode is titanium oxide (TiO_x), however, this cannot be deposited by evaporation and therefore it was not possible to use it for this work.

If an electrode between sub-cells is not possible, calculating current balancing in a multi-junction device is more complicated, requiring EQE measurements to get an idea of the current generation in the sub-cells of a tandem cell (see **Chapter 5**). Optical modelling can be very useful in predicting the changes in current generation with layer thickness due to the relatively strong effects of optical interference.

3.2. EXPERIMENTAL

The devices presented in this section were grown in a Kurt J. Lesker Spectros vacuum growth system, with film thickness monitored by a QCM calibrated by AFM measurements. SEM was performed on the Zeiss Supra 55VP-23-99 SEM in the Physics department at Warwick.

3.3. UNCERTAINTIES

Solar cells grown using these techniques demonstrate a strong dependence on material purity. Even when materials are purified using thermal gradient sublimation batch-to-batch variation can be noticeable. Batches may also degrade over time, leading to variability in solar cells made from the same batch at different times. Solar cells grown at the same time are much more consistent than cells grown separately. While the batch-to-batch purity changes make precise errors difficult to assign, an attempt is made here to do so in **Table 3.1**. This shows the percentage errors for a set of results both within and between batches that use the same nominal architecture:

Glass / ITO / 5 nm MoO_x / 10 nm SubPc / 40 nm C_{60} / 8 nm BCP / Al

These are still estimations, as the effect of batch purity varies between materials.

Table 3.1. Percentage errors, estimated via the standard deviation of sets of devices.

	Voc	Jsc	FF	PCE
Within batch	±1	±3	±7	±7
Across batches	±5	±6	±8	±14

In this thesis, where a trend was investigated the cells were generally grown in a single batch, utilising masking to grow the cells at the same time. This limits the dependency of the results on purity and minimizes the effect of the thickness measurement error.

3.4. RESULTS

The basis for the tandem cells in this work were the two single cell systems, SubPc / C_{60} and ClAlPc / C_{60}. Previous work on these systems has already demonstrated their potential for solar cells.[45, 94] Both single cells utilize MoO_x and BCP as interlayers, as discussed previously. This led to the following structures:

Glass / ITO / 5 nm MoO_x / 10 nm SubPc / 32.5 nm C_{60} / 8 nm BCP / Al

Glass / ITO / 5 nm MoO_x / 20 nm ClAlPc / 32.5 nm C_{60} / 8 nm BCP / Al

These architectures were optimised elsewhere, with representative cells shown in **Table 3.2**. The J-V curves for these cells can be seen in **Figure 3.5**.

Table 3.2. Statistics for some representative single cells, with MoO_x and BCP interlayers.

Donor	V_{oc} / V	J_{sc} / $mAcm^{-2}$	FF	Efficiency (%)
SubPc	1.06	3.60	0.59	2.26
ClAlPc	0.81	4.38	0.54	1.89

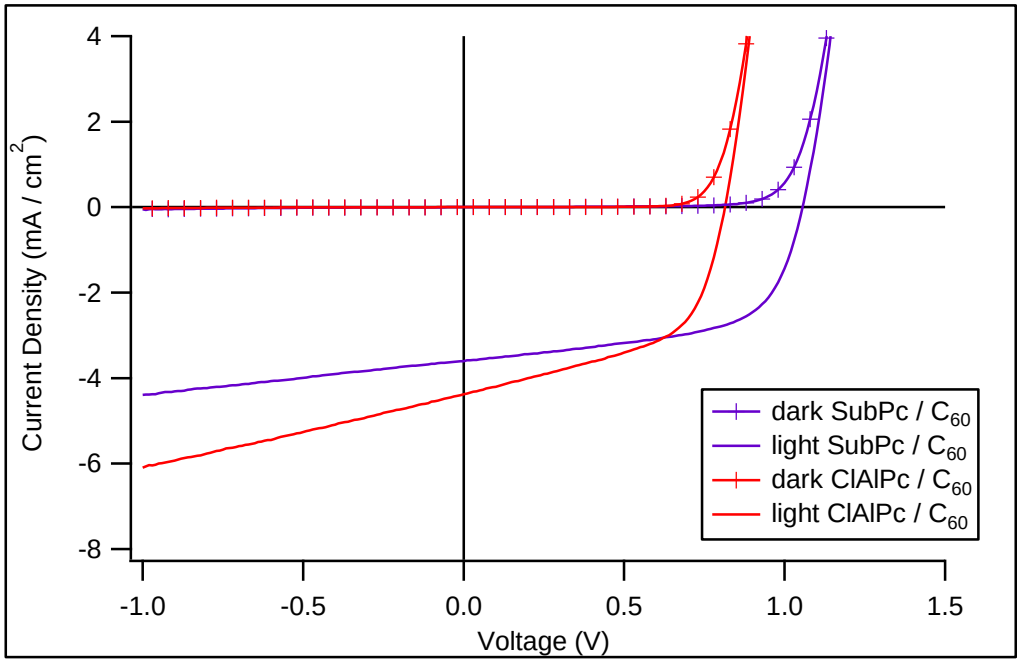

Figure 3.5. J-V curves for the two single cells described, showing both dark and with 100 mW / cm^2 illumination.

To combine these cells into a tandem cell, a recombination layer was required. As described in **Section 3.1**, silver nanoclusters were used to improve recombination in-between the sub-cells. The expected energy level diagram for such a cell at open circuit is shown below as **Figure 3.6**, with the Ag and interlayers suppressing any current generation at the recombination zone while also allowing the current from front and back cell to recombine efficiently to minimize voltage drop.

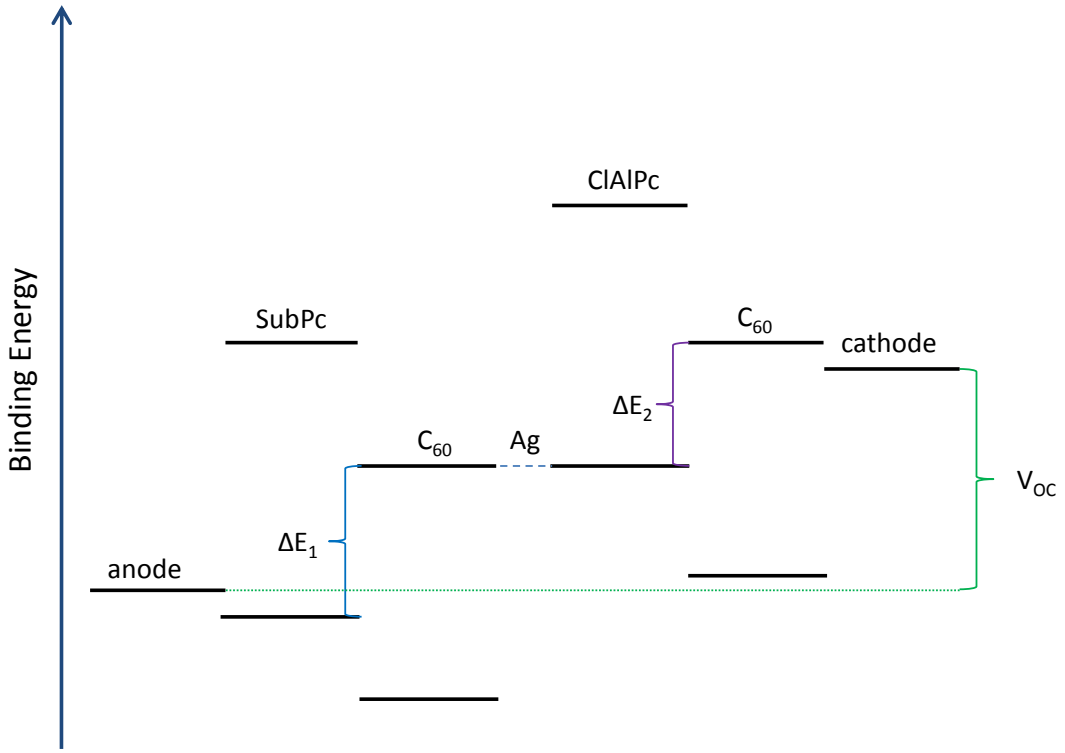

Figure 3.6. Simplified energy level diagram for a series tandem cell at open circuit. The open circuit voltage is expected to be close to the sum of the two sub-cells, minus any inefficiency at the recombination zone.

Growth of nanoclusters was achieved by simple thermal evaporation of very thin layers of silver. To prove this method formed nanoclusters rather than a discrete layer, SEM images of silver grown on ITO and ITO coated with BCP were taken. Two different thicknesses and two different rates at each thickness were tested to see if there was any observable deviation between them. The images of the 2 nm growth on ITO are compared in **Figure 3.7**. The left picture is the growth performed at a rate of 0.005 nms^{-1} and on the right growth at a rate of 0.015 nms^{-1}.

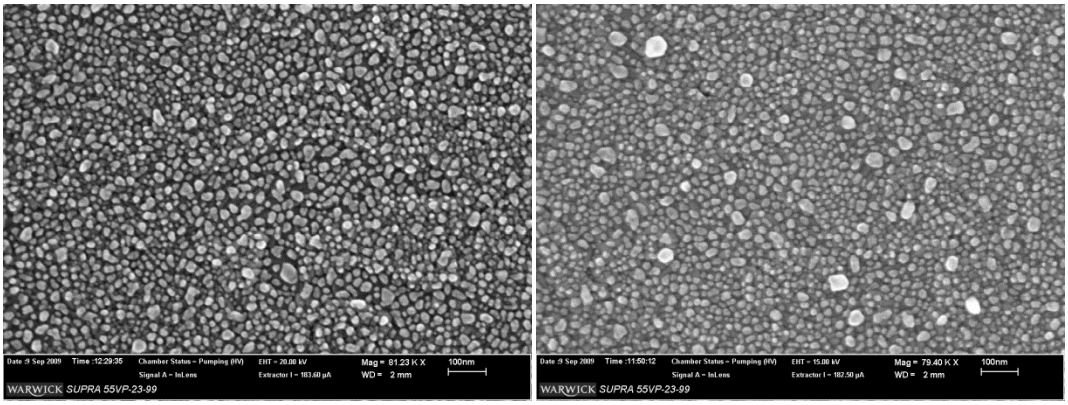

Figure 3.7. Left: 2 nm equivalent of Ag nanoparticles on ITO substrates, 0.005 nms^{-1} growth rate. Right: 0.015 nms^{-1} growth rate.

It can be observed that the growth rate has an impact on the average size of the particles, with more large particles in the faster growth for this thickness. Further samples were grown on $Si0_2$ at a thickness of 1 nm for comparison, shown in **Figure 3.8**.

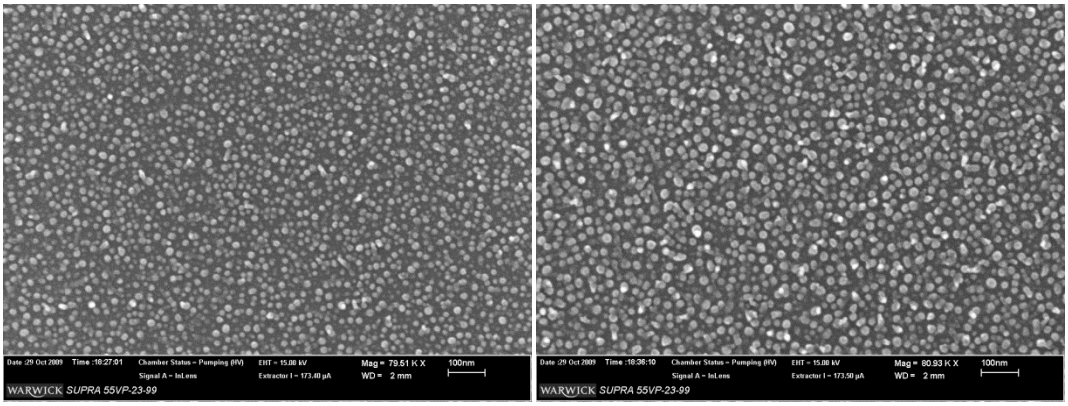

Figure 3.8. Left: 1nm equivalent of Ag nanoparticles on SiO_2 substrates, 0.005 nms^{-1} growth rate. Right: 0.015 nms^{-1} growth rate.

The thinner layers lead to a noticeable decrease in particle size and density compared to the thicker ones, particularly at the slower rate. The J-V curves of devices with and without 2 nm nanoclusters are shown in **Figure 3.9**. These early devices were

built based on single cell thicknesses for testing the recombination layer and had the following structure:

Glass / ITO / 5 nm MoO_x / 10 nm SubPc / 32.5 nm C_{60} / 8 nm BCP / y nm Ag / 5 nm MoO_x / 20 nm ClAlPc / 32.5 nm C_{60} / 8 nm BCP / Al

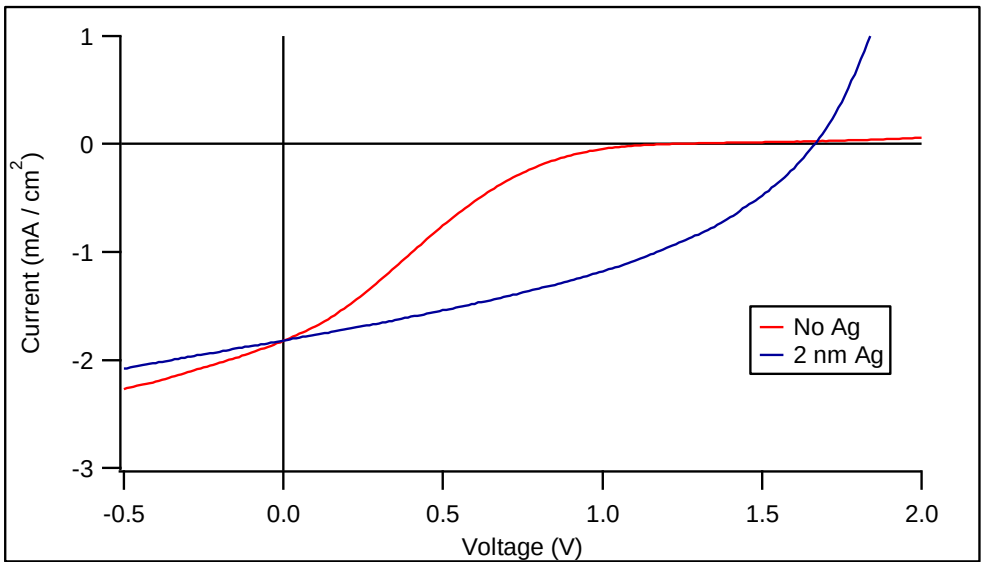

Figure 3.9. Comparison of the J-V curves of a set of tandem cells with and without silver.

The Ag layer thickness *y* was initially 2nm, with the later series testing a number of values between 0 and 2 nm. The Ag layers were grown at a rate of 0.005 nms^{-1} based on the SEM images, since larger particles would have a much higher chance of penetrating the interlayers and degrading device performance. From the figure, the cell without Ag can be observed not to pass significant current under forward bias, indicating a problem at the recombination zone, whereas the 2 nm Ag device displays a much more standard J-V curve. Adding Ag nanoclusters was thus shown to greatly improve the fill factor and obtainable open-circuit voltage, bringing it close to that expected by connecting the two sub-cells in series. The current

generation was still greatly impaired in the tandem architecture compared to the single cells; this can at least partly be attributed to the transmittance of the Ag layer, displayed in **Figure 3.10**. This measurement demonstrates that the transmittance starts to dip quickly with Ag layer thickness, potentially influencing current generation.

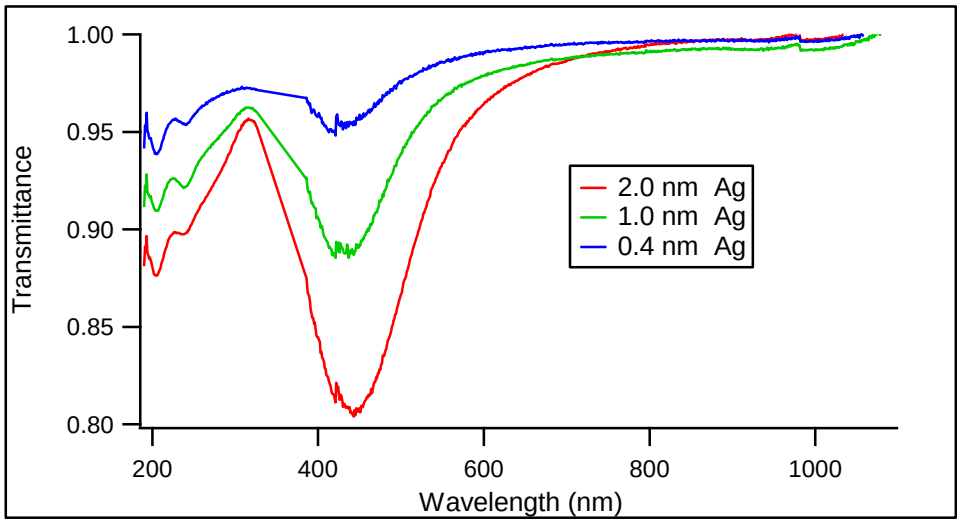

Figure 3.10. Transmittance of various Ag layers, of varying nominal thickness. The layers are formed of nanoparticles rather than being distinct layers; the thickness stated is the equivalent layer that would have the same mass as the nanoparticles.

As a result of the transmittance increase for thinner layers, a series of tandem cells with a range of Ag layer thicknesses were grown which showed a trend for improvement with thinner layers. These results are given in **Figure 3.11** and **Table 3.3**; they show that the short circuit current being equivalent at 2 nm of Ag is a coincidence, with the thinner Ag layers showing improved short circuit currents.

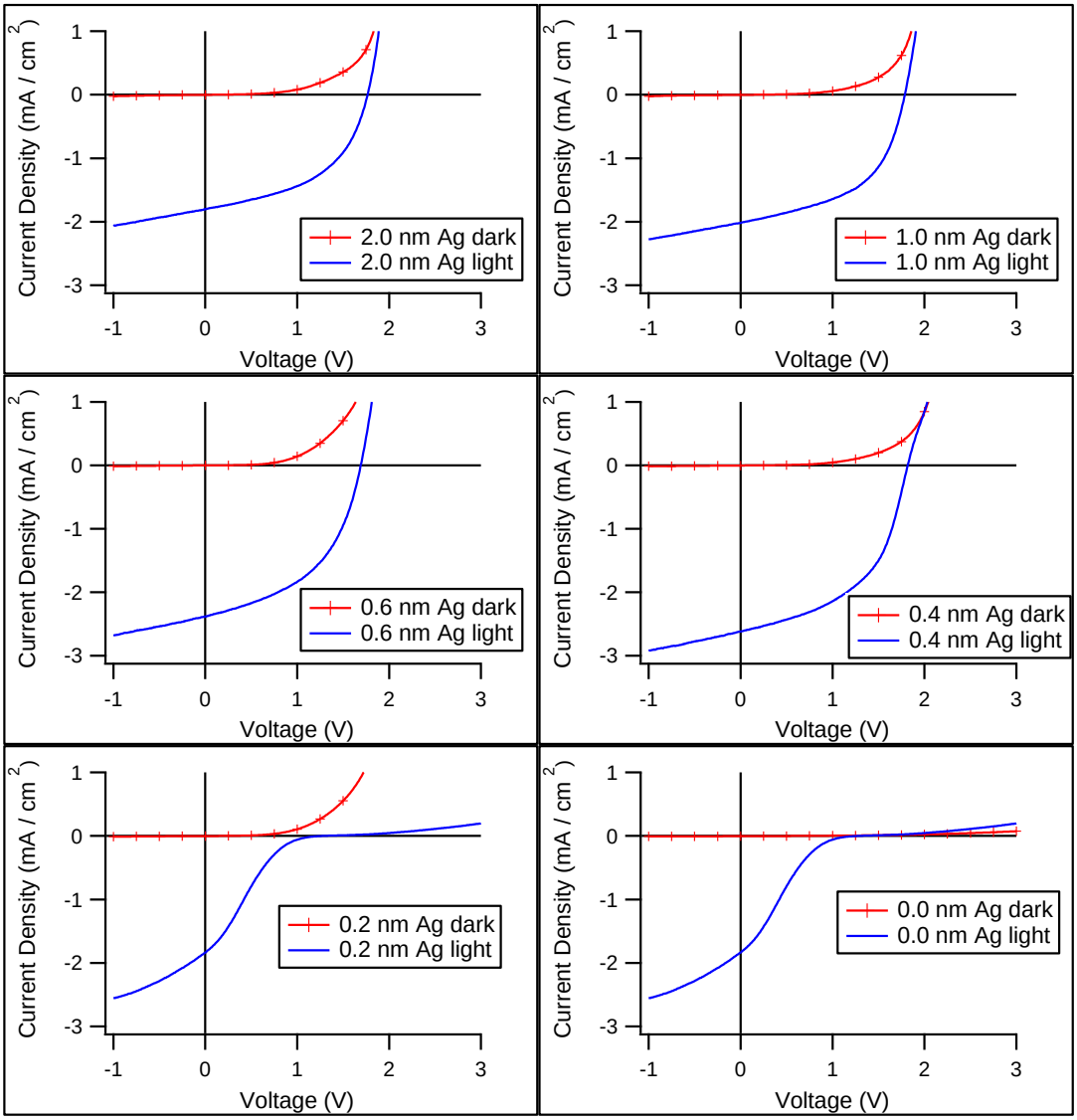

Figure 3.11. J-V curves of the series of cells investigating thickness, showing the changes in shape from adding Ag nanoparticles.

Table 3.3. Relation of cell properties with Ag layer thickness.

Ag thickness (y nm)	Voc (V)	Jsc($mAcm^{-2}$)	FF	PCE (%)
2.0	1.79	1.80	0.46	1.50
1.0	1.76	2.02	0.5	1.88
0.6	1.68	2.35	0.48	1.99
0.4	1.80	2.61	0.49	2.41
0.2	1.63	2.60	0.47	2.11
0.0	1.25	1.83	0.18	0.44

Utilizing thinner Ag layers led to an increase in performance such that the tandem cells exceeded the performance of the single cells, as demonstrated below. Further tests showed the optimum thickness for the Ag layer found to be in the region of 0.4 nm, at a rate of 0.03 nms^{-1}. Results of a test of this Ag layer are given in **Table 3.4**; these cells utilized a thinner front cell, as optical modelling predicted an improvement in current balancing by allowing more light to be absorbed in the back cell's C_{60} layer. Optical modelling is explained in **Chapter 4**; the architecture for these devices is given below:

Glass / ITO / 5 nm MoO_x / 20 nm ClAlPc / 17.5 nm C_{60} / 8 nm BCP / 0, 0.4 or 0.6 nm Ag / 5 nm MoO_x / 10 nm SubPc / 32.5 nm C_{60} / 8 nm BCP / Al

Table 3.4. Comparison of sub-cell and successive silver thickness measurements, thinner than 1nm, demonstrating the improvement as compared to the optimised single cells in **Table 3.2**.

Device	Voc (V)	Jsc ($mAcm^{-2}$)	FF	PCE (%)
SubPc / C_{60} sub-cell	0.93	3.90	0.56	2.12
ClAlPc / C_{60} sub-cell	0.75	2.74	0.53	1.11
0.6 nm Ag Tandem	1.80	3.06	0.47	2.68
0.4 nm Ag Tandem	1.80	3.39	0.47	2.99
0.0 nm Ag Tandem	1.34	2.89	0.27	1.10

The J-V curves for the 0.4 nm silver tandem device and the sub-cells are directly compared in **Figure 3.12**. The increase in current generation from the device with no Ag layer and the improved fill factor can be observed. With this recombination layer, optimizing the tandem cells became more focused on improving the current output through current balancing.

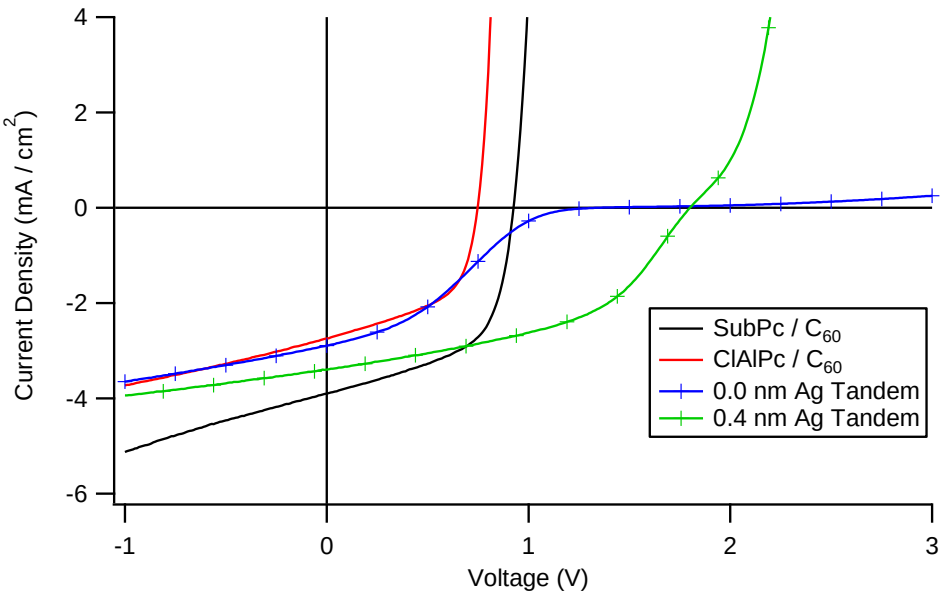

Figure 3.12. J-V curves of a 0.4 nm Ag recombination layer tandem device and its sub-cells for comparison.

The tandem device can be seen to have approximately the sum of the individual open-circuit voltages, with a current output in-between the two sub-cells. This is expected due to current balancing, and there are two possible explanations, though it is likely some element of each contributes. Firstly, the sub-cells as measured are not representative of the current generation in a tandem architecture as light will be absorbed due to the presence of the second sub-cell, meaning the current estimates from single cells are not accurate. This is considered further in **Chapter 4**. Secondly, the underperforming sub-cell can be compensated for by the over-performing sub-cell, as the over-performing cell can put the under-performing cell under a voltage bias to force more current to flow through it, even though the outside contacts are shorted together. This can be explained easily by considering short circuit conditions, where the contacts are kept at the same potential, with a situation where only one sub-cell is active. This is shown schematically in **Figure 3.13**; if only one cell is active, it will generate a photovoltage at the interface between the cells because the charges cannot pass through the second cell.

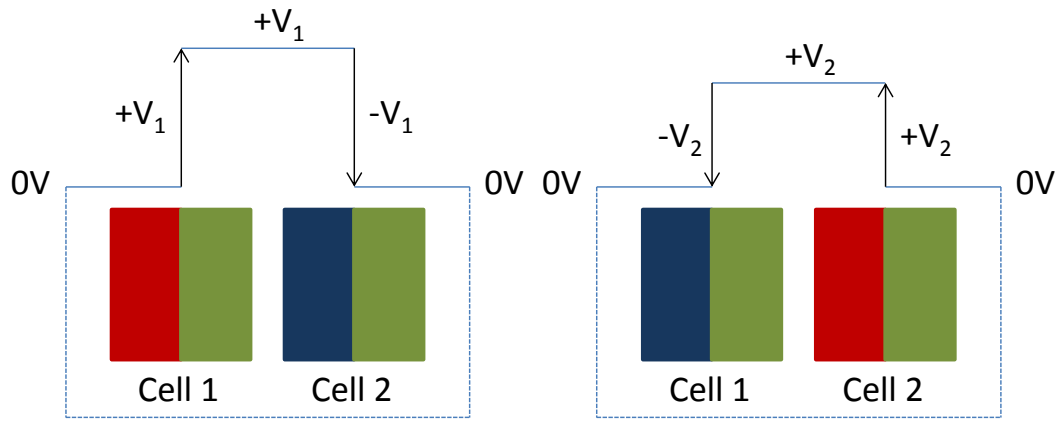

Figure 3.13. Schematic of the voltage situation in a tandem cell when only one cell (red donor) is active. The active cell will apply a bias to the other cell equal and opposite to the photovoltage it can generate across itself.

This photovoltage can then be treated as an applied bias on the second cell, which will negatively bias the cell and drive current through it. Once this process reaches a steady state, the current through both cells will necessarily be equal, with the voltage generated across the active one dropped across the second. This can be extended to any situation where the current generation in the two sub-cells is unequal, as this will lead to a charge (and thus voltage) build-up at the interface. **Figure 3.14** demonstrates predicting the short circuit current (external bias V = 0) using the assumption that the single cell J-V curves accurately represent the tandem cell sub-cells. This estimate compares relatively well with the actual measured J_{sc}, even though no effort has been made to correct for the different optical electrical field inside the tandem cell as compared to the single cells. If the J-V curves of each sub-cell under the existing operating conditions are known, it is possible to construct the J-V curve of the complete device using the condition that the currents must be equal.

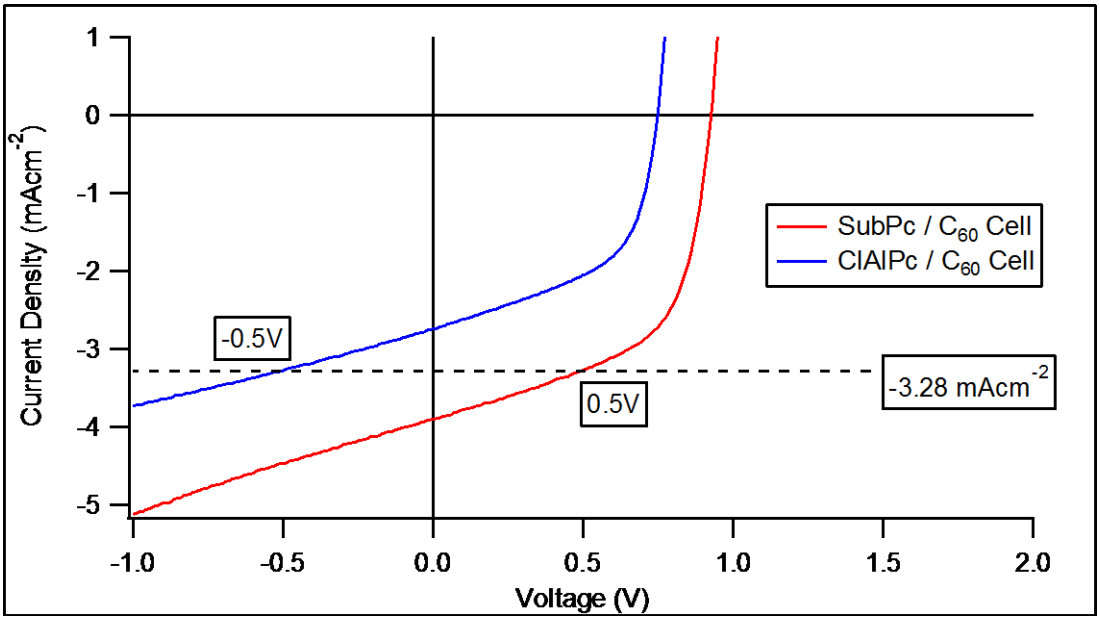

Figure 3.14. Using single cell measurements (representing the sub-cells in the tandem device) to predict J_{sc} of the full device.

It is possible to correct for the differing illumination intensity in a tandem device by utilising optical modelling. In order to improve understanding of current balancing in the tandem cells, optical modelling and external quantum efficiency measurements were utilized, and these form the basis of the remainder of this thesis.

3.5. SUMMARY

This chapter introduced the tandem cell design pursued in this thesis with particular results from an optimisation of the Ag layer in the recombination zone. Results were presented which demonstrated the need for such an Ag layer, as tandem cells constructed from two single cells without this layer had lower-than-expected open circuit voltage, short-circuit current and fill factor. All Ag layers tested (0.4-2 nm) showed an improvement over no layer, with the optimised layer showing further improvements; this layer was determined to be 0.4 nm Ag, grown at a rate of 0.005 nms^{-1}. Tandem devices utilising an optimised recombination layer had significant performance advantages as compared to the single cells with either material combination, demonstrating the benefits of combining these materials into a multijunction architecture.

4. OPTICAL MODELLING

4.1. THE NEED FOR OPTICAL MODELLING

For any solar cell, but especially for organic and tandem solar cells, it is desirable to know where in the active layer light is being absorbed. For excitonic single heterojunction cells, knowing where light is absorbed allows knowledge of the exciton distribution in the device and can thus influence optimum layer thicknesses, as described in **Section 1.5.2.** For series tandem cells, which require current balancing in addition to the single cell requirements (as described in **Chapter** 3), optical modelling becomes more necessary. The location of light absorption can have a much greater impact on the performance of the whole tandem cell than in the single-cell case; if all the light is absorbed in the first cell, optimizing the second cell will never lead to an improvement in efficiency.[23] This is the reason that inorganic tandem cells always have the highest band gap semiconductor at the front of the cell, as it will not absorb light of lower energies, which can then be absorbed in the successive sub-cells. The comparable process in organic tandem cells is to use molecules that absorb in different regions of the spectrum.

For macroscopic objects, light transmission through a layer can often be described by the Beer-Lambert Law. It was actually discovered around 1729 by Pierre Bouguer, and extended by August Beer in 1852 to include the concentration of solutions.[95] The law effectively states that, were the layer split into equal thickness slabs, each slab of material would absorb the same proportion of the incoming light. This allows calculation of the transmission of a layer when the absorbed proportion is known, as represented by the absorption coefficient α in **(4.1)**.

$$T = \frac{I}{I_0} = e^{-\alpha l} \tag{4.1}$$

In this equation, T is the transmittance, while I_0 is the incident radiation intensity. I is the radiation intensity that successfully passes through the slab of material, α is the absorption coefficient and l is the thickness of the slab. For the purpose of solar cells, it then becomes useful to define the absorptance A as the fraction of the incoming light that is absorbed in a layer, as in **(4.2)**. It should be noted this is a different quantity to the more common absorbance; absorbance is useful because it does not change with layer thickness, while absorptance is specific to a layer, like transmittance. If the incident illumination is known, multiplying the photon count by the absorptance will then reveal how many photons have been absorbed in a layer.

$$A = 1 - T - R \tag{4.2}$$

However, the Beer-Lambert law has a number of limitations;[95, 96] one of these is that the absorption coefficient can only be used to calculate absorption in the absence of a significant contribution from interference. Interference is a phenomenon that occurs when two waves superimpose, and leads to a resultant wave of greater or lower amplitude. Light passing through an interface between any two materials has a chance of being reflected rather than transmitted, the chance depending on the relevant dielectric value in each material, which is wavelength-dependant. Close to such a reflection, it is possible for the reflected light to interfere with the incident light; in thick films this effect is close to negligible due to the light becoming

incoherent.[97] However, for thin films, this effect can become significant, particularly near highly reflective interfaces such as metal-organic interfaces, which are used for the back contact of most organic solar cells. In this situation it is not appropriate to use the Beer-Lambert law to calculate absorption.

Instead, to obtain an accurate picture of light absorption, it is necessary to calculate the optical electromagnetic fields throughout a device. This is done utilizing Maxwell's equations and the relevant material equations. Once the electromagnetic field solutions have been calculated, the Poynting vector is used to calculate absorptance at all points of interest in the device. This calculation then includes the effect of interference and reflection at each interface between layers, which is a necessity for accurate calculations in thin film stratified structures.

4.2. ELECTROMAGNETIC THEORY FOR LAYERED MEDIA

Similar derivations to that presented here can be found easily in the literature and in textbooks.[97, 98] To model light propagation in media, the macroscopic Maxwell's equations, given as **(4.3)** to **(4.6)**, combined with the material equations, given as **(4.7)** to **(4.9)**, must be solved.

$$\vec{\nabla} \times \vec{\mathbf{H}} = \vec{\mathbf{j}} + \frac{\partial \vec{\tilde{\mathbf{D}}}}{\partial t} \tag{4.3}$$

$$\vec{\nabla} \times \vec{\mathbf{E}} = -\frac{\partial \vec{\mathbf{B}}}{\partial t} \tag{4.4}$$

$$\vec{\nabla}.\vec{\mathbf{B}} = 0 \tag{4.5}$$

$$\vec{\nabla}.\vec{\tilde{\mathbf{D}}} = \rho \tag{4.6}$$

$$\vec{\mathbf{B}} = \mu_r \mu_0 \vec{\mathbf{H}} \tag{4.7}$$

$$\vec{\tilde{\mathbf{D}}} = \varepsilon_r \varepsilon_0 \vec{\mathbf{E}} \tag{4.8}$$

$$\vec{\mathbf{j}} = \sigma \mathbf{E} \tag{4.9}$$

In these equations, $\vec{\mathbf{E}}$ is the electric field, $\vec{\mathbf{B}}$ is the magnetic field, $\vec{\tilde{\mathbf{D}}}$ is the electric displacement field (or electric field in a medium), $\vec{\mathbf{H}}$ is the magnetizing field (or magnetic field in a medium), $\vec{\mathbf{j}}$ is the free current density, σ the conductivity and ρ is the free charge density. The tilde on the displacement field $\vec{\tilde{\mathbf{D}}}$ is to distinguish it from the alternative formulation in **(4.14)** which combines the two terms on the right hand side of **(4.3)**. It is also worth noting the relationship between the speed of light *c*, permittivity ε_0 and permeability μ_0 of free space displayed in **(4.10)**.

$$c = \frac{1}{\sqrt{\varepsilon_0 \mu_0}} \tag{4.10}$$

Some assumptions and approximations can be used to help simplify the equations. The time dependence of the electric field is declared to be $e^{i\omega t}$. The relative permeability of most materials for organic photovoltaic applications can be approximated to 1 at optical frequencies, so $\mu_r = 1$ can be assumed. In non-absorbing dielectric media $\vec{\mathbf{j}} = \vec{\mathbf{0}}$ and $\rho = 0$; in an absorbing case, such as this one, a complex permittivity ε can be introduced to combine the right hand side of equation **(4.3)**. Rewriting **(4.8)** using the complex permittivity ε_c gives **(4.11)** overleaf.

$$\vec{\mathbf{D}} = \varepsilon_c \varepsilon_0 \vec{\mathbf{E}} \tag{4.11}$$

Using the time dependence of $\vec{\mathbf{E}}$, and the definition of the complex permittivity in **(4.12)**, it is then possible to derive an expression for $\vec{\mathbf{D}}$, given as **(4.13)**.

$$\varepsilon_c = \varepsilon_r - i\varepsilon_i = \varepsilon_r - i\frac{\sigma}{\omega\varepsilon_0} \tag{4.12}$$

$$\vec{\mathbf{D}} = \tilde{\vec{\mathbf{D}}} - i\frac{\sigma}{\omega}\vec{\mathbf{E}}e^{i\omega t} \tag{4.13}$$

By differentiating both sides it is then possible to rewrite **(4.3)** as **(4.14)**:

$$\nabla \times \vec{\mathbf{H}} = \frac{\partial \overline{\mathbf{D}}}{\partial t} \tag{4.14}$$

The relationship between the complex permittivity and the complex refractive index is given in **(4.15)**. The complex refractive index N can be split into real and imaginary parts as normal, as in **(4.16)**.

$$N^2 = \varepsilon_c \tag{4.15}$$

$$N = n - ik \tag{4.16}$$

For physical reasons the solution with a positive value of n is chosen. This leads to the relation displayed in **(4.17)** and **(4.18)** between the elements of the complex permittivity and complex refractive index.

$$\varepsilon_r = n^2 - k^2 \tag{4.17}$$

$$\varepsilon_i = 2nk \tag{4.18}$$

If the media is anisotropic, ε_r, σ, and $\mu_r$must be treated as tensors rather than scalars. Wave propagation is now dependent on the direction of propagation and accompanying polarisation state. Maintaining the approximation of the relative permeability to 1 yields two slightly modified equations, **(4.19)** and **(4.20)**, for current density and electric field:

$$\vec{\mathrm{j}} = \vec{\vec{\boldsymbol{\sigma}}}\vec{\mathbf{E}} \tag{4.19}$$

$$\vec{\vec{\mathbf{D}}} = \vec{\vec{\boldsymbol{\varepsilon}}}_{\mathbf{r}}\varepsilon_0\vec{\mathbf{E}} \tag{4.20}$$

(4.21) and **(4.22)** are the tensor equivalents of **(4.11)** and **(4.12)**:

$$\vec{\mathbf{D}} = \vec{\vec{\boldsymbol{\varepsilon}}}\varepsilon_0\vec{\mathbf{E}} \tag{4.21}$$

$$\vec{\vec{\boldsymbol{\varepsilon}}} = \vec{\vec{\boldsymbol{\varepsilon}}}_{\mathbf{r}} - i\frac{\vec{\vec{\boldsymbol{\sigma}}}}{\omega\varepsilon_0} \tag{4.22}$$

The permittivity tensor, $\overleftrightarrow{\boldsymbol{\varepsilon}}$, can always be represented in a diagonalised form for a certain choice of coordinate axes; the diagonalised form is shown in **(4.23)**.[97]

$$\overleftrightarrow{\boldsymbol{\varepsilon}}_D = \begin{bmatrix} \varepsilon_1 & 0 & 0 \\ 0 & \varepsilon_2 & 0 \\ 0 & 0 & \varepsilon_3 \end{bmatrix} = \begin{bmatrix} N_1^2 & 0 & 0 \\ 0 & N_2^2 & 0 \\ 0 & 0 & N_3^2 \end{bmatrix} = \overleftrightarrow{\mathbf{N}}_D^2 \tag{4.23}$$

A coordinate rotation matrix, M_R, defined in **(4.24)**, can be used to convert between the general and diagonal cases as in **(4.25)**.[99]

$$M_R = \begin{bmatrix} \cos\gamma\cos\alpha - \cos\beta\sin\alpha\sin\gamma & -\sin\gamma\cos\alpha - \cos\beta\sin\alpha\cos\gamma & \sin\beta\sin\alpha \\ \cos\gamma\sin\alpha + \cos\beta\cos\alpha\sin\gamma & -\sin\gamma\sin\alpha + \cos\beta\cos\alpha\cos\gamma & \sin\beta\cos\alpha \\ \sin\beta\sin\gamma & \sin\beta\cos\gamma & \cos\beta \end{bmatrix} \tag{4.24}$$

$$\overleftrightarrow{\boldsymbol{\varepsilon}} = M_R \begin{bmatrix} \varepsilon_1 & 0 & 0 \\ 0 & \varepsilon_2 & 0 \\ 0 & 0 & \varepsilon_3 \end{bmatrix} M_R^{-1} = \overleftrightarrow{\mathbf{N}}^{\mathbf{2}} \tag{4.25}$$

This general case introduces the three Euler angles, α, β and γ; these are defined in **Figure 4.1**. The solutions for electromagnetic fields inside the device are expected to be in the form of plane harmonic waves. The wave equations are treated in a complex manner where the real part of the wave is the physical meaning. The complex fields depend on the angular frequency and wave vector of the light in the medium, as in **(4.26)** overleaf.

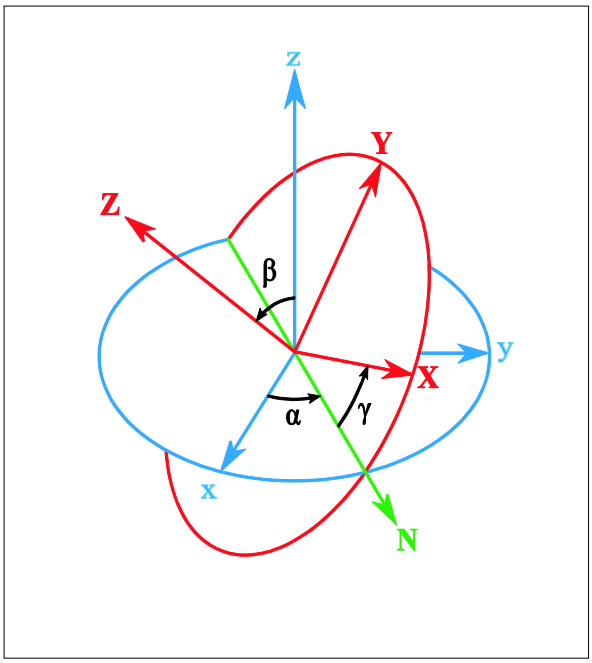

Figure 4.1. Visualisation of the two coordinate systems, XYZ (**ε** diagonalised, in plane with the material) and xyz (laboratory coordinates), and the Euler angles for the transformation between the two. Image created by Lionel Brits, used with permisson.[100]

$$\left.\begin{matrix}\vec{\mathbf{E}}\\ \vec{\mathbf{H}}\end{matrix}\right\} \propto \exp\left(i\left(\omega t - \vec{\mathbf{k}}.\vec{\mathbf{r}}\right)\right) = \exp\left(i\left(\omega t - k_x x - k_y y - k_z z\right)\right) \tag{4.26}$$

Where $\vec{\mathbf{r}}$ is the vector representation of the position and *x*,*y*,*z* are its components in Cartesian coordinates. The real part of the wave vector leads to a change in phase as the wave propagates, while the imaginary part leads to a change in amplitude due to absorption. In isotropic materials, the magnitude of the wave vector is proportional to the complex refractive index of the material and is independent of the direction of the wave vector, as in **(4.27)**.

$$\left|\vec{\mathbf{k}}\right| = (k_x^2 + k_y^2 + k_z^2)^{1/2} = k_0 N \tag{4.27}$$

k_0 is the magnitude of the wave vector in free space, defined as in **(4.28)**.

$$k_0 = \frac{2\pi}{\lambda} \tag{4.28}$$

For anisotropic materials, the magnitude of the wave vector depends on the angle of incidence and it cannot be simplified in the same way.

A plane wave interacting with a planar surface conserves the components of the wave vector in the plane of incidence. The laboratory system is thus chosen so that the x-axis is normal to the surface and the y-axis is in the plane of incidence; this is displayed by the red vectors in **Figure 4.2**.

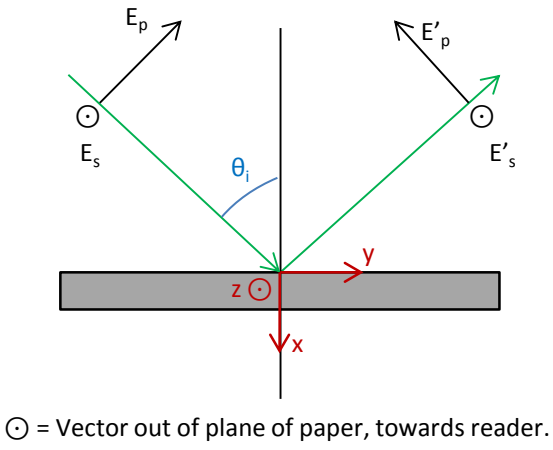

Figure 4.2. Coordinate system chosen for the calculations, with the cardinal vectors in red, relative to the grey substrate / layer stack.

In this coordinate system the component of the wave vector in the z-direction, k_z, is 0. The component of the wave vector in the y-direction, k_y, is an invariant of the system and can be determined by Snell's Law as in **(4.29)**.

$$k_y = N_0 \sin(\theta_0) = N_m \sin(\theta_m) \tag{4.29}$$

k_y thus depends only on the medium of incidence and angle of incidence θ_0. Layers are numbered from the incident material, making the medium of incidence layer 0. A general layer is denoted with use of the subscript *m*, rather than *n*, to avoid confusion with the refractive index. In isotropic media the k_x component can be determined easily from k_y and *N*:

$$k_x^{\pm} = \begin{cases} \pm\left((k_0 N)^2 - k_y^2\right) \text{ if } \mathrm{Im}\left(\left((k_0 N)^2 - k_y^2\right)^{1/2}\right) \leq 0 \\ \mp\left((k_0 N)^2 - k_y^2\right) \text{ if } \mathrm{Im}\left(\left((k_0 N)^2 - k_y^2\right)^{1/2}\right) > 0 \end{cases} \tag{4.30}$$

The sign in **(4.30)** is chosen so that the wave decays in the direction the wave is propagating. In anisotropic media the magnitude of the wave vector depends on the direction of propagation and the polarisation state of the light. The non-trivial solutions for the k_x component inside a layer can be derived from **(4.31)** overleaf.

$$\vec{\mathbf{k}} \times \left(\vec{\mathbf{k}} \times \vec{\mathbf{E}}\right) + \frac{\omega^2}{c^2}\overleftrightarrow{\boldsymbol{\varepsilon}}\vec{\mathbf{E}}$$

$$= \begin{pmatrix} \frac{\omega^2}{c^2}\varepsilon_{xx} - k_y^2 & \frac{\omega^2}{c^2}\varepsilon_{xy} + k_x k_y & \frac{\omega^2}{c^2}\varepsilon_{xz} \\ \frac{\omega^2}{c^2}\varepsilon_{xy} + k_x k_y & \frac{\omega^2}{c^2}\varepsilon_{yy} - k_x^2 & \frac{\omega^2}{c^2}\varepsilon_{yz} \\ \frac{\omega^2}{c^2}\varepsilon_{xz} & \frac{\omega^2}{c^2}\varepsilon_{yz} & \frac{\omega^2}{c^2}\varepsilon_{zz} - k_x^2 - k_y^2 \end{pmatrix} \tag{4.31}$$

For this matrix to have non-trivial plane-wave solutions its determinant must vanish.[101] This leads to a quartic equation which returns four values for k_x, two for forward modes and two for backwards modes. Forward modes have a negative imaginary component and decay as x increases, while backwards modes have a positive imaginary part and decay as x decreases. Evanescent modes result if the magnitude of the wave vector, $|\vec{\mathbf{k}}|$ is smaller than the k_y component, and k_x becomes purely imaginary.

Each solution to **(4.31)** corresponds to a polarisation state of the light. In the isotropic case, when $\varepsilon_{xx} = \varepsilon_{yy} = \varepsilon_{zz}$ and ε_{ij} =0 for $i \neq j$, there are only two distinguishable solutions for the wave vector, distinguished by opposite signs of the k_x component. From the forward and backwards modes it is possible to extract the TE-polarised and TM-polarised wave components with electric field polarisation vectors,$\hat{\mathbf{p}}_i$, where $\hat{\mathbf{p}}_\mathrm{s}$ is s-polarised and $\hat{\mathbf{p}}_\mathrm{p}$ is p-polarised light, as in **(4.32)** and **(4.33)** respectively.

$$\hat{\mathbf{p}}_\mathrm{s} = \begin{pmatrix} 0 \\ 0 \\ 1 \end{pmatrix} \tag{4.32}$$

$$\hat{\mathbf{p}}_{\mathrm{p}} = \frac{1}{k_0 N}\begin{pmatrix} k_y \\ \mp k_x \\ 0 \end{pmatrix} \tag{4.33}$$

The magnetic field vectors, $\bar{\mathbf{q}}_i$, corresponding to the s- and p- polarisation components can then be calculated as shown in **(4.34)** and **(4.35)**.

$$\bar{\mathbf{q}}_s = \sqrt{\frac{\varepsilon_0}{\mu_0}}\frac{1}{k_0}\begin{pmatrix} k_y \\ \mp k_x \\ 0 \end{pmatrix} \tag{4.34}$$

$$\bar{\mathbf{q}}_p = \sqrt{\frac{\varepsilon_0}{\mu_0}} N \begin{pmatrix} 0 \\ 0 \\ 1 \end{pmatrix} \tag{4.35}$$

In the general anisotropic case, the total electric and magnetic fields of a plane wave can be written as a combination of the four modes, given in **(4.36)** and **(4.37)**. The column vector $\mathbf{k}_i$ is defined in **(4.38)** and the relationship between the electric and magnetic field polarisation vectors is outlined in **(4.39)**.

$$\bar{\mathbf{E}}(\bar{\mathbf{r}}) = \sum_{i=1}^{4} c_i \hat{\mathbf{p}}_i \exp(i(\omega t - \bar{\mathbf{k}}.\bar{\mathbf{r}})) \tag{4.36}$$

$$\bar{\mathbf{H}}(\bar{\mathbf{r}}) = \sum_{i=1}^{4} c_i \hat{\mathbf{q}}_i \exp(i(\omega t - \bar{\mathbf{k}}.\bar{\mathbf{r}})) \tag{4.37}$$

$$\bar{\mathbf{k}}_i = \left[k_{xi}, k_y, 0\right]^T \tag{4.38}$$

$$\bar{\mathbf{q}}_{\mathbf{i}} = \sqrt{\frac{\boldsymbol{\varepsilon_0}}{\boldsymbol{\mu_0}}}\frac{\mathbf{1}}{\mathbf{k_0}}\bar{\mathbf{k}}_i \times \hat{\mathbf{p}}_{\mathbf{i}} \tag{4.39}$$

In order to calculate the total electromagnetic field within a layer, the amplitudes of each component must be defined. To model a multilayer structure the electric and magnetic fields at each interface must be considered, in what is termed the transfer matrix method.[102] In order to do these calculations, the complex refractive index

and layer thicknesses of all layers present, including the ambient, must be known. For photovoltaic devices such as those presented in this thesis, the final layer is usually a metal electrode, which is highly absorbing and can be treated as a semi-infinite layer, as shown in **Figure 4.3**.

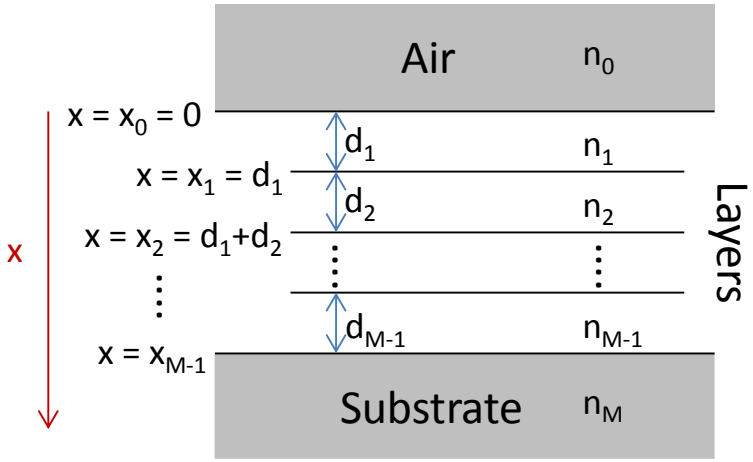

Figure 4.3. Schematic showing the layer structure, with numbering system n_i represents the refractive index of each layer, d_i the layers' thickness, and x the overall position measured from the air interface.

The column vector **c***(m)* represents the amplitudes of the electromagnetic field in each region, so that the fields in region *m* are given by equations **(4.40)** and **(4.41)**.

$$\bar{\mathbf{E}}(x,y) = \sum_{i=1}^{4} c_i(m)\hat{\mathbf{p}}_i(m)\exp(i[\omega t - (k_{xi}(m)(x - x_{m-1}) + k_y y)]) \tag{4.40}$$

$$\bar{\mathbf{H}}(x,y) = \sum_{i=1}^{4} c_i(m)\hat{\mathbf{q}}_i(m)\exp(i[\omega t - (k_{xi}(m)(x - x_{m-1}) + k_y y)]) \tag{4.41}$$

Where $\hat{\mathbf{p}}_i(m)$, $\bar{\mathbf{q}}_\mathbf{i}(m)$, and $k_{xi}(m)$ represent, for layer *m*, the electric field vectors, magnetic field vectors, and x-component of the wave vector respectively. Position *x* is measured from the ambient interface and x_{m-1} represents the thickness of the layers from ambient up to the beginning of the current layer *m*.

The electric and magnetic fields in each layer can be linked through the continuity of the fields at the interfaces.[97] Only four electromagnetic field components are needed to obtain a solution, so the x-components of the fields are eliminated and the tangential field expressions derived.[103]

It is then possible to define two sets of matrices that show how the light propagates through the layer structure, given in **(4.42)** and **(4.43)**. Respectively, they are the dynamical matrices, Δ_m which depend on the polarisation of the light and define how the light passes each interface; and the propagation matrices, Γ_m which define the change of phase and amplitude within each layer.

$$\Delta_m = \begin{pmatrix} \hat{\mathbf{p}}_1(m).\hat{\mathbf{z}} & \hat{\mathbf{p}}_2(m).\hat{\mathbf{z}} & \hat{\mathbf{p}}_3(m).\hat{\mathbf{z}} & \hat{\mathbf{p}}_4(m).\hat{\mathbf{z}} \\ \vec{\mathbf{q}}_1(m).\hat{\mathbf{y}} & \vec{\mathbf{q}}_2(m).\hat{\mathbf{y}} & \vec{\mathbf{q}}_3(m).\hat{\mathbf{y}} & \vec{\mathbf{q}}_4(m).\hat{\mathbf{y}} \\ \vec{\mathbf{q}}_1(m).\hat{\mathbf{z}} & \vec{\mathbf{q}}_2(m).\hat{\mathbf{z}} & \vec{\mathbf{q}}_3(m).\hat{\mathbf{z}} & \vec{\mathbf{q}}_4(m).\hat{\mathbf{z}} \\ \hat{\mathbf{p}}_1(m).\hat{\mathbf{y}} & \hat{\mathbf{p}}_2(m).\hat{\mathbf{y}} & \hat{\mathbf{p}}_3(m).\hat{\mathbf{y}} & \hat{\mathbf{p}}_4(m).\hat{\mathbf{y}} \end{pmatrix} \tag{4.42}$$

$$\Gamma_\mathrm{m} = \begin{pmatrix} e^{ik_{x1}(m)d_m} & 0 & 0 & 0 \\ 0 & \mathrm{e}^{ik_{x2}(m)d_m} & 0 & 0 \\ 0 & 0 & \mathrm{e}^{ik_{x3}(m)d_m} & 0 \\ 0 & 0 & 0 & \mathrm{e}^{ik_{x4}(m)d_m} \end{pmatrix} \tag{4.43}$$

The column vectors of adjacent layers can be linked with **(4.44)**.

$$\begin{pmatrix} c_1(m-1) \\ c_2(m-1) \\ c_3(m-1) \\ c_4(m-1) \end{pmatrix} = \Delta_{m-1}^{-1}\Delta_{\mathrm{m}}\Gamma_{\mathrm{m}} \begin{pmatrix} c_1(m) \\ c_2(m) \\ c_3(m) \\ c_4(m) \end{pmatrix} = \overleftrightarrow{\mathbf{M}}_{\mathrm{m-1,m}} \begin{pmatrix} c_1(m) \\ c_2(m) \\ c_3(m) \\ c_4(m) \end{pmatrix} \tag{4.44}$$

Applying this equation in sequence, as in **(4.45)**, allows relation of the fields in the ambient medium with any other layer, up to the metal electrode layer, represented by **c***(M)*.

$$\begin{pmatrix} c_1(0) \\ c_2(0) \\ c_3(0) \\ c_4(0) \end{pmatrix} = \overleftrightarrow{\mathbf{M}}_{0,1} \dots \overleftrightarrow{\mathbf{M}}_{m-1,m} \dots \overleftrightarrow{\mathbf{M}}_{M-1,M} \begin{pmatrix} c_1(M) \\ c_2(M) \\ c_3(M) \\ c_4(M) \end{pmatrix} = \overleftrightarrow{\mathbf{M}} \begin{pmatrix} c_1(M) \\ c_2(M) \\ c_3(M) \\ c_4(M) \end{pmatrix} \tag{4.45}$$

The order of the components in such a column vector is not important, though consistency is required to perform further calculations. The convention adopted here is for $c_1$and c_2 to be the forward and backward modes for the TE-polarised light and c_3 and c_4 for TM-polarised light. Anisotropic layers make this slightly less straightforward but a consistent convention is still possible.

A total of four components can be assigned. The column vector of the ambient's two forward modes are set as input parameters, depending on the light source, while the backward modes in the electrode are set to be zero, reasoning there will be no light originating in a thick absorbing layer. This can be valid even for a weakly absorbing final layer provided it is thick enough to lead to incoherence of the light, and light reflected back into the device from the other side can be treated as a separate problem with the layer structure reversed. Calculation of the components of all the

column vectors can then be achieved to obtain **(4.46)** using transfer matrices in the same manner as **(4.45)**:

$$\begin{pmatrix} c_1(m) \\ c_2(m) \\ c_3(m) \\ c_4(m) \end{pmatrix} = \overleftrightarrow{\mathbf{M}}_{m,m+1} \dots \overleftrightarrow{\mathbf{M}}_{M-1,M} \begin{pmatrix} c_1(M) \\ 0 \\ c_3(M) \\ 0 \end{pmatrix} = \overleftrightarrow{\mathbf{M}} \begin{pmatrix} c_1(M) \\ 0 \\ c_3(M) \\ 0 \end{pmatrix} \tag{4.46}$$

Where $c_1(M)$ and $c_3(M)$ can be calculated using **(4.47)** and **(4.48)**:

$$c_1(M) = \frac{c_1(0)M_{33} - c_3(0)M_{13}}{M_{11}M_{33} - M_{13}M_{31}} \tag{4.47}$$

$$c_3(M) = \frac{c_3(0)M_{11} - c_1(0)M_{31}}{M_{11}M_{33} - M_{13}M_{31}} \tag{4.48}$$

M_{ij} is a matrix element of the combined transfer matrix. Application of the Poynting vector **(4.49)** allows calculation of the absorption from the field amplitudes in the device.[102]

$$\vec{\mathbf{P}} = \mathrm{Re}(\vec{\mathbf{E}}) \times \mathrm{Re}(\vec{\mathbf{H}}) \tag{4.49}$$

The Poynting vector oscillates at twice the frequency of the wave, but it is the averaged value that is normally observed. The mean value can be obtained by averaging the cross product over one period τ as in **(4.50)**:

$$\langle \vec{\mathbf{P}} \rangle_t = \frac{1}{\tau}\int_0^{\tau} \left(\mathrm{Re}(\vec{\mathbf{E}}) \times \mathrm{Re}(\vec{\mathbf{H}})\right) dt = \frac{1}{2} Re(\vec{\mathbf{E}} \times \vec{\mathbf{H}}^*) \\ = \frac{1}{2} Re(\vec{\mathbf{E}}^* \times \vec{\mathbf{H}}) \tag{4.50}$$

For absorbing media, all waves will be able to interact with each other. This leads to the mixed Poynting vector.[104] In such a situation the total energy flux is therefore defined by **(4.51)**:

$$\langle \vec{\mathbf{P}}_{total}(\mathbf{x}) \rangle_t \\ = \frac{1}{2}\mathrm{Re}\left[\left(\sum_{i=1}^{4} c_i(x)\vec{\mathbf{p}}_{\mathbf{i}}(x)\right) \times \left(\sum_{i=1}^{4} c_i(x)\vec{\mathbf{q}}_{\mathbf{i}}(x)\right)^*\right] \tag{4.51}$$

Since it is the energy transport in the x-direction that is interesting, only the component of the Poynting vector in this direction needs to be calculated. The components in the yz-plane are spatially invariant and not of interest. The Poynting vector allows calculation of the reflectance, transmittance and absorption of the device, normalised to the incident energy flux. Selecting for the x-component gives the power in each case, with incident power represented by (4.52), and reflected and transmitted power by (4.53) and (4.54) respectively.

$$\mathrm{P}_{incident} = \left[\frac{1}{2} Re\left(\left(c_1(0)\hat{\mathbf{p}}_1(0) + c_3(0)\hat{\mathbf{p}}_3(0)\right) \times \left(c_1^*(0)\overline{\mathbf{q}}_1^*(0) + c_3^*(0)\overline{\mathbf{q}}_3^*(0)\right)\right)\right] \tag{4.52}$$

$$\mathrm{P}_{reflected} = \left[\frac{1}{2} Re\left(\left(c_2(0)\hat{\mathbf{p}}_2(0) + c_3(0)\hat{\mathbf{p}}_4(0)\right)\right.\right. \tag{4.53}$$
$$\left.\left. \times \left(c_2^*(0)\overline{\mathbf{q}}_2^*(0) + c_4^*(0)\overline{\mathbf{q}}_4^*(0)\right)\right)\right]$$

$$\mathrm{P}_{transmitted} = \left[\frac{1}{2} Re\left(\left(c_1(M)\hat{\mathbf{p}}_1(M) + c_3(M)\hat{\mathbf{p}}_3(M)\right)\right.\right. \tag{4.54}$$
$$\left.\left. \times \left(c_1^*(M)\overline{\mathbf{q}}_1^*(M) + c_3^*(M)\overline{\mathbf{q}}_3^*(M)\right)\right)\right]$$

Modes of differing polarisation state do not interact with each other in isotropic parts of a multi-layer system, and modes travelling in opposite directions interact only if the medium has a complex refractive index. This allows for a separate treatment of the ambient, the metal layer and the absorbing layers. The power flux carried by a given mode can be calculated by **(4.55)**:

$$\mathrm{P_i}(m) = |c_i(m)|^2 \frac{1}{2} \langle \mathrm{Re}(\hat{\mathbf{p}}_i(m) \times \overline{\mathbf{q}}_i^*(m)) \rangle_x \tag{4.55}$$

In anisotropic layers it is possible to have modes that consist of a combination of s- and p-polarisations. TE and TM polarisation cannot be treated separately in this case, and R and T are instead matrices:

$$R = \begin{pmatrix} R_{ss} & R_{ps} \\ R_{sp} & R_{pp} \end{pmatrix} \tag{4.56}$$

$$T = \begin{pmatrix} T_{ss} & T_{ps} \\ T_{sp} & T_{pp} \end{pmatrix} \tag{4.57}$$

$$\begin{pmatrix} R_{ss} & R_{ps} \\ R_{sp} & R_{pp} \end{pmatrix} \begin{pmatrix} P_1(0) \\ P_3(0) \end{pmatrix} = \begin{pmatrix} P_2(0) \\ P_4(0) \end{pmatrix} \tag{4.58}$$

$$\begin{pmatrix} T_{ss} & T_{ps} \\ T_{sp} & T_{pp} \end{pmatrix} \begin{pmatrix} P_1(0) \\ P_3(0) \end{pmatrix} = \begin{pmatrix} P_1(M) \\ P_3(M) \end{pmatrix} \tag{4.59}$$

Where:

$$R_{ss} = \left|\frac{M_{21}M_{33} - M_{23}M_{31}}{M_{11}M_{33} - M_{13}M_{31}}\right|^2 \frac{F_2(0)}{F_1(0)} \tag{4.60}$$

$$R_{sp} = \left|\frac{M_{33}M_{41} - M_{31}M_{43}}{M_{11}M_{33} - M_{13}M_{31}}\right|^2 \frac{F_4(0)}{F_1(0)} \tag{4.61}$$

$$R_{ps} = \left|\frac{M_{11}M_{23} - M_{13}M_{21}}{M_{11}M_{33} - M_{13}M_{31}}\right|^2 \frac{F_2(0)}{F_3(0)} \tag{4.62}$$

$$R_{pp} = \left|\frac{M_{11}M_{43} - M_{13}M_{41}}{M_{11}M_{33} - M_{13}M_{31}}\right|^2 \frac{F_4(0)}{F_3(0)} \tag{4.63}$$

$$T_{ss} = \left|\frac{M_{33}}{M_{11}M_{33} - M_{13}M_{31}}\right|^2 \frac{F_1(M)}{F_1(0)} \tag{4.64}$$

$$T_{ss} = \left|\frac{-M_{31}}{M_{11}M_{33} - M_{13}M_{31}}\right|^2 \frac{F_3(M)}{F_1(0)} \tag{4.65}$$

$$T_{ss} = \left|\frac{-M_{13}}{M_{11}M_{33} - M_{13}M_{31}}\right|^2 \frac{F_1(M)}{F_3(0)} \tag{4.66}$$

$$T_{ss} = \left|\frac{M_{11}}{M_{11}M_{33} - M_{13}M_{31}}\right|^2 \frac{F_3(M)}{F_3(0)} \tag{4.67}$$

Effectively each can be constructed from elements of the transfer matrices and the field vectors. To calculate the Poynting vector in the m^{th} layer at distance d' from the previous interface, the column vector for that position is calculated using a slightly modified propagation matrix $\Gamma'_m(d')$.

$$\vec{\mathbf{c}}' = \Gamma'_m(d')\vec{\mathbf{c}}(m) \tag{4.68}$$

Once the Poynting vector, and thus energy flux, is known, the proportion of light absorbed at a position *x* can be calculated from the gradient of the Poynting vector:

$$\alpha(x) = -\frac{dP_x(x)}{dx} \tag{4.69}$$

Given this method for calculating absorptance at a point, performing this calculation for all positions of interest in the device leads to a complete absorptance profile. Comparison of this absorptance profile with External Quantum Efficiency (EQE) (see **1.5.4**) measurements allows an estimation of the Internal Quantum Efficiency (IQE), as given by **(4.70)**.

$$IQE = Q_{Diff}Q_{Diss}Q_T = \frac{EQE}{Q_A} \tag{4.70}$$

Multiplying the absorptance by the incident photon flux *qp* as in **(4.71)** leads to a measure of the exciton generation rate in the material:

$$E_{gen} = \alpha(x)qp \tag{4.71}$$

The photon flux can be calculated easily from the intensity I_0 of the incoming radiation using **(4.72)** overleaf.

$$qp = \frac{I_0 \lambda}{hc} \tag{4.72}$$

Making these calculations for each wavelength for a single cell yields an upper limit for the current generation. If the IQE can be estimated, multiplying the result by it leads instead to an estimate of the short circuit current. In the case of a tandem cell, estimating the short-circuit current of the sub-cells can lead to better current balancing. The ability to predict how the absorptance of the cell will shift with changes in the layer structure is extremely useful for optimisation.

4.2.1. ELLIPSOMETRY

Ellipsometry is a precision technique that is most often used to measure thin film layer thicknesses to a very high degree of accuracy. This measurement is made possible with knowledge of the layer structure and the complex refractive index of all the materials in the stack. However, if the thickness of the layer is known, calculation of the complex refractive index is also possible. As optical modelling requires complex refractive index data, ellipsometry was used to obtain this for the cases where there was no published data. While a complete discussion of ellipsometric theory is beyond the remit of this thesis, some of the basic theory behind the technique is discussed, then the two ellipsometers used for this work introduced. Finally, the results obtained and the analysis performed on them is discussed.

4.2.1.1. THEORY OF ELLIPSOMETRY

Ellipsometry involves measuring the phase and amplitude change of a polarised light beam reflecting off a layer of the material to be measured. This can be a thick layer, such as a substrate, or a thin layer on a known substrate, in which case it must be treated as a layer stack.

Polarisation was discovered in 1808 by Malus when working with calcite crystals,[99] before the classical electromagnetic theory had even been established. The polarisation of the light wave describes the relationship between the electric field components in two arbitrary perpendicular directions. For simplicity these will be chosen to be our coordinate axes, y and z, since x is the direction of propagation, as shown in **Figure 4.4**.

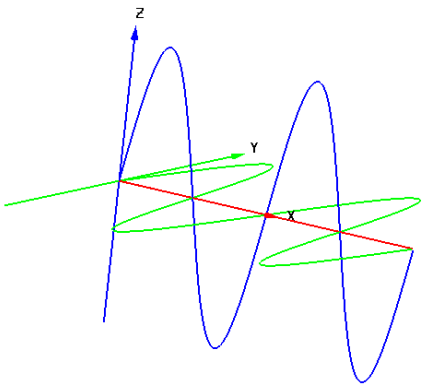

Figure 4.4. Light wave propagating the x-direction with arbitrary electric fields in the y- and z-axis.

The most general case of polarization is elliptic; this is the situation where the total electric field vector (i.e. the vector sum of the two components at any particular

moment) describes an elliptic trajectory as it precesses. The time dependence of the total electric field can thus be formulated as in **(4.73)**:

$$E(t) = \left[\frac{E_z(t)}{E_y(t)}\right] = \mathrm{Re}\left(\left[\frac{Ze^{i\Delta}}{Y}\right]\right) \tag{4.73}$$

Y and *Z* are the amplitudes of the electric field in the *y*- and *z*- directions respectively, and Δ is the *relative phase*, or phase-shift, of the vibrations in *y*- and *z*- directions, usually varying between $-\pi$ and π, or sometimes 0 to 2π. In basic ellipsometric measurements, only the *relative amplitude*, *Z/Y*, is relevant; multiplication of both by a common constant is equivalent to changing the light intensity.

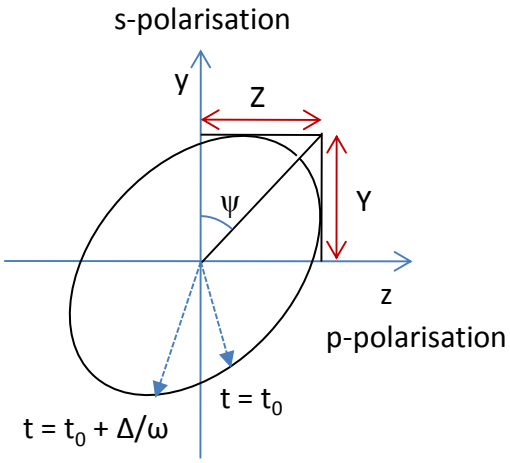

Figure 4.5. Representation of the ellipsometric angles ψ and Δ as related to the components of the electric field in the y- and z-axis.

The relative amplitude can also be expressed in terms of the angle ψ from **Figure 4.5**, where it can be seen that $\tan \psi = Z / Y$, varying from 0 to $\pi/2$. Elliptic polarization can thus be represented by the Jones vector, **(4.74)**, overleaf.

$$\begin{bmatrix} \sin\psi\, e^{i\Delta} \\ \cos\psi \end{bmatrix} \tag{4.74}$$

This relies on the two real angles ψ and Δ. Two polarisation states are said to be orthogonal when their Jones vectors are orthogonal in the usual vector algebra sense. The polarisation orthogonal to **(4.74)** is therefore **(4.75)**:

$$\begin{bmatrix} -\cos\psi\, e^{i\Delta} \\ \sin\psi \end{bmatrix} = \begin{bmatrix} \sin(\frac{\pi}{2} - \psi)\, e^{i(\Delta \pm \pi)} \\ \cos(\frac{\pi}{2} - \psi) \end{bmatrix} \tag{4.75}$$

Ellipsometers rely on manipulating the polarisation state of a light beam incident on and reflected by a sample. The basic setup of an ellipsometer requires a light source, linear polariser (P), retarder (or 'compensator', C), a sample (S), a second linear polariser termed the analyser (A), and a detector.

The source, polariser and compensator produce light of a known polarisation state that is reflected off the sample, through the analyser to the detector. The analyser allows the polarisation of the light hitting the detector to be controlled and thus measured; this setup is shown in a general way in **Figure 4.6**. The angles P,C and A shown are known as the azimuthal angles, or azimuths, and represent the angle between the z-axis of the light and the active angle of the components; this is the permitted polarisation for the polarisers or the fast axis for the compensator.

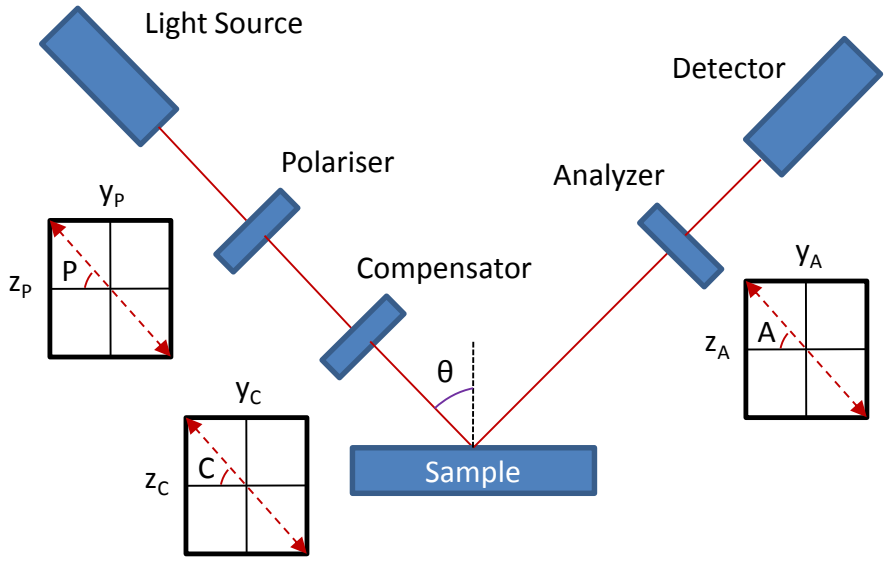

Figure 4.6.Example schematic of a Polariser – Compensator – Sample – Analyser (PCSA) setup for ellipsometry. The angles P, C and A are the azimuths of the components.

The amplitude observed by the detector can be related to the relevant parameters as follows:

$$E_A \begin{bmatrix} 1 \\ 0 \end{bmatrix} = \begin{bmatrix} 1 & 0 \\ 0 & 0 \end{bmatrix} \begin{bmatrix} \cos A & \sin A \\ -\sin A & \cos A \end{bmatrix} \begin{bmatrix} r_p & 0 \\ 0 & r_s \end{bmatrix} \begin{bmatrix} \cos P \\ \sin P \end{bmatrix} E_p \tag{4.76}$$

Where the matrix containing r_p, r_s is the characteristic reflection matrix of the surface. This matrix can easily be extracted from the optical modelling discussed in **Section 4.2**, as calculating the reflection from the stack is integral to calculating transmittance and absorptance. Ellipsometry is discussed in more detail in the *Handbook of Ellipsometry*, by Harland G. Tompkins and Eugene A. Irene.[99]

4.2.1.2. DATA ANALYSIS

The useful quantities in ellipsometry – film thickness, refractive index and roughness – can only be extracted by modelling the near-surface region of the sample and fitting the ellipsometry data, with the unknown variable as a fitting parameter. This makes the data analysis in ellipsometry critical; the ellipsometric angles Δ and ψ are not that interesting by themselves.

To perform any parameterization, it is necessary to have realistic models of the dielectric functions as functions of wavelength. One of the oldest models is the Lorentz-oscillator model, which assumes the solid is a collection of non-interacting oscillators. This model is only valid for photon energies much less than the band gap of the material, and is given by **(4.77)**:

$$\varepsilon(\lambda) = \tilde{n}(\lambda)^2 = 1 + \sum_j \frac{A_j \lambda^2}{\lambda^2 - \lambda_{0j}^2 + i\zeta_j \lambda} \tag{4.77}$$

A_j, λ_{0j}, and ζ_j are all parameters to be fitted, unless they have previously been determined for this film. It is also possible to rewrite this in terms of energy, in which case the parameters used are slightly different. Several other models are based on the Lorentz oscillator model, such as the Sellmaier approximation, which assumes the extinction coefficient is zero; given as **(4.78)**.

$$\varepsilon = n^2 = 1 + \sum_j \frac{A_j \lambda^2}{\lambda^2 - \lambda_{0j}^2} \tag{4.78}$$

The Cauchy expansion is often used as a first port of call for materials with no significant absorption; given as **(4.79)** overleaf.

$$n = B_0 + \sum_j \frac{B_j}{\lambda^{2j}} \tag{4.79}$$

The Drude expression is also related to the Lorentz model, and is used to express the optical functions of metals and the free carrier effects in semiconductors; given as **(4.80)**.

$$\varepsilon(E) = 1 - \sum_j \frac{B_j}{E}\left(\frac{1}{E - i\Gamma_j}\right) \tag{4.80}$$

In all of these models, the parameters other than the photon energy, *E*, or wavelength, λ, are parameters to be fitted. While all of these models include a summation over index *j*, most of the time a single term is sufficient to achieve the accuracy required for spectroscopic ellipsometry, although more terms can be included to increase the accuracy if required.

Many thin film materials encountered in ellipsometry are amorphous or nearly amorphous, particularly organic materials. Optical transitions in such materials are well known to have no **k**-vector conservation, leading to optical functions lacking sharp features characteristic of crystalline materials. The optical functions may also vary considerably with growth conditions, leading to a diversity of optical properties. There have been many attempts to parameterise the optical functions in such materials; however, based on the limitations of most approaches,[99] only one is presented here: The Tauc-Lorentz formulation.

This empirical formulation stems from the Lorentz oscillator model and the Tauc expression for the imaginary part of the dielectric function near the band edge. For a single transition this leads to **(4.81)**:

$$\varepsilon_2(E) = 2n(E)k(E) = \frac{A(E - E_g)^2}{(E^2 - E_0^2)^2 + \Gamma^2}\frac{\Theta(E - E_g)}{E} \tag{4.81}$$

Θ here is the Heaviside function [Θ(*E*) = 1 for $E \geq 0$ and Θ(*E*) = 0 for $E < 0$]. The other parameters are, again, entered into the fitting procedure unless previously determined. The real part of the dielectric function is obtained via Kramers-Kronig integration, defined as in **(4.82)**:

$$\varepsilon_1(E) = \varepsilon_1(\infty) + \frac{2}{\pi}P\int_{R_g}^{\infty}\frac{\xi\varepsilon_2(\xi)}{\xi^2 - E^2}d\xi \tag{4.82}$$

The P here denotes the Cauchy Principal Value (CPV) of the integral; this is used to assign values to improper integrals. This integral is improper because $\xi^2 - E^2$ will be zero at some point in the range. In this case the CPV can be calculated analytically; the full form can be found on page 257 of the Handbook of Ellipsometry.[99]

Handling crystalline materials is more complicated than amorphous ones, since the long-range order leads to critical points in the band structure, which show up as sharp features in the optical functions.

It is sometimes desirable to use an average of two or more sets of optical functions, for example in blends of organic molecules or to simulate a rough sample-air or sample-substrate interface. The primary difference between the methods for this is the choice of averaging technique. These methods are generally termed 'Effective Medium Approximations' (EMAs). More information can be found on page 260 of the Handbook, or in Effective Medium Theory, by T. Choy.[99, 105]

Different approximations can be used for different situations, for example, the Maxwell-Garnett EMA may be appropriate when the ratio of materials heavily favours one, allowing that material to be treated as the host material. In contrast, the Bruggerman approximation might be chosen when the ratio of materials is more equal, as it makes no assumptions about either material dominating the dispersion function.

4.2.1.3. FITTING PROCEDURE

The fitting procedure can be split into three stages. Firstly, the layer structure must be chosen; for example substrate – sample – air, or substrate – sample – roughness layer – air. Thicknesses, if known, are also assigned to each layer; if unknown the best guess is usually used initially.

Secondly, the optical functions of each layer need to be defined, either by using a pre-existing dataset or through dispersion models or EMAs.

Finally, an algorithm and a metric must be chosen that allow any undetermined parameters to be pinned down. Fewer parameters usually make the fitting easier, faster, and more accurate. The choice of metric is quite important as it is what decides whether a model actually fits the data or not. The most satisfactory metric for ellipsometric data is generally accepted to be the reduced χ^2, given below as **(4.83)**:

$$\chi^2 = \frac{1}{N-m-1}\sum_{j=1}^{N}\frac{\left[\rho_{exp}(\lambda_j) - \rho_{calc}(\lambda_j, \mathbf{z})\right]^2}{\sigma(\lambda_j)^2} \tag{4.83}$$

This is a nice metric for a number of reasons; firstly, a perfect fit has $\chi^2 = 1$, meaning the ideality is defined unambiguously. Furthermore, the errors of the data set can be included in the fitting algorithm, allowing points with a large error to be weighted less heavily.

4.3. EXPERIMENTAL

The transfer matrix model was implemented in MATLAB initially based on a set of scripts created by Felix Braun,[103] used with permission from Jenny Nelson at Imperial College. The script was rewritten in Python to facilitate a graphical interface, making interpreting the wealth of data generated easier and faster. The original script was also extended to include current estimations assuming 100% IQE. The changes allowed the script to be run more easily by other users, and while execution time increased slightly the Python version is a lot easier to use and performs more analysis useful for solar cells than the original did. It also has the capability to save and load structures from files, while the output is saved automatically in a format that can easily be read by other programs. The main GUI page is displayed in **Figure 4.7**; this screen is for sample definition and management, and also spectra and materials management. The Results browser is displayed in **Figure 4.8**; this is designed for quick overview and comparison of results. The window is tabbed to swap easily between different result types, and roughly graphs results for visualisation.

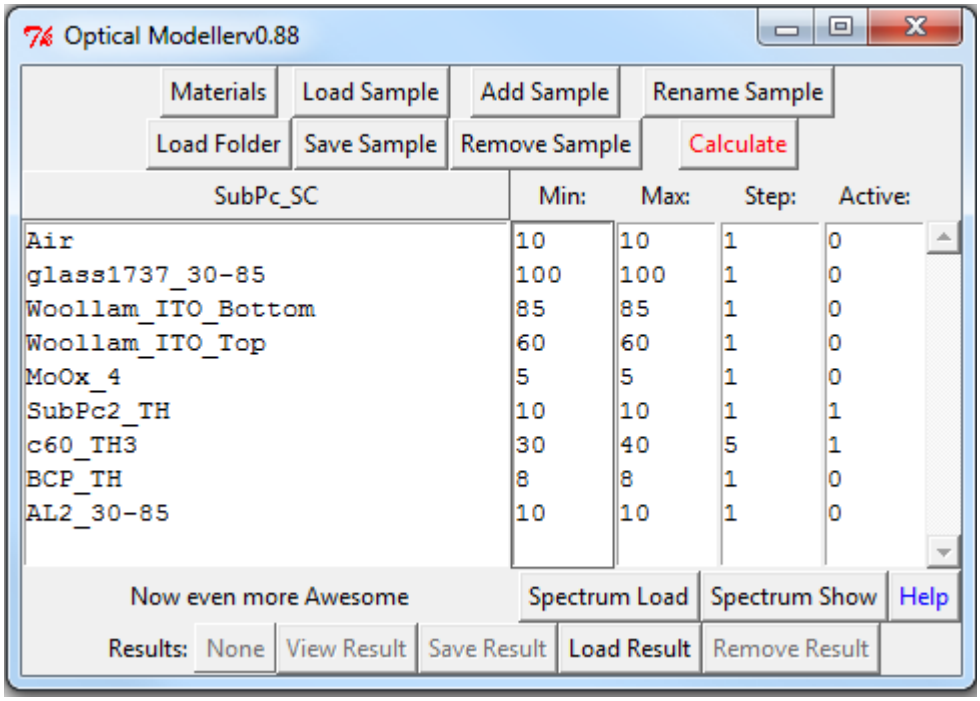

Figure 4.7. Optical modeller GUI. Multiple samples can be loaded at once, and samples can be saved and loaded easily. The sample definition area is interactive to make design as intuitive as possible.

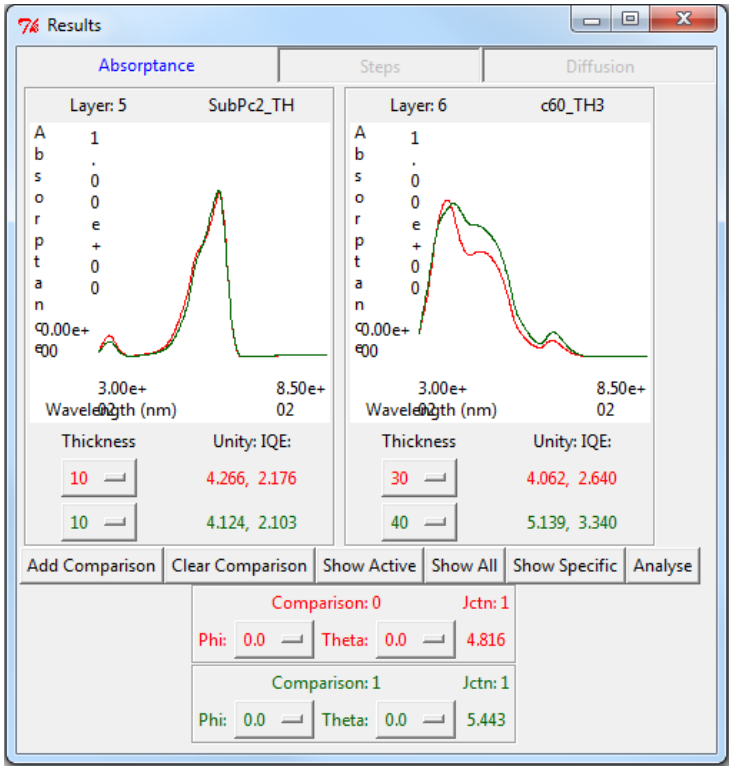

Figure 4.8. Results GUI for optical modeller, on the absorptance tab. Designed for rough graphing of data for preliminary analysis.

The majority of the complex refractive index data was obtained from literature reports or from Jenny Nelson at Imperial College along with the Matlab scripts. Literature values were used for SubPc,[106] C_{60},[107] BCP,[108] and MoO_3,[109] while Aluminium, glass, TiO_2, and ITO were obtained from Jenny Nelson. ClAlPc was obtained by ellipsometry, as explained in **Section 4.4.1**. The description of the ellipsometers can be found in **Section 2.7**.

4.4. RESULTS

The ellipsometry undertaken to determine the complex refractive index of ClAlPc is presented first, followed by optical modelling as applied to two distinct sets of cells, the first being a set of interesting single cells where optical interference was particularly relevant, and the second set being tandem cells similar to those discussed in **Section 3.4**.

4.4.1. ELLIPSOMETRY

Ellipsometry was used to characterise the complex refractive index of ClAlPc. Initially, 30 nm and 50 nm layers were grown on Quartz and Silicon-100 substrates, and then measured on the EP3. The results of the measurement are shown in **Figure 4.9** for the 50 nm layer on ITO, together with the best model fit to the data.

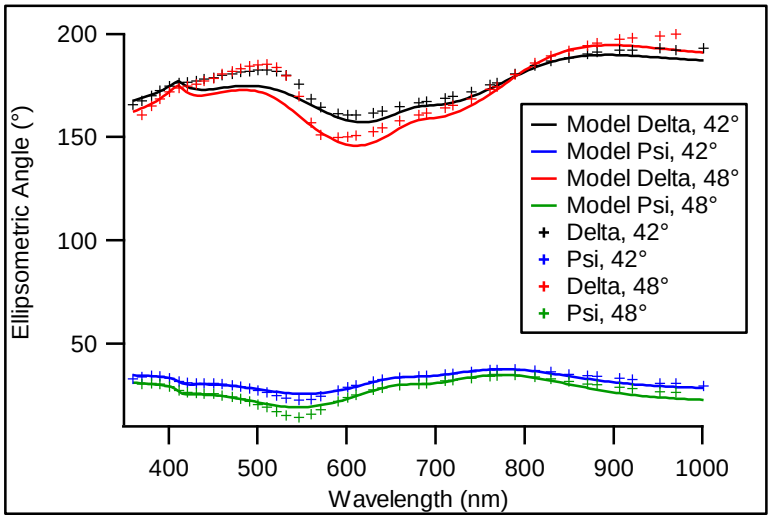

Figure 4.9. Fit to the ellipsometric angles utilizing the three-peak Tauc Lorentz model from **Table 4.1**.This sample was a 50 nm layer of ClAlPc on a glass / ITO substrate, measured at two angles of incidence, 42° and 48°.

The ClAlPc was modelled as a single layer of material atop the relevant substrates; the organic layer was specified by a combination of three Tauc-Lorentz peaks, one below 400 nm and the others between 600-850 nm. The best fit parameters for the three Tauc-Lorentz (T-L) peaks used are presented in **Table 4.1**.

Table 4.1. Table of parameters used to generate the complex refractive index of ClAlPc.

Peak	A	E_0	Gamma	E_g
T-L #1	62.32	1.609	0.173	1.347
T-L #2	1862.18	2.854	0.265	2.995
T-L #3	2.64	1.850	0.195	1.195

Using this index resulted in a fit with an RMSE of 4.8; the RMSE refers to the combined RMSE from all four samples simultaneously. Lower is generally better when considering the RMSE, although the exact magnitude means little. The complex refractive index prediction generated from these peaks is displayed in **Figure 4.10**, with the 30 nm UV-vis absorption spectrum for comparison. The complex refractive index data calculated is hereafter labelled as 'F1' for clarity.

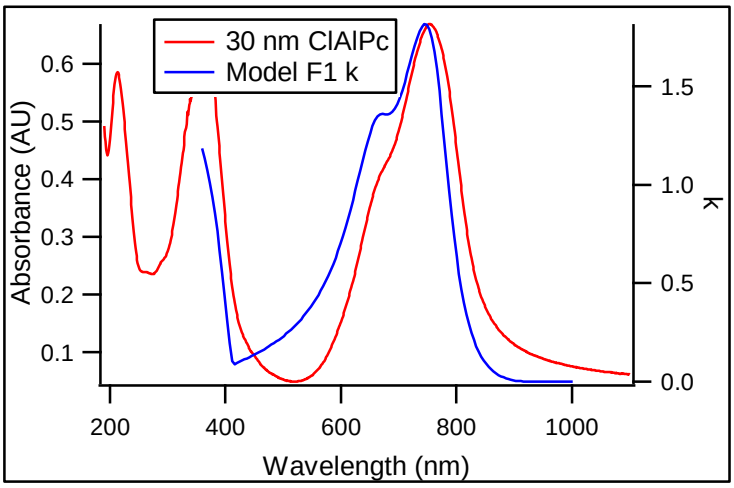

Figure 4.10. Comparison of the complex refractive index calculated from **Table 4.1** (F1) with the UV-vis absorption spectra of a 30 nm ClAlPc film on quartz.

One key issue with this fit is the behaviour at shorter wavelengths, evident even in **Figure 4.9**. Utilizing optical modelling the absorption spectrum was predicted based

on the calculated refractive index, and the calculated and experimental data compared as in **Figure 4.11**.

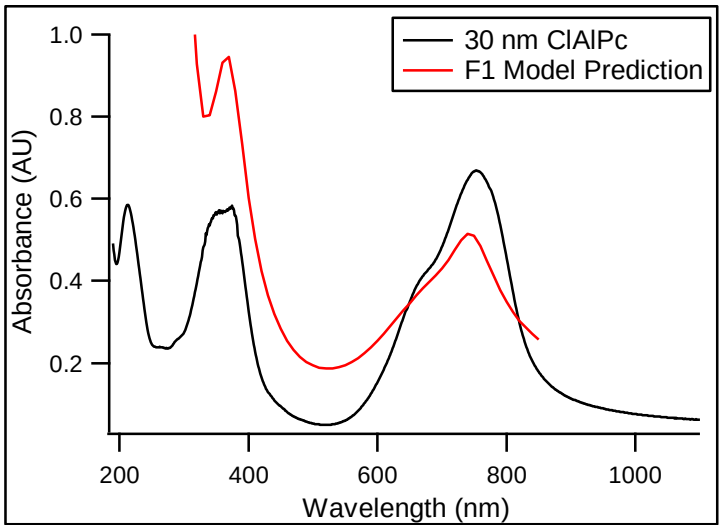

Figure 4.11. UV-vis absorption spectrum compared to a model prediction of absorbance for the first measurement of the refractive index.

To improve this situation, the ellipsometer at Imperial College was utilized since it covers a larger wavelength range; particularly the peak at about 360 nm could be characterised. A second set of samples was prepared and measured, with the results still fitted by the EP4 software. The Delta / Psi results as measured are shown in **Figure 4.12** together with the best model fit.

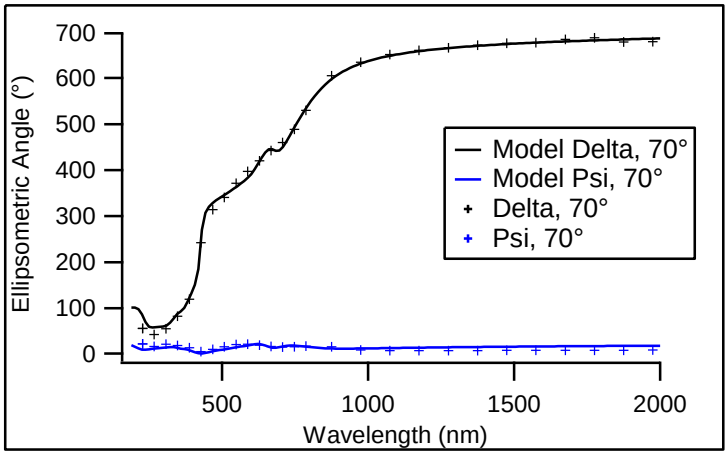

Figure 4.12. Comparison of ellipsometric data with the model fit based on the four-peak dispersion function from **Table 4.2** (F2) for ClAlPc. This measurement was done at 70° angle of incidence on quartz following advice from the staff at Imperial College, as the ellipsometer should be most sensitive near (but not at) the Brewster angle (~68°).

The samples were modelled as single layers on quartz. With the additional wavelength range, the dispersion function was modified to 4 peaks, two Tauc-Lorentz and two Tauc-Lorentz-Urbach (T-L-U) peaks. The best fit parameters for this data are shown in **Table 4.2**; the complex refractive index calculated from these parameters is compared with the first dataset and the absorption spectrum in **Figure 4.13**. The refractive index calculated from this set is labelled 'F2' to avoid confusion with the previous set.

Table 4.2. Parameters used to create the dispersion function in the second fitting.

Peak	A	E_0	Gamma	E_g	E_t	E_u
T-L #1	79.46	6.65	3.13	2.85	n/a	n/a
T-L #2	65.01	3.49	0.53	2.88	n/a	n/a
T-L-U #1	10.57	1.65	0.15	1.03	0.00	3.97
T-L-U #2	2.28	1.89	0.19	0.91	0.00	6.59

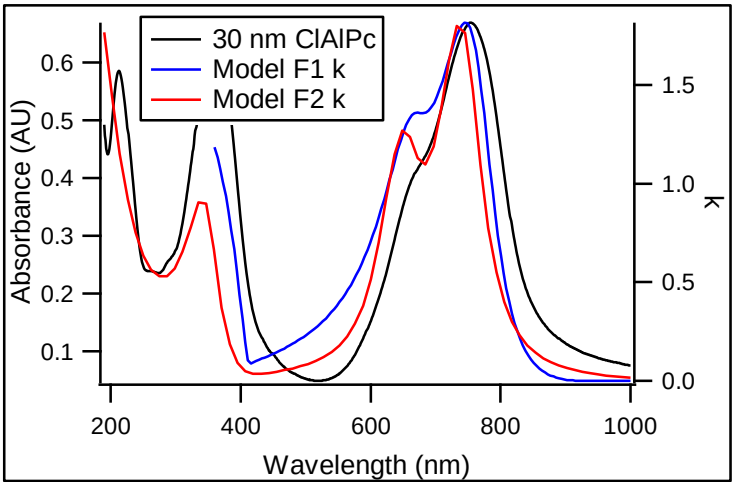

Figure 4.13.Comparison of the imaginary part of the refractive index (k) for both models with the UV-vis.

Use of this index resulted in a fit with an RMSE of 7.9 if only delta is fitted, or 10.2 if both delta and psi are considered. Despite the higher RMSE result, the comparison with the absorption spectrum is favourable (**Figure 4.14**). This is likely due to the increased complexity of the model, and the wider data range fitted. Dataset F2 has since been used for the calculations involving ClAlPc in this thesis.

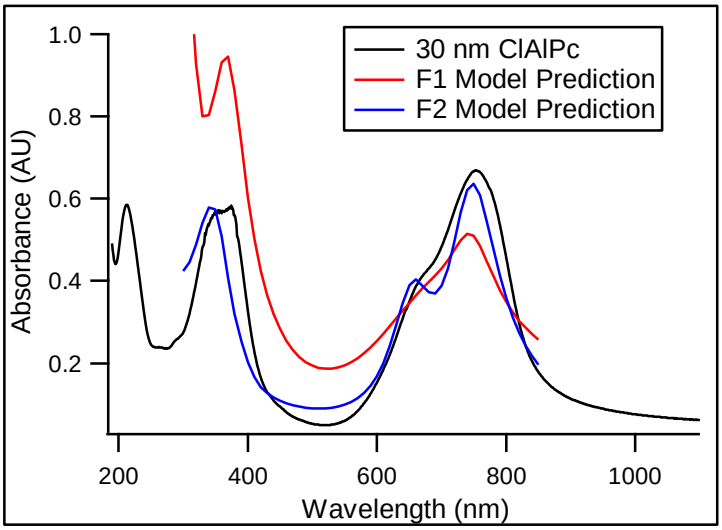

Figure 4.14. Model predictions of absorbance for both models with that measured by UV-vis for a 30 nm layer of ClAlPc on Quartz substrate.

4.4.2. SINGLE CELL MODELLING

The first results presented relate to a series of hybrid single cells grown at Warwick by Chloe Dearden, which consisted of a SubPc donor layer together with a titanium oxide (TiO_x) inorganic acceptor. The titanium oxide was spin-coated as it cannot be vacuum deposited; all other materials were vacuum deposited. This work was in progress concurrently with my own and presented some initially puzzling results when attempting to optimise the SubPc layer. With only one significantly absorbing layer (the SubPc), it is very easy to observe the effects of interference in this system as compared to devices with multiple absorbing layers, or indeed multiple junctions. In the more complicated systems it is much more difficult to directly link the current generation with the position of the layers in the optical electric field. The initial cells used the following configuration:

Glass / ITO / TiO_x (25 nm) / SubPc (14 or 28 nm) / MoO_x (5 nm) / Al electrode.

Cells in this configuration were inconsistent with respect to the exciton diffusion length of the SubPc. The majority of literature reports that the exciton diffusion length in SubPc should be near 10 nm,[69, 110] in agreement with optimised SubPc / C_{60} single cells, but as can be seen from **Table 4.3** the 28 nm SubPc cells showed a better current generation. This result cannot be understood without taking interference in the optical electric field into account.

Table 4.3. Comparison of cell performance with differing SubPc thicknesses.

Device	Voc (V)	Jsc ($mAcm^{-2}$)	FF	PCE (%)
14 nm SubPc / 5 nm MoO_x	0.74	1.02	0.34	0.28
28 nm SubPc / 5 nm MoO_x	0.77	1.36	0.26	0.28

The key to understanding the result is the placement of the SubPc layer in the standing wave set up inside such a device by reflection from the metal electrode. The electric field and per-nm absorptance are plotted in **Figure 4.15**.

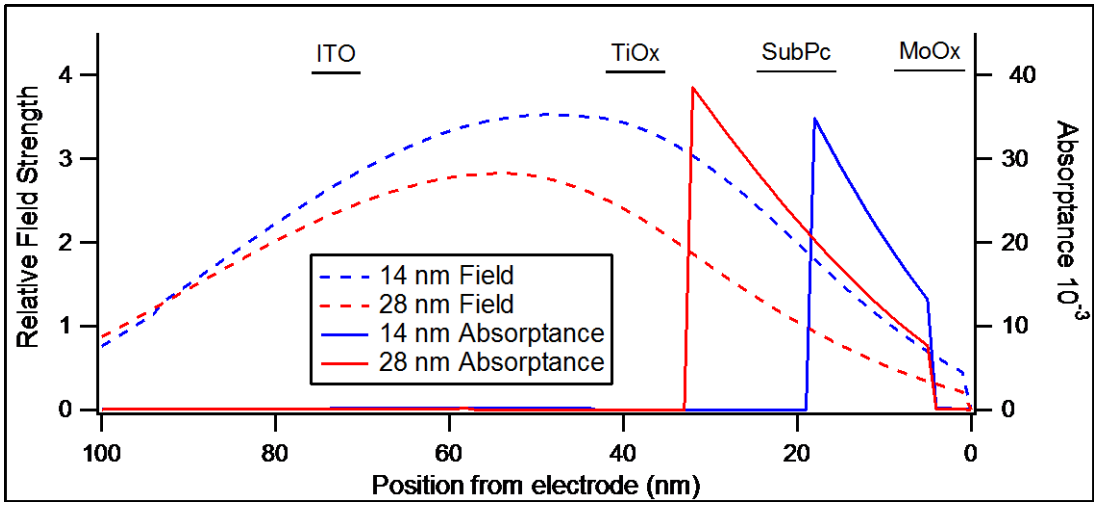

Figure 4.15. Electric field and device absorptance calculations, plotted at 550 nm, for both the 14 nm and 28 nm SubPc devices from **Table 4.3**. The reflective Aluminium electrode is at 0 nm. The order and rough position of the other layers is indicated by the material labels along the top. The highly absorbing SubPc layer shows up clearly in the absorptance traces.

When the MoO_x layer is at 5nm as in **Figure 4.15**, the SubPc layer sits in the region of low field close to the electrode. The position of this layer is identifiable in the absorptance plot by the large peak. It can be seen that with the thicker, 28nm SubPc layer there is a higher peak absorptance at the interface with the TiOx (which is to the left of the peak). Since it is expected that the exciton diffusion length of the SubPc is near 10 nm, higher optical field closer to the interface would yield a higher current.

The total layer absorptance for each device is shown in **Figure 4.16**. Integrating the product of the absorptance at each wavelength and the AM 1.5G spectrum gives a maximum current estimate assuming 100% IQE, shown in **Figure 4.16**. It can be seen that the estimate is higher for the 28 nm case, even when only the 14 nm closest to the interface is considered.

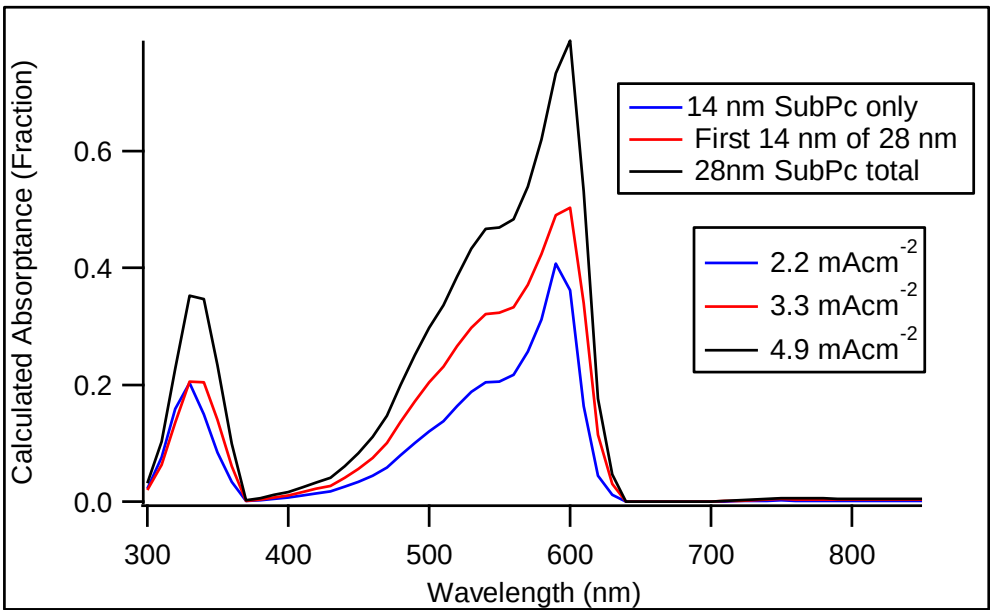

Figure 4.16. Comparison of 14 and 28 nm SubPc layer absorptance with TiO_x acceptor. The current estimates are calculated for AM1.5G illumination with 100% IQE.

The current estimates from **Figure 4.16** suggest that, if all 28 nm of SubPc were contributing to the photocurrent, the current output would more than double as compared to the 14 nm SubPc device. While this doubling is not observed, comparison of the first 14 nm of the 28 nm device to the 14 nm device suggests a more modest increase of 50%, which is much more comparable to the observed 33%. Non-contributing SubPc would be expected to show up as an increased series resistance in the 28 nm devices, due to its low charge mobility.[69] This can be observed in **Table 4.3** as the reduced fill factor of the 28 nm SubPc device. The

presence of 14 nm of potentially non-contributing SubPc leads to the conclusion that the efficiency could be improved by use of a spacer layer in-between the SubPc and the electrode. To confirm this, a second set of cells was grown (again by Chloe Dearden) with both 14 and 28 nm of SubPc and additionally with a varying amount of MoO_x, to be used as an optical spacer, as below;

Glass / ITO / TiO_x (25 nm) / SubPc (14 or 28 nm) / MoO_x (5 - 20 nm) / Al electrode.

The field plot for 20nm of MoOx is given as **Figure 4.17**. In contrast to the 5 nm MoOx devices, the field (and thus absorptance) are now expected to be higher in the 14 nm SubPc device, when considering only the 14 nm closest to the interface.

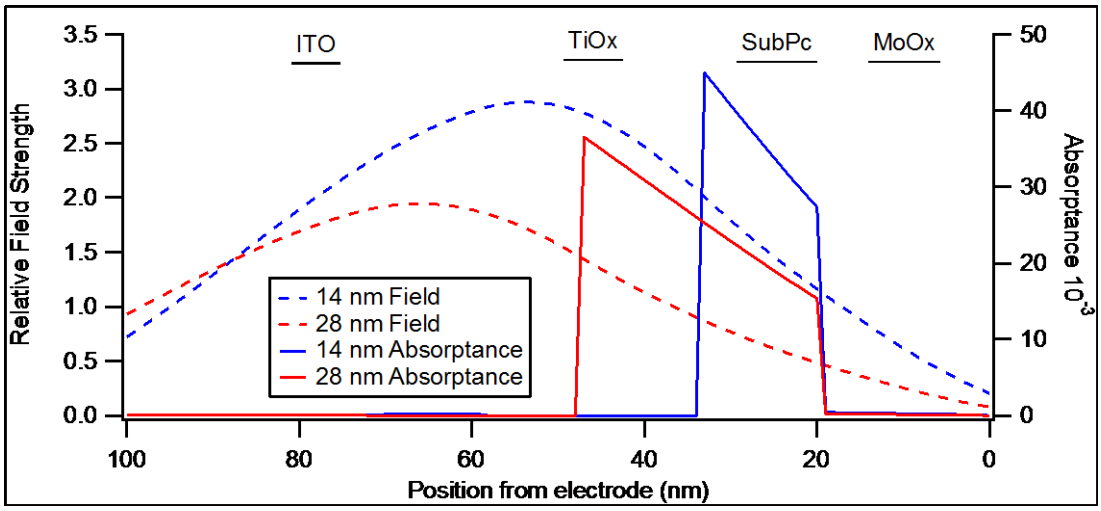

Figure 4.17. Electric field and device absorptance calculations, plotted at 550 nm, for both the 14 nm and 28 nm SubPc devices with 20 nm MoOx spacer layer. The reflective Aluminium electrode is at 0 nm. The order and rough position of the other layers is indicated by the material labels along the top. The highly absorbing SubPc layer shows up clearly in the absorptance traces.

Full wavelength range modelling predictions are given in **Figure 4.18**. As can be seen from the plot, the prediction is for 14 nm of SubPc to be comparable in absorptance with the first 14 nm of the 28 nm SubPc layer when the MoO_x layer is at around 15 nm, which results in roughly the same separation from the reflecting interface, with a further improvement when the MoO_x layer is increased up to 20 nm However, the MoO_x layer is expected to be a better conductor than the extra SubPc, which means the IQE in a real device should be better in the 14 nm SubPc / 20 nm MoO_x case. This is supported by the J-V results from this set of devices, (**Table 4.3**) showing in the superior fill factor of the 14 nm devices.

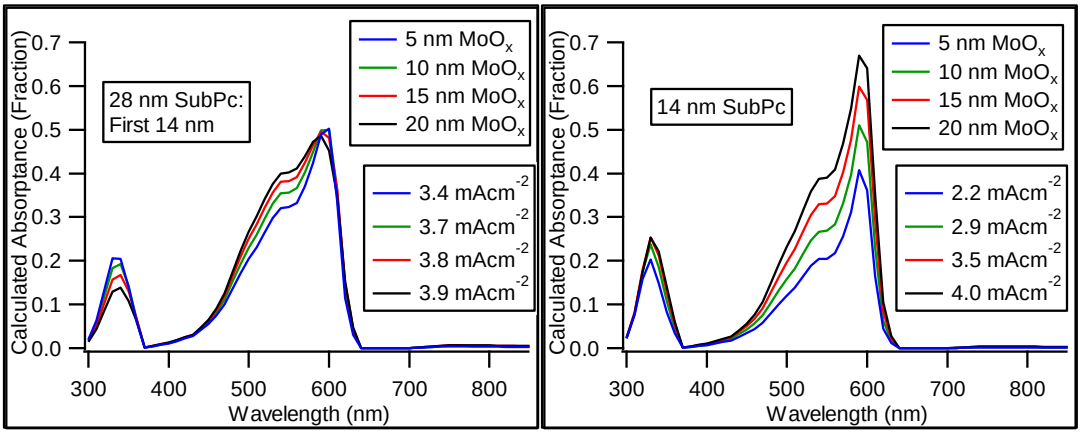

Figure 4.18. Absorptance predictions for 14 and 28 nm SubPc layers, presuming only the 14 nm closest to the TiO_x can contribute.

Table 4.4. Device results comparing differing optical spacing with the two SubPc thicknesses.

Device	Voc (V)	Jsc ($mAcm^{-2}$)	FF	PCE (%)
14 nm SubPc / 5 nm MoO_x	0.74	1.02	0.34	0.28
14 nm SubPc / 10 nm MoO_x	0.71	1.60	0.35	0.42
14 nm SubPc / 15 nm MoO_x	0.70	1.73	0.41	0.53
14 nm SubPc / 20 nm MoO_x	0.85	1.64	0.38	0.58
28 nm SubPc / 5 nm MoO_x	0.77	1.36	0.26	0.28
28 nm SubPc / 10 nm MoO_x	0.80	1.54	0.30	0.38
28 nm SubPc / 15 nm MoO_x	0.84	1.64	0.31	0.45
28 nm SubPc / 20 nm MoO_x	0.75	1.50	0.27	0.33

The EQE results for these cells are given as **Figure 4.19**. Comparison of the EQE with the absorptance predictions allows calculation of the IQE, displayed as **Figure 4.20**. This shows a great improvement in the IQE in the 14 nm SubPc cells as compared to the 28 nm SubPc cells. This improvement in the IQE from better conduction is the reason for the 14 nm devices to be the most efficient overall.

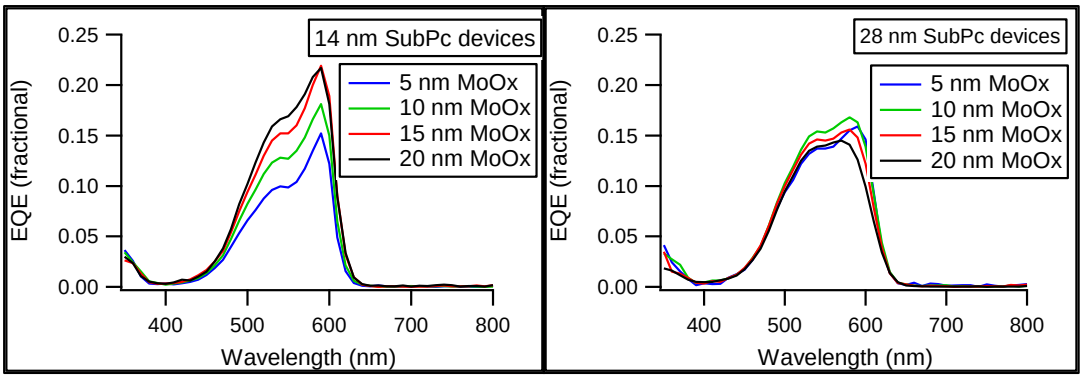

Figure 4.19.EQE of the 14 and 28 nm SubPc device series. The increase in EQE with increased MoOx is obvious in the 14 nm devices, while the minor changes in the 28 nm devices back up the modelling predictions for this system.

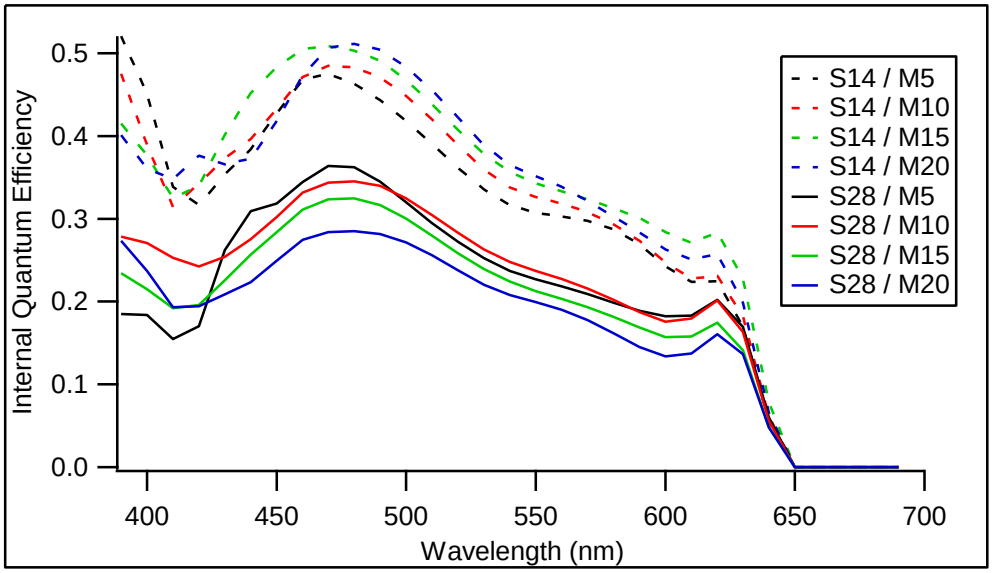

Figure 4.20. Calculated IQE of devices with varying MoO_3 and SubPc thickness.

4.4.3. TANDEM CELL MODELLING

Optical modelling was also applied to tandem cells, where it is of particular interest for calculating current generation in each sub-cell. Of course, optical modelling by itself cannot calculate current generation; as discussed in **Section 4.2**, current generation can be calculated by convolving the incident illumination intensity at each wavelength with the wavelength-dependant EQE, where EQE is defined in **(1.5)**, and optical modelling allows calculation only of Q_A, the quantum efficiency of absorption. Multiplication of the modelling result by the IQE, if known, is required to calculate the EQE for current generation calculations. Conversely, if the EQE and Q_A are known, it is possible to work out the IQE of the cell.

This has an application for tandem cells, where, if the IQE of the sub-cells can be determined, modelling can be used to generate current predictions for the sub-cells. The IQE can be estimated using single heterojunction cells with the same architecture as the tandem sub-cells, using the approximation that the IQE of the cell

will not change significantly with position in the optical electric field. This approximation should be valid where the layer thickness is less than or equal to the exciton diffusion length, in which case it will not matter where inside the layer the light is absorbed. If this is not the case, this approximation may no longer be valid, as the position of absorption within the layer becomes significant. Modelling was thus first applied to the single-cell equivalents of the sub-cells of some tandem cells, with the single cells having the following architectures:

Glass / ITO / 5nm MoO_x / 10nm SubPc / 40nm C_{60} / 8nm BCP / Al

Glass / ITO / 5nm MoO_x / 20nm ClAlPc / *d* nm C_{60} / 8nm BCP / Al

With *d* taking values of 15, 20, 25 and 30 nm. The absorptance predictions for the two active layers were summed and compared with EQE measurements to calculate the IQE of the single cells, as shown in **Figure 4.21** for a SubPc / C_{60} single cell and a ClAlPc / C_{60} single cell with *d* = 30nm. Only the layers considered active are taken into account (SubPc, ClAlPc, C_{60}) since light absorbed in other layers is not considered to generate useable excitons / charges. The IQE is estimated by trial-and-error. The IQE is presumed to be roughly constant for a particular layer structure, so a constant factor is used to scale the absorptance prediction. A trial-and-error approach is used to find the 'best-fit' constant factor, which is then taken to be the IQE. This is similar to a recent approach adopted for polymer solar cells by Gilot et al.[111]

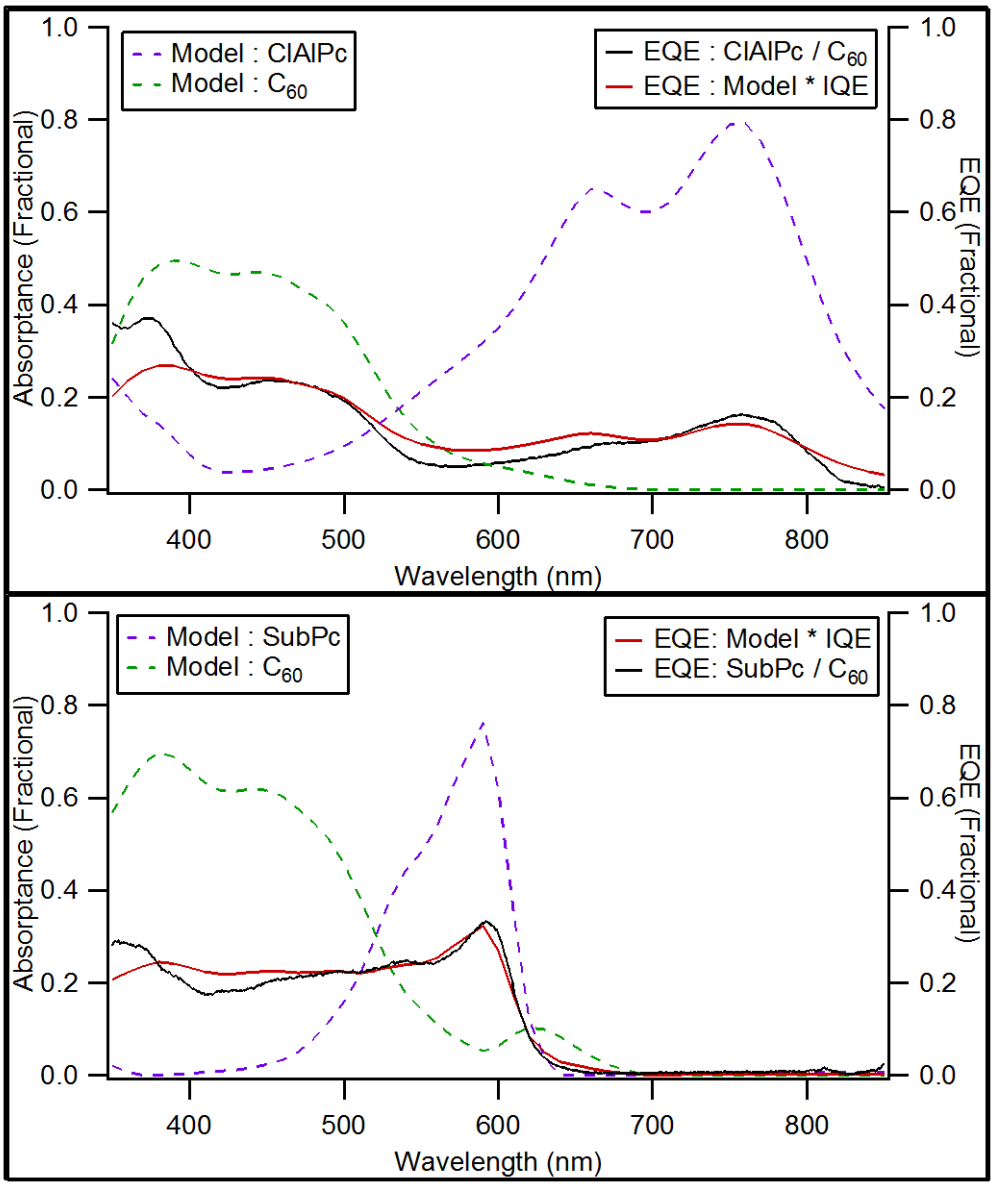

Figure 4.21. Plots of the absorptance in the active layers as predicted by optical modelling, against the EQE of comparable cells. The red lines represent the active layers after scaling by the IQE. Dotted lines indicate an absorptance prediction, while solid lines are EQEs. The legends are placed near the respective axes for the traces they describe.

Estimation of the IQE then allows the model to predict directly the current generation in the sub-cells of a tandem device, which is useful when attempting to optimise the tandem cell through modelling.

Predictions for a short series of tandem cells are given below. This series of cells had the following structure, with *d* taking values of 15, 20, 25 and 30 nm.

Glass / ITO / 5nm MoO_x / 10nm SubPc / 40nm C_{60} / 8nm BCP / 0.2nm Ag / 5nm MoO_x / 20nm ClAlPc / *d* nm C_{60} / 8nm BCP / Al

Absorptance in the front and back cells was calculated via optical modelling then moderated by the IQE calculated from single junction cells of the same thickness, as described. This led to the absorptance predictions of **Figure 4.22**.

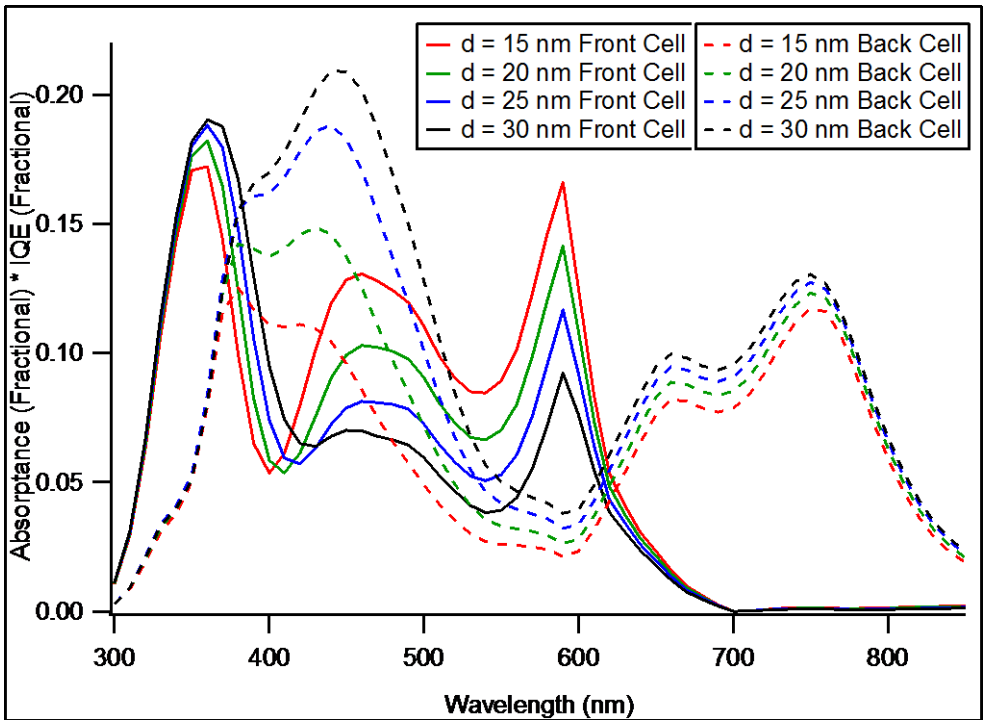

Figure 4.22. Absorptance * IQE predictions for a series of SubPc / C_{60} / ClAlPc / C_{60} tandem cells. Solid lines represent the SubPc / C_{60} front cell and dashed lines the ClAlPc / C_{60} back cell. IQEs are those determined previously.

From these predictions it is clear that while the back cell absorptance increases with thickness *d* of C_{60} in it, the front cell also loses a significant amount of absorptance due to its position in the standing wave shifting. By integrating with the Newport solar simulator lamp spectra (used to provide a better current estimate), current predictions can be obtained. The sum of the output of the two active layers in each sub-cell is taken to constitute the total output of the sub-cell at short circuit. To estimate the current output of the tandem cell, a blunt measure would be to simply take the minimum output of the two relevant sub-cells, however, this is overly pessimistic. Analysis of device operation via a four-terminal tandem cell has shown that when one sub-cell is underperforming the better performing cell will apply a voltage to the under-performer and extract a greater current than if both cells were operating at short-circuit.[112]

Table 4.5. Current predictions from modelling for the tandem cell sub-cells. The overall current output of the tandem cell is then estimated, by matching currents from expected J-V curves.

Device	Front Cell (SubPc / C_{60})	Back Cell (ClAlPc / C_{60})	Tandem (Matched)	J-V Measured
d = 15 nm	1.73	1.80	1.76	2.18
d = 20 nm	1.47	2.15	1.75	2.09
d = 25 nm	0.92	2.51	1.70	1.95
d = 30 nm	0.84	2.77	1.60	1.64

If the J-V curves of the sub-cells are known this can in principle be easily worked out by stating that the voltage drop over the two sub-cells at (overall) short-circuit is equal and opposite, and then increasing this voltage until the current output of each cell is matched.[113] Since the J-V curves are not easily measured in a two-contact

tandem cell, this can instead be approximated utilizing the J-V curves of the single cells imitating the sub-cells under appropriate illumination to match that of the illumination in a tandem architecture.

As can be observed in **Table 4.5**, this actually yields a reasonable estimate for the *d* = 30 nm case, but underestimates for the others, although the correct trend is identified. It is postulated that this is primarily due to inaccuracies in the complex refractive index data, particularly for ClAlPc. Errors in the thickness of the layers may also contribute. Improving the accuracy of the data is the realm of ellipsometry, as discussed in **Section 4.2.1**. Extending the EQE measurements to tandem cells was also pursued, as discussed in **Section** 5, to improve the understanding of the cell's operation. The overall efficiency as measured from the J-V measurements is given in **Table 4.6**.

Table 4.6. Full J-V results from SubPc / C_{60} /ClAlPc /C_{60} architecture cells.

Device	Voc (V)	Jsc ($mAcm^{-2}$)	FF	PCE (%)
d = 15 nm	1.82	2.18	0.53	2.14
d = 20 nm	1.81	2.09	0.58	2.24
d = 25 nm	1.82	1.95	0.57	2.06
d = 30 nm	1.82	1.64	0.57	1.71

Since the performance of the architecture with the SubPc / C_{60} front cell was no better than the performance of the single cells, the architecture was reversed and modelled for comparison. The following architectures were both modelled and subsequently grown:

Glass / ITO / 5nm MoO_x / *d1* nm ClAlPc / *d2* nm C_{60} / 8nm BCP / 0.2nm Ag / 5nm MoO_x / 10nm SubPc / 20nm C_{60}/ 8nm BCP / Al

Where *d1* was the series 6, 10, 16, 20 nm and *d2* was either 8 or 15 nm. The modelling EQE (absorptance multiplied by empirical IQE) predictions are shown in **Figure 4.23** for the *d2* = 8 nm case and **Figure 4.24** for the *d2* = 15 nm case.

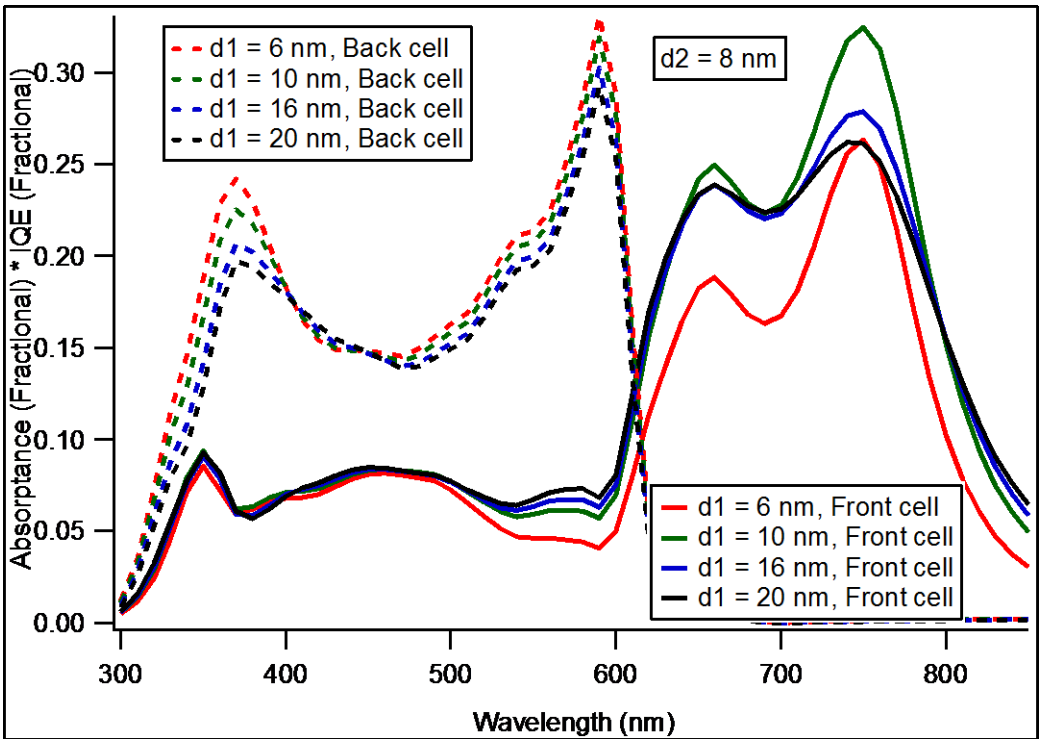

Figure 4.23. Predicted EQE for tandem cells with the ClAlPc / C_{60} being the front cell, with *d2* (front cell C_{60} thickness) equal to 8 nm. IQEs are those determined previously.

Integrating the predicted EQEs with the lamp spectra and current matching of J-V curves lead to the predictions for the current in **Table 4.7**.

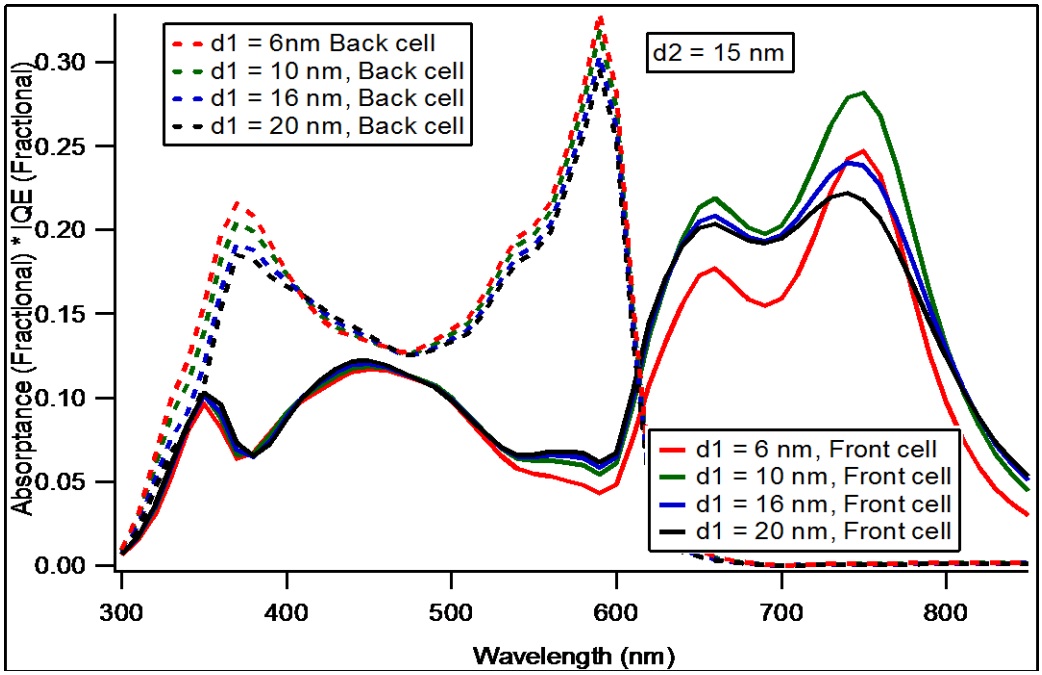

Figure 4.24. Predicted EQE for tandem cells with the ClAlPc / C_{60} being the front cell, with *d2* (front cell C_{60} thickness) equal to 15 nm. IQEs are those determined previously.

Table 4.7. Current predictions generated from the predicted EQE and integrated with the Newport lamp spectra, including predictions from J-V matching via single cell J-V curves to predict the tandem Jsc.

Device		Front Cell (ClAlPc / C_{60})	Back Cell (SubPc / C_{60})	Tandem (Matched)	J-V Measured
d1 = 6 nm	d2 = 8 nm	3.11	2.96	3.02	3.26
d1 = 10 nm		3.98	2.87	3.06	3.44
d1 = 16 nm		3.88	2.75	2.97	3.42
d1 = 20 nm		3.90	2.69	3.05	3.34
d1 = 6 nm	d2 = 15 nm	3.24	2.77	2.96	3.37
d1 = 10 nm		3.81	2.70	2.92	3.38
d1 = 16 nm		3.69	2.61	2.97	3.35
d1 = 20 nm		3.63	2.56	2.91	3.32

However, the predicted improvement in the Jsc as compared to the first architecture is realized in these cells. The modelling also agrees with the J-V measurements in that changing the thickness of the front cell in this case leads to only minor changes in the current output of the cell. The overall performance of these cells therefore shows significant improvement compared to the cells made using the first architecture, as can be seen in **Table 4.8**.

Table 4.8. Full J-V results from the second architecture, showing the improved cell characteristics.

Device		Voc (V)	Jsc ($mAcm^{-2}$)	FF	PCE (%)
d1 = 6 nm	d2 = 8 nm	1.66	3.26	0.52	2.97
d1 = 10 nm		1.72	3.44	0.52	3.23
d1 = 16 nm		1.78	3.42	0.53	3.36
d1 = 20 nm		1.84	3.34	0.52	3.32
d1 = 6 nm	d2 = 15 nm	1.72	3.37	0.52	3.16
d1 = 10 nm		1.71	3.38	0.54	3.26
d1 = 16 nm		1.78	3.35	0.53	3.33
d1 = 20 nm		1.77	3.44	0.53	3.41

4.5. SUMMARY

This chapter first presented variable-angle spectroscopic ellipsometry (VASE) measurements of ClAlPc thin films on quartz substrates. The results obtained were fitted with a combination of Tauc-Lorentz peaks to obtain the complex refractive index of the film. This complex refractive index was then shown to predict with reasonable accuracy the absorption of such a film as measured by UV-vis absorption.

Optical modelling was also discussed in this chapter, and its application for both thin film single cell devices, where it can aid optimisation via the use of spacer layers or architectural modification, and tandem devices, where it has wider application in attempting to optimise the current balancing. Optical modelling was demonstrated to be useful for inverted hybrid single cells based on a SubPc / TiO_x heterojunction, where the architecture was modified to use a spacer layer rather than a thicker donor layer to improve current generation. It was also demonstrated to predict reasonably the absorption in each sub-cell in a tandem device, particularly when current-matching of the predicted sub-cell J-V curves was performed.

Optical modelling is an important capability to have when making tandem cells. The number of parameters available in the construction of tandem cells make complete trial-and-error optimisation inefficient at best. Optical modelling both increases predictive power and gives insight into the behaviour of some structures affected by the standing wave in the optical electric field. In addition, the software and methods used to calculate optical field amplitudes / absorptances / IQEs are also being used by other members of the group for their own single or tandem cell research.

5. EXTERNAL QUANTUM EFFICIENCY MEASUREMENTS

In this chapter the theory behind EQE measurements of tandem cells is presented, both the established protocol for organic tandem cells and an additional proposal to use white light bias measurements to obtain extra information from the technique.

5.1. THEORY

The External Quantum Efficiency technique was developed by E.F.Zalewski and J.Geist in 1980.[114] As previously discussed in **Section 1.5.4**, the overall quantum efficiency can be split into the quantum efficiencies of the individual processes in a solar cell, as described by **(1.5)**, and restated as **(5.1)** below:

$$EQE = Q_A Q_{Diff} Q_{Diss} Q_T \qquad (5.1)$$

However, in tandem cells this simple equation is no longer sufficient. The necessity for current balancing at the recombination zone between the sub-cells leads to the added requirement for the incoming light to be absorbed as equally as possible in both sub-cells of the tandem device, which is potentially not the case. The necessity for current balancing can be understood by considering the energy levels of the tandem cell at short circuit, shown in **Figure 5.1**. For example, consider an electron generated in the SubPc / C_{60} sub-cell; the matching hole can easily reach the anode, but the electron gets stuck at the Ag layer, as it cannot pass through the full HOMO of the ClAlPc without a matching hole in that layer, and it cannot reach the LUMO due to the energy difference. As a result, the current cannot flow through the cell, and charge builds up at the recombination zone until a steady state flat-band is

reached in the cell generating current. A similar process can be described for inorganic tandem cells.

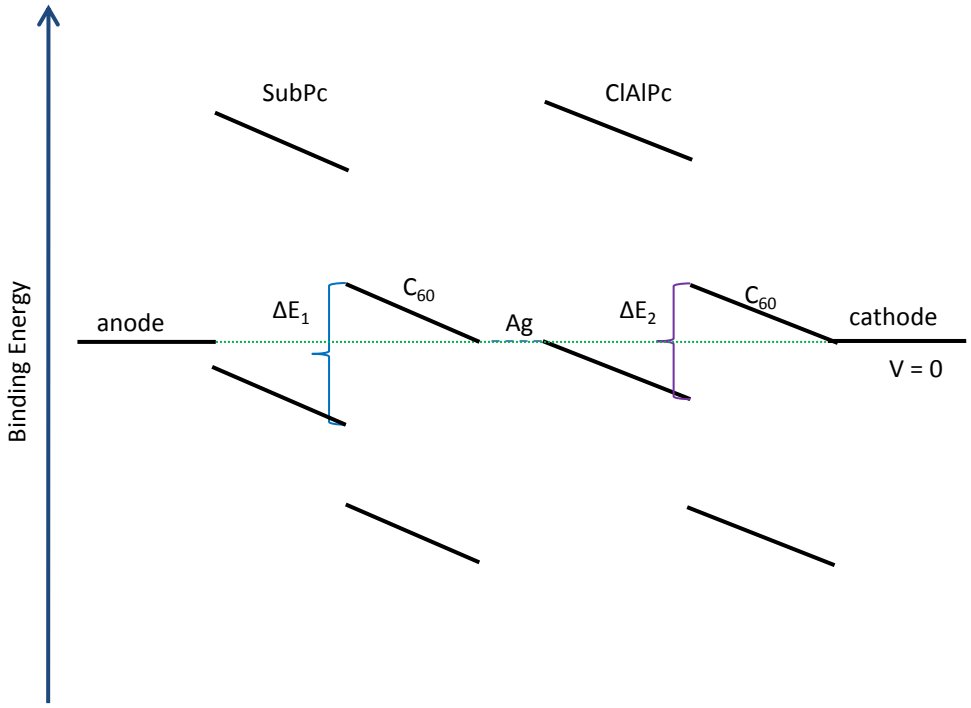

Figure 5.1. Energy level diagram of a tandem cell at short circuit (external voltage = 0). Interfaces are simplified and there is an assumption of no charge build-up at the recombination zone; the bands are sloped due to the internal field(s).

An example of the actual expected EQE in tandem cells can be found in the work of Burdick et al, who used a tandem cell composed of two sub-cells of amorphous silicon.[115] When only a monochromatic probe light is used, it is expected that the external quantum efficiency at each wavelength will result from the minimum quantum efficiency of the sub-cells including the effects of optical interference on Q_A. A prediction for this with a SubPc / C_{60} / ClAlPc / C_{60} tandem cell is shown below in **Figure 5.2**, based on single cell SubPc / C_{60} and ClAlPc / C_{60} EQE measurements. From this it can be seen that the actual measured EQE has the same approximate shape as the crossover of the two single cell EQEs, but still has significant differences. There are two primary reasons for this to be the case; firstly,

the positioning of the sub-cell in the optical electrical field in a tandem device is different to that in a single cell, resulting in a different absorption profile. This is different to inorganic solar cells, where the sub-cells are thick enough and conductive enough that the effect of such a shift is minimal.

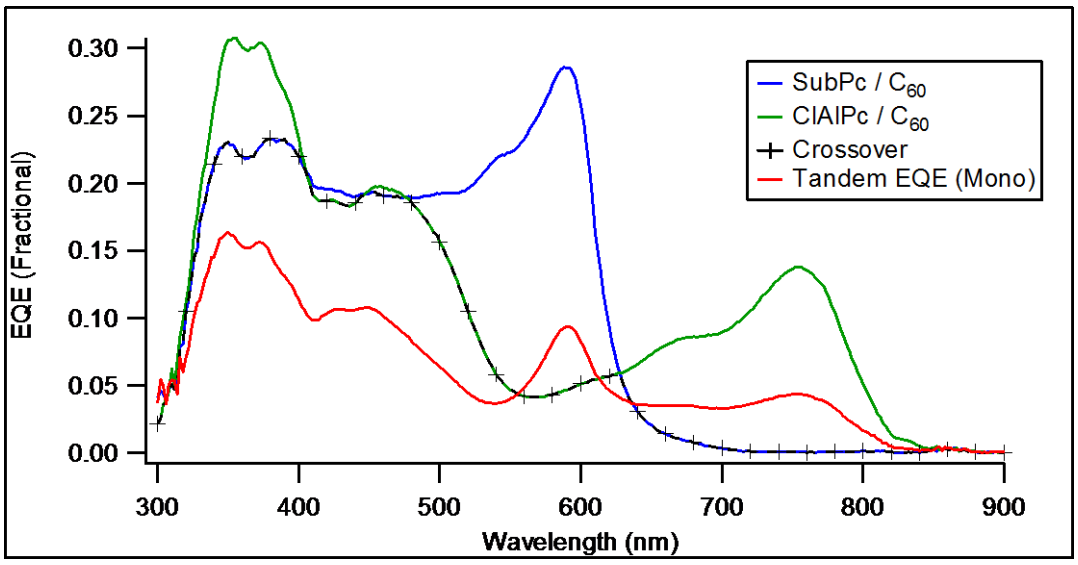

Figure 5.2. Comparison of the single cell EQEs with the tandem cell EQE (monochromatic probe light only). The crosses represent the expected tandem cell EQE based solely on single cell EQE and current balancing.

The second reason is that in organic solar cells the J-V curve under reverse bias is rarely completely flat, as can be seen in **Figure 5.3**. Even under monochromatic bias when only one cell is absorbing it is possible to observe a current. This can be observed above ~650 nm in **Figure 5.2**, and is due to the 'working' sub-cell applying a reverse bias across the second sub-cell and forcing a reduced but detectable current through. This makes accurate EQE measurements of tandem cells using only monochromatic light impossible.

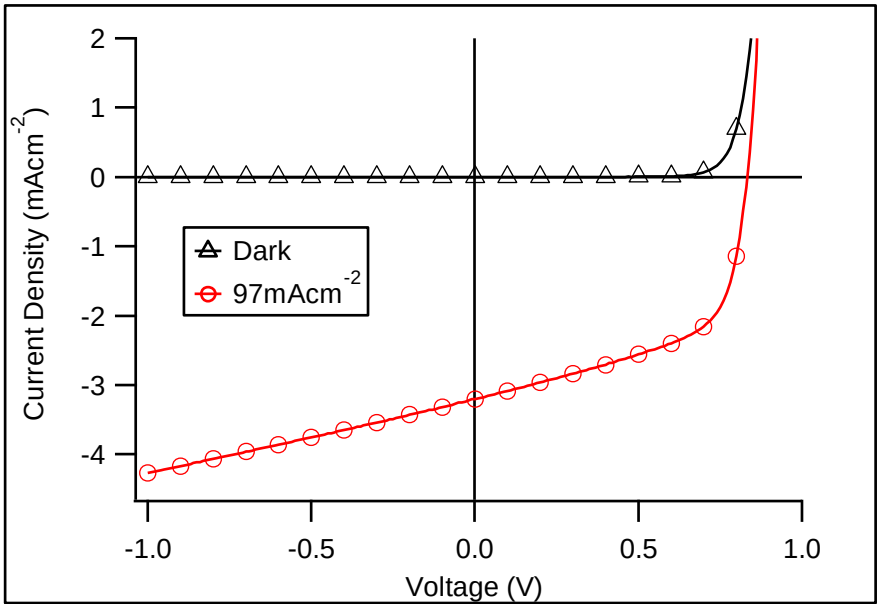

Figure 5.3.Light and dark J-V curves for an example ClAlPc/ C_{60} cell showing the leakiness of the cell under reverse bias. As can be seen, this is also illumination dependant, presumably due to the photoconductivity of the organic materials.

However, as outlined by Burdick et al, it is possible to measure the sub-cell EQEs in a tandem architecture without an accessible intermediate contact with the use of an optical bias illumination. The principle here is to flood one, and only one, of the sub-cells with illumination, so that one sub-cell is producing a large excess of current. The monochromatic probe light will then only show up when it is absorbed in the second, unbiased sub-cell. This allows the EQE of the unbiased sub-cell to be measured. For a truly accurate measure of the sub-cell EQE, however, a few additional corrections must be made. These corrections are proposed in a paper by Gilot et al,[111] and consist of a correction for the voltage bias generated by the optically biased sub-cell and a potential correction for the sub-linear light intensity dependence of current generation in the cell under test. This second correction will be noticeable when the sub-cell under test cannot be illuminated with floodlight representative of AM1.5G. The magnitude of the electrical bias can be determined

by comparing the curves of the equivalent single cells at the specific illumination expected in the tandem sub-cell.

5.2. EXPERIMENTAL

A Xenon arc lamp solar simulator (Sciencetech SF150) is used as a light source in conjunction with a monochromator to provide monochromatic light; this light is mechanically chopped at approximately 520 Hz. The monochromatic light is measured by use of a calibrated photodiode, model 818-UV from Newport, to account for the spectrum of the light source when making measurements. The output from either the photodiode or a device under test is fed to a FEMTO DHPCA-100 current amplifier (used as a pre-amplifier) and then to a Stanford Instruments SR830DSP Lock-In amplifier, which uses the exact frequency from the chopper to 'lock-in' to the signal. The Lock-In Amplifier interfaces to a computer, where a LabView program performs analysis.

Light-biased measurements were performed using either a high-powered LED or the Newport-Oriel solar simulator described in **Section 2.6**. Red light bias illumination was provided by a Thorlabs M780L2, "deep red" LED, and green light bias illumination by a Thorlabs M530L2, "green" LED. A schematic of the setup for light biasing is shown in **Figure 5.4**. Bias voltage to the sample under EQE was provided by the FEMTO DHPCA-100 current amplifier.

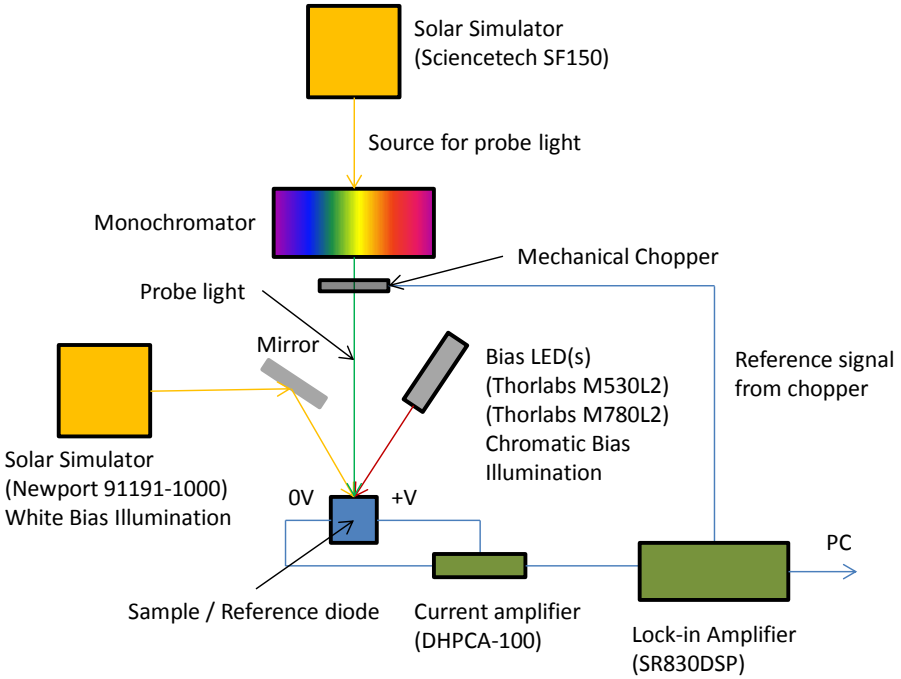

Figure 5.4. Schematic of the setup for light bias measurements. The incident angles of the light from the bias LEDs and Newport simulator are exaggerated for the sake of compactness; the actual incident angles are smaller (~20°).

5.3. RESULTS

5.3.1. WHITE LIGHT BIAS EQE

The current matching situation in a tandem cell becomes more interesting when white light bias illumination is used. White light here is defined as light which is either equal or an approximation to the AM1.5G standard to minimize spectral mismatch.[52] In an extension of the argument for monochromatic bias illumination, only the cell currently under-performing should respond to the probe illumination, as the over-performing cell will by definition be generating an excess of current. As a result the EQE should give a direct indication of which sub-cell requires further improvement in order to improve the overall power conversion efficiency; this is

achieved by observing where the white light bias trace shows more or less response than expected.

The following series of small molecule tandem cells were grown to probe the changes in white light bias *EQE* with cell balancing, with the thickness of the C_{60} layer in the second sub-cell (*d*) varied between 15 nm and 30 nm in 5 nm increments:

Glass / ITO / 5 nm MoO_x / 10 nm SubPc / 20 nm C_{60} / 8 nm BCP / 0.2 nm Ag / 5 nm MoO_x / 20 nm ClAlPc / *d* nm C_{60} / 8 nm BCP / Al

This series was chosen based on optical modelling which suggested a change in the current-limiting sub-cell should occur across the series. The cells were not optimised to produce the best possible *PCEs*, but rather to provide a systematic study for the *EQE* measurements that could then be related to *J-V* measurements under 1 sun illumination. The modelling predicted that the SubPc sub-cell would dominate initially at smaller values of *d*, with the ClAlPc sub-cell beginning to dominate as *d* was increased. **Figure 5.5** shows the absorption spectra of the active materials used in the two sub-cells, along with the emission spectra of the two LEDs used for red and green light biasing. The LEDs were chosen such that each excites one sub-cell with little absorption in the other; the 530 nm green bias is intended to primarily excite the SubPc sub-cell, and the 780 nm red bias to excite the ClAlPc sub-cell.

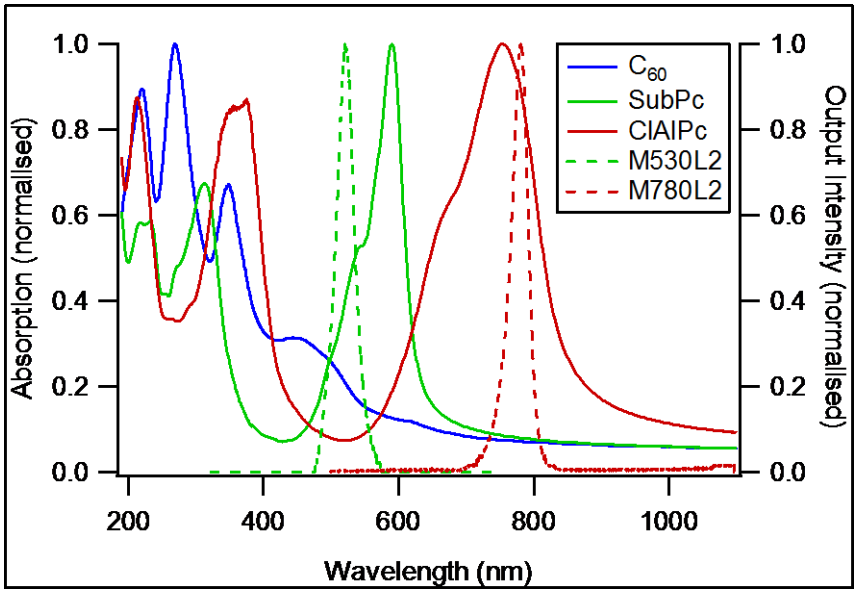

Figure 5.5. Normalised absorption spectra of the active materials, together with the normalised output intensity of the two diodes used for light bias measurements.

As shown in **Figure 5.6**, which uses the d = 15 nm cell as an example, both sub-cells can be observed to generate some current when no bias light is applied. Part of this current can be explained by overlap in absorption between sub-cells, particularly in the 300-600 nm region, as can be determined from **Figure 5.5**.

The other part of the current, and that observed over 600 nm, is likely due to the leaky nature of OPVs under bias, allowing the cell probed by the monochromatic light to force a small current through the second cell.[112] Applying a red bias light (780 nm) results in the SubPc / C_{60} sub-cell appearing in the *EQE* due to the ClAlPc/C_{60} sub-cell generating excess current, while applying a green bias light (530 nm) results in the ClAlPc / C_{60} sub-cell appearing since the SubPc / C_{60} sub-cell generates excess current.

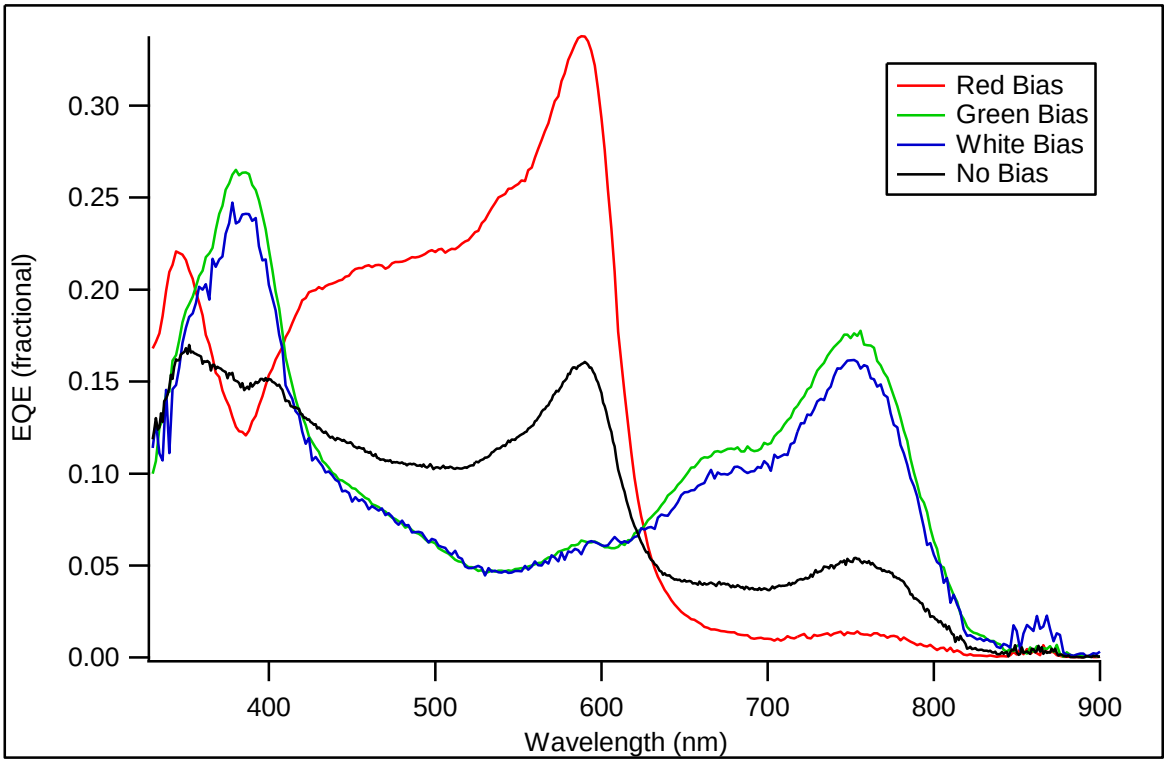

Figure 5.6. EQE of cell with *d* = 15 nm while illuminated with various bias lights.

It is expected that applying a white light bias is just an extension of this balancing argument. The sub-cell which generates the most current under white light bias will not appear in the *EQE* spectra as the additional monochromatic probe light will only further saturate the sub-cell, again showing up the under-performing sub-cell. This can be seen in **Figure 5.6**, which compares the *EQE* response under different bias illuminations for the *d* = 15 nm cell. The white light bias in this cell is shown to be almost equivalent to illuminating with the green bias LED, suggesting that the ClAlPc / C_{60} sub-cell is current limiting.

By contrast, if the current is perfectly balanced with no charge built-up at the interface, the cell is expected to behave as if it were unbiased. To compare the series of cells directly, the ratio of the difference between white light and no bias cases with the no bias case was calculated, via equation **(5.2)**.

$$WBD = \frac{(White\ bias\ EQE - \ Dark\ EQE)}{Dark\ EQE} \tag{5.2}$$

By subtracting the no-bias case as a reference in this way the best-optimised cell would be expected to follow the zero line, i.e. with no difference between the light bias and no-bias traces.

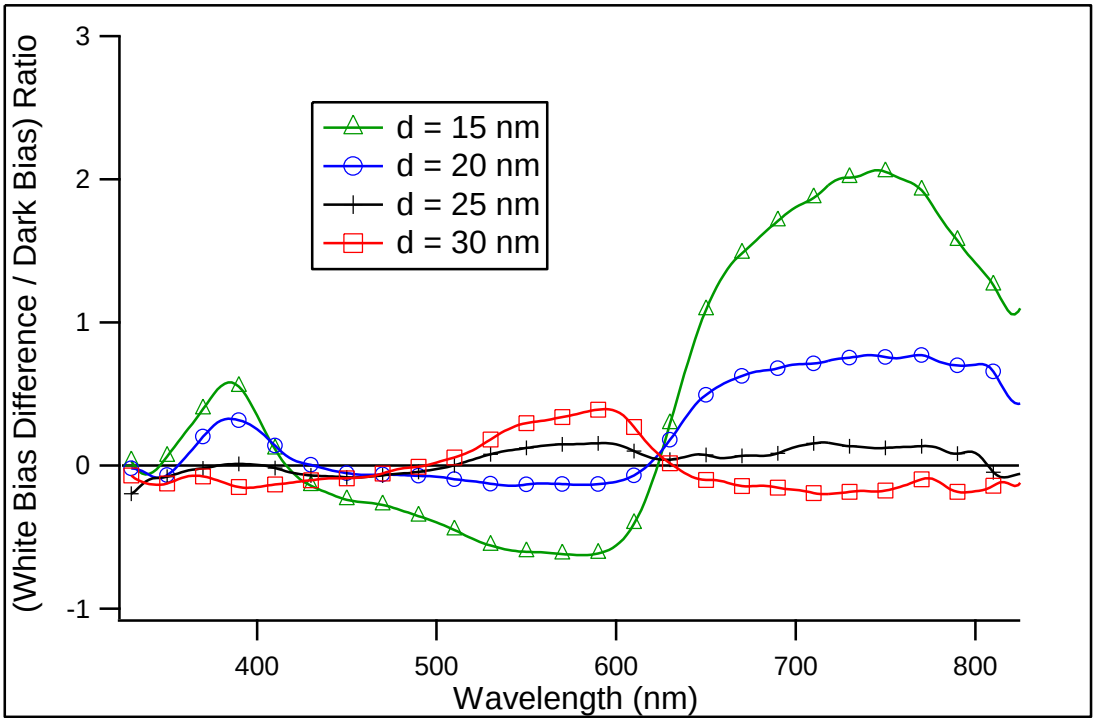

Figure 5.7 – Comparing the difference between the white light bias and the dark EQE traces. The difference divided by the dark value was used rather than absolute values to give a better comparison of the curves.

This analysis is shown in **Figure 5.7**, where it can be seen that the *d* = 15 nm tandem cell clearly shows less response from the SubPc / C_{60} sub-cell and a stronger response from the ClAlPc / C_{60} sub-cell than in the no bias condition. For *d* = 20 nm

this deviation is reduced in both regions, and for d = 25 nm the device shows even less deviation, which should indicate that this tandem cell is better optimised. In the d = 30 nm cell, the deviation reverses, with the ClAlPc / C_{60} sub-cell showing less response and the SubPc / C_{60} showing a stronger response than in the no bias case. This inversion implies that an optimisation point has been passed, and from the observed deviations the d = 25 nm cell is expected to be the closest to this optimum point. The observed minor positive deviation for the d = 25 nm cell may be due to the increased leakage current observed in similar single cells under illumination as compared to in the dark; this can be observed in **Figure 5.3**.

Comparing this to the estimates for the sub-cell short-circuit currents (J_{SC}) from regular light bias *EQE*, as in **Table 5.1**, the same trend is observed. The d = 15 nm cell is predicted to be strongly limited by the ClAlPc / C_{60} sub-cell, with the d = 20 nm still limited by this cell but to a lesser degree. The d = 25 nm cell is predicted to be quite well balanced with the d = 30 nm cell limited instead by the SubPc / C_{60} sub-cell.

Table 5.1. Comparison of sub-cell EQE estimations from voltage-corrected light biased EQE measurements integrated with the solar simulator lamp spectra, with thickness (d) of C_{60} in the ClAlPc / C_{60} sub-cell.

d [nm]	ClAlPc / C_{60} [mA /cm^2]	SubPc / C_{60} [mA /cm^2]	Difference [mA /cm^2]
15	2.43	3.13	0.69
20	2.61	2.80	0.18
25	2.82	2.78	-0.03
30	2.43	2.08	-0.35

The J-V curves obtained for these devices are given in **Figure 5.8**. The statistics of the cells are tabulated in **Table 5.2.**

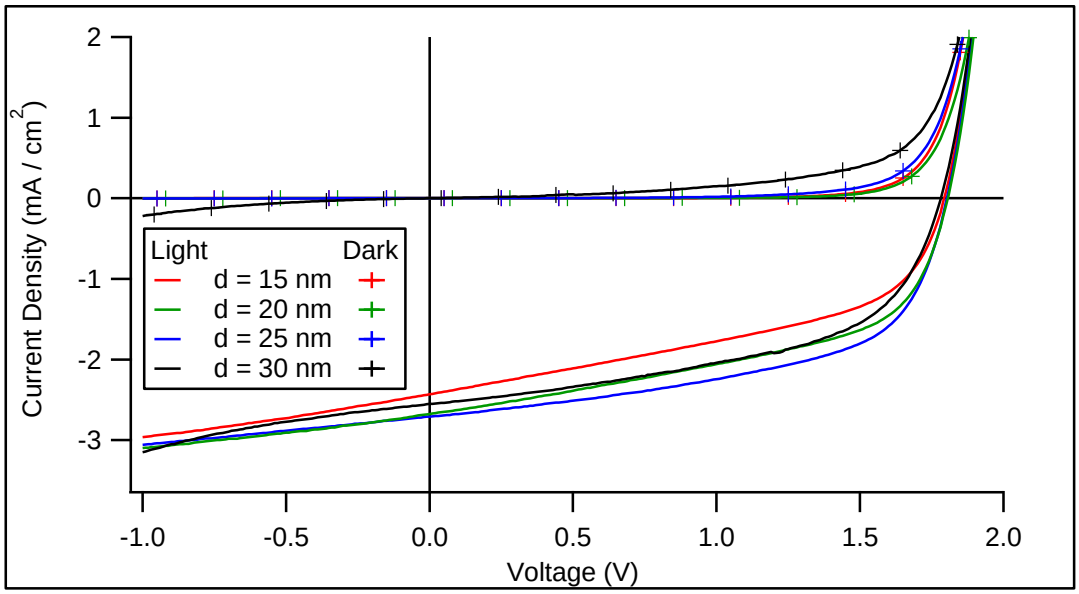

Figure 5.8. J-V curves for the devices. The slight shift in Jsc and the change in fill factor can be seen clearly.

Table 5.2. Comparison of results of IV measurements for the series of cells with varying C_{60} thickness in the ClAlPc / C_{60} sub-cell.

d (nm)	Voc (V)	Jsc (mA/cm^2)	FF	PCE (%)
15	1.79	2.43	0.47	1.98
20	1.81	2.68	0.51	2.39
25	1.81	2.71	0.56	2.64
30	1.78	2.55	0.53	2.32

Comparing the measured efficiencies under 1 sun illumination using *J-V* measurements, the prediction for the *d* = 25 nm cell to be the best optimised cell is supported. The *d* = 25 nm cell is shown to give the highest J_{SC} of the series, while the *d* = 15 nm cell, which is clearly predicted to be the most poorly balanced from

Figure 5.7, is shown to demonstrate the worst *J-V* characteristics. It should be noted that this technique will optimise based on the spectrum of the white light used, and it is thus important for solar cells that the best approximation to AM1.5G is made.

5.3.2. SUPPLEMENTARY DATA

Application of this method to the dataset presented in **Section 4.4** confirms the conclusions arrived at in that section.

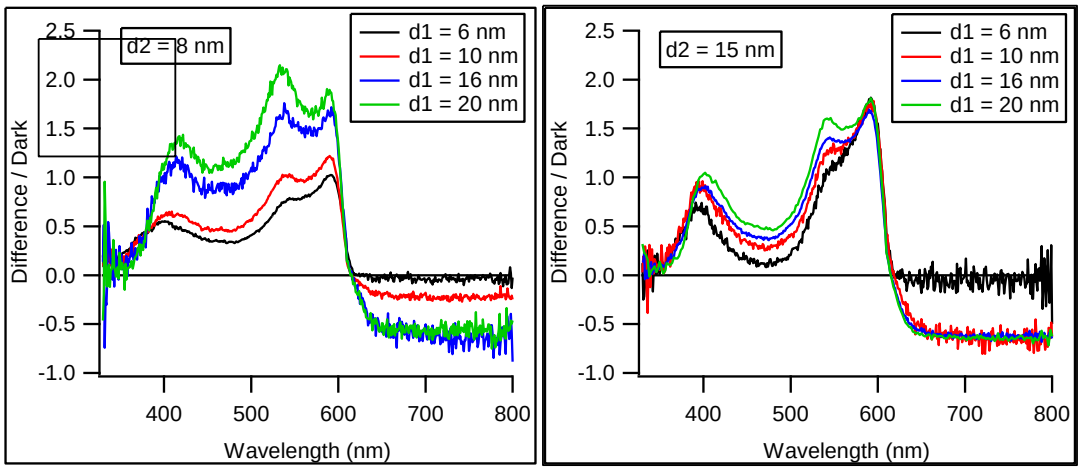

Figure 5.9. Difference traces for the devices from **Section 4.4**. All traces show that the SubPc / C_{60} sub-cell is limiting, to a greater or lesser degree.

The bias difference traces are given in **Figure 5.9**; as can be seen by comparing these traces with the sub-cell difference predictions in **Table 5.3**, these results are in good agreement, at least qualitatively. As predicted, the d1 = 6 nm, d2 = 8 nm device is the only device close to achieving a balance between the sub-cells, although as previously noted this is overshadowed by the voltage biasing effect of the ClAlPc sub-cell when considering the actual current extracted.

Table 5.3. Model predictions for this set of cells, with the difference calculated.

Device		Front Cell (ClAlPc / C_{60})	Back Cell (SubPc / C_{60})	Difference [mA /cm^2]
d1 = 6 nm	d2 = 8 nm	3.11	2.96	0.15
d1 = 10 nm		3.98	2.87	1.11
d1 = 16 nm		3.88	2.75	1.13
d1 = 20 nm		3.90	2.69	1.21
d1 = 6 nm	d2 = 15 nm	3.24	2.77	0.47
d1 = 10 nm		3.81	2.70	1.11
d1 = 16 nm		3.69	2.61	1.08
d1 = 20 nm		3.63	2.56	1.06

5.4. SUMMARY

It is possible to use EQE measurements of tandem cells in simulated AM1.5G white light bias conditions to infer directly which of the sub-cells of the tandem cell is current-limiting, as demonstrated in this particular case where the best optimised cell was predicted using white light bias EQE measurements then confirmed by J-V measurements. This would be a convenient method to determine the state of current balancing in a device without relying on complicated analysis. The results from this measurement would then enable further optimisation by directing attention on the underperforming cell. This technique can be applied to tandem cells based on a range of different materials systems, provided the sub-cells are at least partially spectrally distinct.

6. CONCLUSIONS

This thesis has investigated the use of multijunction device architectures to improve the efficiency of organic molecular photovoltaics. Several areas have been covered:

- Use and design of the recombination zone
- Use and application of optical modelling for thin film photovoltaics
- Ellipsometric measurements to obtain complex refractive index data.
- Application of EQE to tandem cells, and additional techniques to extract further data from such measurements.

6.1. RECOMBINATION ZONE

Use of ultrathin layers of silver between 0.4 nm and 4 nm at a growth rate of 0.005 nms^{-1} was shown to provide recombination centres for charges at the interface of the two sub-cells; the presence of nanoparticles rather than a complete film of silver was confirmed by SEM. The silver nanoparticles improved the cell performance significantly compared to the reference devices lacking silver nanoparticles; open-circuit voltage improved in one case from 1.34 V to 1.80 V, while short-circuit current improved from 2.89 $mAcm^{-2}$ to 3.39 $mAcm^{-2}$, with an additional boost to the fill factor from 0.27 to 0.47, contributing to a total efficiency improvement from 1.10% to 2.99%, and an improvement over the best single cell result of 2.26%. This demonstrated the material system combines well into a multijunction cell, giving a relatively high open circuit voltage that is close to the sum of the sub-cell voltages, without losing a significant amount of current generation, and providing a clear advantage in efficiency over the single heterojunction configuration.

6.2. OPTICAL MODELLING

Ellipsometry measurements of thin films of ClAlPc were presented and analysed to measure the complex refractive index for optical modelling. Several films of different thicknesses were measured with Variable Angle Spectroscopic Ellipsometry (VASE). The results from the measurements were then fitted with a combination of four Tauc-Lorentz dispersion functions, and verified utilizing optical modelling to compare the predicted absorption from refractive index to UV-vis absorption spectra.

Optical electric field modelling was discussed in the context of solar cells, and used to explain and improve some device architectures in hybrid TiOx / SubPc solar cells; by using the spacer layer predicted in optical modelling rather than making the donor layer thicker the overall efficiency was improved from 0.28% to 0.58%. This was due to the improvement in quantum efficiency gained by using the thinner donor layer, while utilizing optical spacing to shift the donor layer towards a peak in the optical electric field to boost absorption.

Optical modelling was also applied to tandem cells, where it provided useful current estimates for the sub-cells. This is an aid in attempting to optimise the tandem device; quantitative measures of the current generation were shown to be possible if the IQE of the sub-cell is known or can be estimated. The use of optical modelling to specify the short-circuit current of the sub-cells allowed J-V curves from single cells adjusted for light intensity to predict the current generation of the tandem cell when including the effect of current-matching between the two sub-cells; this demonstrated that the short-circuit current of the tandem cell is not simply limited to that of the weakest sub-cell.

6.3. EXTERNAL QUANTUM EFFICIENCY

Tandem solar cell measurement by external quantum efficiency (EQE) was both discussed and demonstrated, covering the inadequacy of standard EQE techniques when measuring series multijunction cells. The use of bias light and corrective voltage was discussed and EQE of tandem cells in varying bias illumination conditions shown. An extension to the existing protocols was proposed that allows EQE measurements to make a qualitative assessment of the current balancing in a tandem cell under 'white' (AM1.5G, or other target spectrum) light conditions. This is a completely independent measure of current balancing that does not rely on accurate optical modelling; the correlation between the balancing conditions obtained via this method and optical modelling is demonstrated in two distinct data sets.

6.4. FURTHER WORK

There are multiple avenues available for pursuit as a result of this work; in particular, the development of a second acceptor material that could be used alongside C_{60} to further widen the absorption of the tandem cell and enhance current generation. Certain materials may also have the potential to further improve the open-circuit voltage of a tandem device if their energy levels are suitable. A replacement for the Bathocuproine (BCP) used in this work might also lead to more efficient recombination layers, as this material is generally insulating. The development of a suitable optical spacer for vacuum-deposition would have potential to boost cell efficiencies in combination with the optical modelling approach. The use of bulk heterojunction layers might also be considered to improve current generation in the tandem device, as they have shown promise in single cells.

Extending the tandem cell concept further may also be a route to improvement; in inorganic cells triple heterojunction devices are utilized to attain very high PCEs. The addition of a third heterojunction with a lower V_{oc} that absorbed in the near infrared would potentially boost efficiencies by up to half. There has been recent work in the area of vacuum-deposited organic tandem cells carried out by Heliatek which has resulted in a certified PCE of 9.8% with a 1.1 cm^2 area, demonstrating the potential for this kind of photovoltaics.[116]

For optical modelling, the addition of a diffusion model for exciton generation would be a logical step to reduce potential error in the calculation of the IQE of a device, and for better comparison of films that are of significant thickness compared to the diffusion length of excitons. Such models have been demonstrated in the literature and would improve the predictive power of the modelling.[117]

The newly developed EQE protocol could also potentially be extended to obtain further information on a tandem cell under operation; in particular it may be possible to quantify the bias voltage at the interface. This would allow construction of the J-V curves of each sub-cell without an intermediate contact. It may also prove to be useful in the case of three or more heterojunctions, if the material combination is suitable for identifying sub-cells from the EQE traces, as it does not require the use of multiple bias illuminations.

7. REFERENCES

*[1] BP in BP Energy Outlook 2030, Vol. BP, http://www.bp.com, **2011**.*

*[2] BP in BP Statistical Energy Review 2011, Vol. BP, http://www.bp.com, **2011**.*

*[3] S. Solomon, D. Qin, M. Manning, Z. Chen, M. Marquis, K. B. Averyt, T. M. and M. H.L in Climate Change 2007: The Physical Science Basis, Vol. Intergovernmental Panel on Climate Change, Cambridge University Press, **2007**, p. 996.*

*[4] J. Nelson, The Physics of Solar Cells, Imperial College Press, London, **2003**, p. 363.*

*[5] NREL in Concentrating Solar Power Research, Vol. US Department of Energy, **2010**.*

*[6] R. Ohl in light-sensitive electric devices, Vol. 2402662 (Ed. U. S. P. Office), United States, **1946**.*

*[7] J. H. Zhao, A. H. Wang, M. A. Green and F. Ferrazza, Applied Physics Letters **1998**, 73, 1991-1993.*

*[8] M. A. Green, K. Emery, Y. Hishikawa and W. Warta, **2011**, 19, 92.*

*[9] S. Naseem and T. J. Coutts, Journal of Applied Physics **1985**, 58, 4463-4464.*

*[10] R. H. Bube, A. L. Fahrenbruch, R. Sinclair, T. C. Anthony, C. Fortmann, W. Huber, C. T. Lee, T. Thorpe and T. Yamashita, Ieee Transactions on Electron Devices **1984**, 31, 528-538.*

*[11] S. Wojtczuk, P. Chiu, X. B. Zhang, D. Derkacs, C. Harris, D. Pulver, M. Timmons and Ieee, 35th IEEE Photovoltaic Specialists Conference (Honolulu, HI) **2010**, pp. 1259-1264.*

*[12] S. Schumann, R. Da Campo, B. Illy, A. C. Cruickshank, M. A. McLachlan, M. P. Ryan, D. J. Riley, D. W. McComb and T. S. Jones, Journal of Materials Chemistry **2011**, 21, 2381-2386.*

*[13] M. D. McGehee and C. Goh, Short Course on Physics of Sustainable Energy (Univ Calif Berkeley, Berkeley, CA) **2008**, pp. 322-330; J. Kalowekamo and E. Baker, Solar Energy **2009**, 83, 1224-1231.*

*[14] B. O'Regan and M. Gratzel, Nature **1991**, 353, 737-740.*

*[15] M. Gratzel and K. Kalyanasundaram, Current Science **1994**, 66, 706-714.*

*[16] M. K. Nazeeruddin, F. De Angelis, S. Fantacci, A. Selloni, G. Viscardi, P. Liska, S. Ito, T. Bessho and M. Gratzel, Journal of the American Chemical Society **2005**, 127, 16835-16847.*

*[17] G. A. Chamberlain, Solar Cells **1983**, 8, 47-83.*

*[18] C. W. Tang, Applied Physics Letters **1986**, 48, 183-185.*

*[19] D. Wynands, M. Levichkova, K. Leo, C. Uhrich, G. Schwartz, D. Hildebrandt, M. Pfeiffer and M. Riede, Applied Physics Letters **2010**, 97, 3.*

*[20] G. Yu, J. Gao, J. C. Hummelen, F. Wudl and A. J. Heeger, Science **1995**, 270, 1789-1791.*

*[21] Y. Liang, Z. Xu, J. Xia, S.-T. Tsai, Y. Wu, G. Li, C. Ray and L. Yu, Advanced Materials **2010**, 22, E135-+.*

*[22] S. Schumann, S. A. F. Bon, R. A. Hatton and T. S. Jones, Chemical Communications **2009**, 6478-6480.*

*[23] M. Hiramoto, M. Suezaki and M. Yokoyama, Chemistry Letters **1990**, 3, 327-330.*

*[24] J. G. Xue, S. Uchida, B. P. Rand and S. R. Forrest, Applied Physics Letters **2004**, 85, 5757-5759.*

*[25] C. L. Uhrich, G. Schwartz, B. Maennig, W. M. Gnehr, S. Sonntag, O. Erfurth, E. Wollrab, K. Walzer, J. Foerster, A. Weiss, O. Tsaryova, K. Leo, M. K. Riede and M. Pfeiffer in Efficient and long-term stable organic vacuum deposited tandem solar cells, Vol. 7722 Eds.: P. L. Heremans, R. Coehoorn and C. Adachi), Spie-Int Soc Optical Engineering, Bellingham, **2010**; B. Maennig, J. Drechsel, D. Gebeyehu, P. Simon, F. Kozlowski, A. Werner, F. Li, S. Grundmann, S. Sonntag, M. Koch, K. Leo, M. Pfeiffer, H. Hoppe, D. Meissner, N. S. Sariciftci, I. Riedel, V. Dyakonov and J. Parisi, Applied Physics a-Materials Science & Processing **2004**, 79, 1-14; J. Drechsel, B. Mannig, F. Kozlowski, M. Pfeiffer, K. Leo and H. Hoppe, Applied Physics Letters **2005**, 86, 244102.*

*[26] K. Triyana, T. Yasuda, K. Fujita and T. Tsutsui, Thin Solid Films **2005**, 477, 198-202; K. Triyana, T. Yasuda, K. Fujita and T. Tsutsui, Japanese Journal of Applied Physics **2011**, 43, 2352.*
*[27] D. Cheyns, B. Rand and P. Heremans, Applied Physics Letters **2010**, 97, 033301.*
*[28] K. Kawano, N. Ito, T. Nishimori and J. Sakai, Applied Physics Letters **2006**, 88, 3.*
*[29] G. Dennler, H. J. Prall, R. Koeppe, M. Egginger, R. Autengruber and N. S. Sariciftci, Applied Physics Letters **2006**, 89, 073502.*
*[30] A. Colsmann, J. Junge, C. Kayser and U. Lemmer, Applied Physics Letters **2006**, 89, 203506.*
*[31] A. G. F. Janssen, T. Riedl, S. Hamwi, H. H. Johannes and W. Kowalsky, Applied Physics Letters **2007**, 91, 073519.*
*[32] A. Hadipour, B. de Boer and P. W. M. Blom, JOURNAL OF APPLIED PHYSICS **2007**, 102, 074506-074506.*
*[33] J. Gilot, M. Wienk and R. Janssen, Applied Physics Letters **2007**, 90, 143512.*
*[34] J. Kim, K. Lee, N. Coates, D. Moses, T. Nguyen, M. Dante and A. Heeger, Science **2007**, 317, 222.*
*[35] M. Skompska, Synthetic Metals **2010**, 160, 1-15; P. Gomez-Romero, Advanced Materials **2001**, 13, 163-174.*
*[36] X. Chen and S. S. Mao, Chemical Reviews **2007**, 107, 2891-2959; J. Boucle, S. Chyla, M. S. P. Shaffer, J. R. Durrant, D. D. C. Bradley and J. Nelson, Advanced Functional Materials **2008**, 18, 622-633.*
*[37] A. Einstein, Annalen der Physik **1905**, 17, 132-148.*
*[38] H. P. Myers, Introductory Solid State Physics, Second Edition, Taylor & Francis, **1997**, p. 536.*
*[39] L. M. Sander, Advanced Condensed Matter Physics, Cambridge University Press, **2009**, p. 286.*
*[40] B. A. Gregg and M. C. Hanna, Journal of Applied Physics **2003**, 93, 3605-3614.*
*[41] M. Pope and C. E. Swenberg, Electronic processes in organic crystals and polymers, Oxford University Press, **1999**, p. 1328.*
*[42] G. H. Wannier, Physical Review **1937**, 52, 191.*
*[43] T. Stubinger and W. Brutting, Journal of Applied Physics **2001**, 90, 3632-3641.*
*[44] H. Ishii, K. Sugiyama, E. Ito and K. Seki, Advanced Materials **1999**, 11, 605+.*
*[45] I. Hancox, K. V. Chauhan, P. Sullivan, R. A. Hatton, A. Moshar, C. P. A. Mulcahy and T. S. Jones, Energy & Environmental Science **2010**, 3, 107-110.*
*[46] M. Pfeiffer, K. Leo, X. Zhou, J. S. Huang, M. Hofmann, A. Werner and J. Blochwitz-Nimoth, Organic Electronics **2003**, 4, 89-103.*
*[47] D. Cheyns, J. Poortmans, P. Heremans, C. Deibel, S. Verlaak, B. P. Rand and J. Genoe, Physical Review B **2008**, 77, 165332.*
*[48] M. Planck, Annalen der Physik **1901**, 5, 553 ff.*
*[49] A. S. f. T. a. Materials, Laboratory Apparatus; Degradation of Materials; SI; Oxygen Fire Safety, Astm International, **2012**, p. 956.*
*[50] NREL in Reference Solar Spectral Irradiance: Air Mass 1.5, Vol. 2011 **2003**.*
*[51] K. A. Emery and C. R. Osterwald, Solar Cells **1986**, 17, 253-274.*
*[52] V. Shrotriya, G. Li, Y. Yao, T. Moriarty, K. Emery and Y. Yang, Advanced Functional Materials **2006**, 16, 2016-2023.*
*[53] H. de Diesbach and E. von der Weid, Helvetica Chimica Acta **1927**, 10, 886-888.*
*[54] G. Chaidogiannos, F. Petraki, N. Glezos, S. Kennou and S. Nespurek, Applied Physics a-Materials Science & Processing **2009**, 96, 763-767.*
*[55] H. Peisert, M. Knupfer, T. Schwieger, G. G. Fuentes, D. Olligs, J. Fink and T. Schmidt, Journal of Applied Physics **2003**, 93, 9683-9692.*

*[56] M. An, S. Kim and J. D. Hong, Bulletin of the Korean Chemical Society **2010**, 31, 3272-3278; L. Zhang, Q.-F. Xu, J.-M. Lu and S.-C. Yao, Guang pu xue yu guang pu fen xi = Guang pu **2007**, 27, 773-776; M. V. Martinez-Diaz, M. Ince and T. Torres, Monatshefte Fur Chemie **2011**, 142, 699-707.*

*[57] R. R. Mather, Journal of Porphyrins and Phthalocyanines **1999**, 3, 643-646.*

*[58] R. D. Gould, Coordination Chemistry Reviews **1996**, 156, 237-274.*

*[59] M. E. AzimAraghi and A. Krier, Pure and Applied Optics **1997**, 6, 443-453.*

*[60] P. Sullivan, T. S. Jones, A. J. Ferguson and S. Heutz, Applied Physics Letters **2007**, 91, 233114; K. V. Chauhan, P. Sullivan, J. L. Yang and T. S. Jones, Journal of Physical Chemistry C **2010**, 114, 3304-3308.*

*[61] S. W. Cho, L. F. J. Piper, A. DeMasi, A. R. H. Preston, K. E. Smith, K. V. Chauhan, P. Sullivan, R. A. Hatton and T. S. Jones, Journal of Physical Chemistry C **2010**, 114, 1928-1933.*

*[62] A. Ioannidis and J. P. Dodelet, Journal of Physical Chemistry B **1997**, 101, 5100-5107.*

*[63] N. McKeown, Phthalocyanine Materials: synthesis, structure and function., Cambridge University Press, **1998**, p. 193.*

*[64] H. Laurs and G. Heiland, Thin Solid Films **1987**, 149, 129-142.*

*[65] A. Meller and A. Ossko, Monatshefte Fur Chemie **1972**, 103, 150.*

*[66] V. R. Ferro, L. A. Poveda, R. H. González-Jonte, J. M. Garcia de la Vega, T. Torres and B. del Rey, Journal of Porphyrins and Phthalocyanines **2000**, 4, 611-620.*

*[67] M. Trelka, A. Medina, D. Ecija, C. Urban, O. Groening, R. Fasel, J. M. Gallego, C. G. Claessens, R. Otero, T. Torres and R. Miranda, Chemical Communications **2011**, 47, 9986-9988.*

*[68] H. Kumar, P. Kumar, R. Bhardwaj, G. D. Sharma, S. Chand, S. C. Jain and V. Kumar, Journal of Physics D-Applied Physics **2009**, 42, 015103.*

*[69] P. Heremans, D. Cheyns and B. P. Rand, Accounts of Chemical Research **2009**, 42, 1740-1747.*

*[70] H. Gommans, D. Cheyns, T. Aernouts, C. Girotto, J. Poortmans and P. Heremans, Advanced Functional Materials **2007**, 17, 2653-2658.*

*[71] H. W. Kroto, J. R. Heath, S. C. Obrien, R. F. Curl and R. E. Smalley, Nature **1985**, 318, 162-163.*

*[72] J. N. Haddock, X. H. Zhang, B. Domercq and B. Kippelen, Organic Electronics **2005**, 6, 182-187.*

*[73] M. S. Dresselhaus and G. Dresselhaus, Annual Review of Materials Science **1995**, 25, 487-523.*

*[74] J. Jiang, National University of Singapore Engineering Research **2006**, 21, 11.*

*[75] P. Peumans and S. R. Forrest, Applied Physics Letters **2001**, 79, 126-128.*

*[76] I. Hancox, P. Sullivan, K. V. Chauhan, N. Beaumont, L. A. Rochford, R. A. Hatton and T. S. Jones, Organic Electronics **2010**, 11, 2019-2025.*

*[77] H. Gommans, B. Verreet, B. P. Rand, R. Muller, J. Poortmans, P. Heremans and J. Genoe, Advanced Functional Materials **2008**, 18, 3686-3691.*

*[78] T. Yasuda, Y. Yamaguchi, D. C. Zou and T. Tsutsui, Japanese Journal of Applied Physics Part 1-Regular Papers Short Notes & Review Papers **2002**, 41, 5626-5629.*

*[79] D. R. Lide, CRC handbook of chemistry and physics, CRC Press, **1993**, p. 2712.*

*[80] M. Chelvayohan and C. H. B. Mee, Journal of Physics C-Solid State Physics **1982**, 15, 2305-2312; M. Uda, A. Nakamura, T. Yamamoto and Y. Fujimoto, Journal of Electron Spectroscopy and Related Phenomena **1998**, 88, 643-648.*

*[81] S. Schwertheim, M. Leinhos, T. Mueller, H. C. Neitzert, W. R. Fahmer and Ieee in PEDOT with carbon nanotubes as a replacement for the transparent conductive coating (ITO) of a heterojunction solar cell, Vol. **2008**, pp. 1259-1263; D. S. Ghosh, R. Betancur, T. L. Chen, V. Pruneri and J. Martorell, Solar Energy Materials and Solar Cells **2011**, 95, 1228-1231; K. Y. Lee, Y. K. Kim, O. K. Kwon, J. W. Lee, D. M. Shin, D. Y. Kim, B. C. Sohn and D. S. Choi, Thin*

*Solid Films **2000**, 363, 225-228; J. Q. Zhao, S. J. Xie, S. H. Han, Z. W. Yang, L. N. Ye and T. L. Yang, Synthetic Metals **2000**, 114, 251-254.*
*[82] R. F. Salzman, J. G. Xue, B. P. Rand, A. Alexander, M. E. Thompson and S. R. Forrest, Organic Electronics **2005**, 6, 242-246.*
*[83] G. Sauerbrey, Zeitschrift für Physik A Hadrons and Nuclei **1959**, 155, 206-222.*
*[84] Q. Zhong, D. Inniss, K. Kjoller and V. B. Elings, Surface Science **1993**, 290, L688-L692.*
*[85] T. S. Druzhinina, S. Hoeppener and U. S. Schubert, Nano Letters **2010**, 10, 4009-4012.*
*[86] Y. Martin, C. C. Williams and H. K. Wickramasinghe, Journal of Applied Physics **1987**, 61, 4723-4729; G. Binnig, C. F. Quate and C. Gerber, Physical Review Letters **1986**, 56, 930-933.*
*[87] N. Corporation in Solar Simulator Spectral Irradiance Data, Vol. 2011 http://www.newport.com, **2011**.*
*[88] Spectrolab in Spectroscopic ellipsometer SE GES5E, Vol. 2011 http://www.sopra-sa.com, **2009**; Accurion in Nanofilm EP3_SE, Vol. 2011 **2011**.*
*[89] A. Yakimov and S. R. Forrest, Applied Physics Letters **2002**, 80, 1667-1669.*
*[90] S. E. Shaheen, C. J. Brabec, N. S. Sariciftci, F. Padinger, T. Fromherz and J. C. Hummelen, Applied Physics Letters **2001**, 78, 841-843; F. Padinger, R. S. Rittberger and N. S. Sariciftci, Advanced Functional Materials **2003**, 13, 85-88; F. Pichot and B. A. Gregg, Journal of Physical Chemistry B **2000**, 104, 6-10; Mandelko.J and J. H. Lamneck, Journal of Applied Physics **1973**, 44, 4785-4787.*
*[91] V. Chauhan, R. Hatton, P. Sullivan, T. Jones, S. W. Cho, L. Piper, A. deMasi and K. Smith, Journal of Materials Chemistry **2010**, 20, 1173-1178.*
*[92] K. L. Mutolo, E. I. Mayo, B. P. Rand, S. R. Forrest and M. E. Thompson, Journal of the American Chemical Society **2006**, 128, 8108-8109.*
*[93] A. Madan, Materials and Manufacturing Processes **2007**, 22, 412-418.*
*[94] V. Chauhan in Understanding the Open-Circuit Voltage in Small Molecule Heterojunction Photovoltaic Devices, Vol. Doctor of Philosophy in Chemical Physics University of Warwick, Warwick Library, **2010**, p. 156.*
*[95] A. Beer, Einleitung in die höhere Optik, Druck und Verlag von Friedrich Vieweg und Sohn, **1853**, p. 430.*
*[96] D. F. Swinehart, Journal of Chemical Education **1962**, 39, 333.*
*[97] M. Born, E. Wolf, A. B. Bhatia, P. C. Clemmow, D. Gabor, A. R. Stokes, A. M. Taylor, P. A. Wayman and W. L. Wilcock, Principles of Optics: Electromagnetic Theory of Propagation, Interference and Diffraction of Light, Cambridge University Press, **2000**, p. 986.*
*[98] C. L. Mitsas and D. I. Siapkas, Applied Optics **1995**, 34, 1678-1683; O. S. Heavens, Reports on Progress in Physics **1960**, 23, 1.*
*[99] H. G. Tompkins and E. A. Irene, Handbook of ellipsometry, William Andrew Pub. ; Heidelberg, Germany : Springer, Norwich, N.Y., **2005**, p. xvi, 870.*
*[100] L. Brits in Eulerangles, Vol. Wikipedia, **2008**, pp. Euler angles, hand drawn Inkscape.*
*[101] P. Yeh, Journal of the Optical Society of America **1979**, 69, 742-756.*
*[102] S. S. Sun and N. S. Sariciftci, Organic photovoltaics: mechanism, materials, and devices, Taylor & Francis, **2005**, p. 664.*
*[103] F. M. Braun in Modelling of Light-Trapping Structures and their Application in Organic Photovoltaic Devices, Vol. Doctor of Philosophy Imperial College London, London, **2007**, p. 265.*
*[104] M. A. Dupertuis, B. Acklin and M. Proctor, Journal of the Optical Society of America a-Optics Image Science and Vision **1994**, 11, 1167-1174.*
*[105] T. C. Choy, Effective Medium Theory: Principles and Applications, Oxford University Press, USA, **1999**, p. 200.*
*[106] Y. Wang, D. H. Gu and F. X. Gan, Optics Communications **2000**, 183, 445-450.*
*[107] D. Datta and S. Kumar, Journal of Applied Physics **2009**, 106, 074517.*

[108] Z. T. Liu, C. Y. Kwong, C. H. Cheung, A. B. Djurisic, Y. Chan and P. C. Chui, Synthetic Metals ***2005****, 150, 159-163.*
[109] A. Szekeres, T. Ivanova and K. Gesheva, Journal of Solid State Electrochemistry ***2002****, 7, 17-20.*
[110] W. A. Luhman and R. J. Holmes, Advanced Functional Materials ***2011****, 21, 764-771.*
[111] J. Gilot, M. M. Wienk and R. A. J. Janssen, Advanced Functional Materials ***2010****, 20, 3904-3911.*
[112] A. Hadipour, B. de Boer and P. W. M. Blom, Organic Electronics ***2008****, 9, 617-624.*
[113] J. Gilot, M. M. Wienk and R. A. J. Janssen, Organic Electronics ***2011****, 12, 660-665.*
[114] E. F. Zalewski and J. Geist, Applied Optics ***1980****, 19, 1214-1216.*
[115] J. Burdick and T. Glatfelter, Solar Cells ***1986****, 18, 301-314.*
[116] S. Rohr in Heliatek achieves new world record for organic solar cells with certified 9.8% cell efficiency, Vol. http://www.heliatek.com/?p=1346&lang=en, ***2011****.*
[117] J. Wagner, T. Fritz and H. Bottcher, Physica Status Solidi a-Applied Research ***1993****, 136, 423-432; L. A. A. Pettersson, L. S. Roman and O. Inganas, Journal of Applied Physics* ***1999****, 86, 487-496.*